

UNIVERSITY OF EAST ANGLIA

DOCTORAL THESIS

**The Southern Boundary of the
Antarctic Circumpolar Current**

by

Ria Oelerich

A thesis submitted in partial fulfillment of the requirements
for the degree of Doctor of Philosophy
in the

Centre for Ocean and Atmospheric Sciences
School of Environmental Sciences

September 2022

Supervisors:

Karen J. Heywood

Gillian M. Damerell

© This copy of the thesis has been supplied on condition that anyone who consults it is understood to recognise that its copyright rests with the author and that use of any information derived there from must be in accordance with current UK Copyright Law. In addition, any quotation or extract must include full attribution.

© Copyright 2022

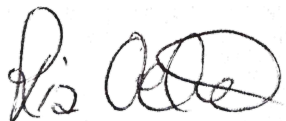
Ria Oelerich

Declaration of Authorship

I, Ria Oelerich, declare that this thesis titled, “The Southern Boundary of the Antarctic Circumpolar Current” and the work presented in it are my own. I confirm that:

- This work was done wholly or mainly while in candidature for a research degree at this University.
- Where any part of this thesis has previously been submitted for a degree or any other qualification at this University or any other institution, this has been clearly stated.
- Where I have consulted the published work of others, this is always clearly attributed.
- Where I have quoted from the work of others, the source is always given. With the exception of such quotations, this thesis is entirely my own work.
- I have acknowledged all main sources of help.
- Where the thesis is based on work done by myself jointly with others, I have made clear exactly what was done by others and what I have contributed myself.

Signed:



Date:

21.09.2022

UNIVERSITY OF EAST ANGLIA

Abstract

Centre for Ocean and Atmospheric Sciences

School of Environmental Sciences

Doctor of Philosophy

The Southern Boundary of the Antarctic Circumpolar Current

by Ria Oelerich

Antarctic ice sheet mass loss is a major contributor to global sea level rise. Circumpolar Deep Water, transported by the Antarctic Circumpolar Current (ACC), contributes heat to amplify ice shelf basal melting, when it accesses the Antarctic continental shelf. The Southern Boundary of the ACC provides the closest connection of warm ACC waters to Antarctica. Strong density gradients across the Southern Boundary constitute a frontal jet and modulate the southward heat transport. Mechanisms modulating the poleward transport of heat are poorly understood. This thesis explores two such mechanisms.

Firstly, the frontal structure of the Southern Boundary is investigated with observed hydrographic transects. A global ocean reanalysis is used to identify the interannual and seasonal variability of the Southern Boundary and deep-water temperatures on the Bellingshausen Sea continental shelf. Annual means of potential temperature reveal interannual variability and enable separation into warm and cold regimes with deep-water temperature differences of up to 1°C. The results suggest that the deep-water temperature in the southern Bellingshausen Sea is due to a combination of shelf break heat transport and surface heat fluxes. Surface heat flux variability is related to the variability of the Amundsen Sea Low and its influence on sea ice extent and local formation of cold, dense water in winter.

Secondly, the variability of the Southern Boundary at the Greenwich Meridian is investigated using ocean gliders and satellite altimetry. It is demonstrated that a cyclonic eddy near the Southern Boundary increases its density gradients and amplifies its frontal jet. Mixing length scales are suppressed across the frontal jet while the eddy is crossing and increase to about 25 km after the eddy has crossed the Greenwich Meridian. This increase supports an increased exchange of water parcels across the Southern Boundary, implying that the ‘barrier’ properties of the Southern Boundary are reduced.

Access Condition and Agreement

Each deposit in UEA Digital Repository is protected by copyright and other intellectual property rights, and duplication or sale of all or part of any of the Data Collections is not permitted, except that material may be duplicated by you for your research use or for educational purposes in electronic or print form. You must obtain permission from the copyright holder, usually the author, for any other use. Exceptions only apply where a deposit may be explicitly provided under a stated licence, such as a Creative Commons licence or Open Government licence.

Electronic or print copies may not be offered, whether for sale or otherwise to anyone, unless explicitly stated under a Creative Commons or Open Government license. Unauthorised reproduction, editing or reformatting for resale purposes is explicitly prohibited (except where approved by the copyright holder themselves) and UEA reserves the right to take immediate 'take down' action on behalf of the copyright and/or rights holder if this Access condition of the UEA Digital Repository is breached. Any material in this database has been supplied on the understanding that it is copyright material and that no quotation from the material may be published without proper acknowledgement.

Acknowledgements

These four years of PhD passed by in just a blink of an eye. In one moment I finished my Master's and in the next I am about to submit my PhD thesis. It was an unforgettable journey. I learned so many important lessons that helped me to grow as a person and as a scientist. Therefore, it gives me great pleasure to thank and appreciate all of those special people who supported me during this journey.

First and foremost, I would like to thank Karen for her guidance, endless patience, constructive criticism and kindness. I am lucky to have you as a mentor and working with you over the past couple of years has been an absolute pleasure. Thank you for having me at UEA. I want to thank Gillian for her great support, scientific advice and for sharing her glider knowledge. Thanks to both of you for always having an ear for me and for being phenomenal supervisors throughout my PhD.

I am grateful to all the great scientists I have met and collaborated with during my PhD. Thanks to Andy for taking me on my first research expedition to the Southern Ocean, for his great scientific input and patience throughout endless draft-readings. Thanks to Seb, Marcel and Louise for their collaboration and for welcoming me to Gothenburg. I am hoping to visit again in the future.

I want to thank to all my 3.16 office mates and ENVEast cohort members, who have become good friends. Thanks for all the useful input, discussions and ideas. Callum, Beth, Leigh and Midge thanks for your friendship, great game nights, delicious pizza, cycle rides and squash that kept me going. Yanxin, Yixi and Shenje, thanks for yummy hot pot nights. It has been a pleasure to get to know all of you.

I would also like to thank my good friend Johnny, who persuaded me to take more breaks and entertained me with uncountable rounds of Mario Kart during many months of unwanted home office.

Most importantly, I want to thank my parents for their unconditional love and support. You always have my back and I would not be who I am without you.

Finally, I thank the European Research Council (ERC) for the financial support throughout this PhD.

Contents

Declaration of Authorship	v
Abstract	vii
Acknowledgements	ix
1 Introduction	1
1.1 Motivation	1
1.2 The Southern Ocean	3
1.3 Research Questions and Thesis Structure	9
2 Variability of the Antarctic Circumpolar Current’s Southern Boundary in the Bellingshausen Sea	11
2.1 Introduction	11
2.2 Data and Methodology	13
2.3 Hydrography and Frontal Structure of the Bellingshausen Sea across the Shelf Break and Slope	15
2.4 Location of the Southern Boundary in the Bellingshausen Sea .	18
2.5 Variability of the Southern Boundary	22
2.5.1 Seasonal Variability	22
2.5.2 Interannual Variability and Relation to Warm Water Pen- etration onto the Shelf	24
2.6 Summary and Conclusions	27
3 Wind-induced Variability of Warm Water on the Bellingshausen Sea Continental Shelf	31
3.1 Introduction	31
3.2 The GLORYS12V1 Reanalysis and Climatology	36
3.3 Modes of Variability of Ocean Temperature on the Continental Shelf	43
3.4 Mechanisms Leading to Warm and Cold Regimes on the Conti- nental Shelf	52
3.5 Conclusions	63

4	Stirring across the Antarctic Circumpolar Current's Southern Boundary at the Greenwich Meridian, Weddell Sea	67
4.1	Introduction	67
4.2	Frontal Structure of the Southern Boundary	70
4.3	Effects of Mesoscale Eddies on Frontal Structure and Frontal Jet	73
4.4	Effects of Mesoscale Eddies on Mixing Length Scales	77
4.4.1	Interannual Variability of Barrier Properties	84
4.5	Conclusions	89
5	Conclusions and Future Work	91
5.1	Summary	91
5.1.1	The Bellingshausen Sea	92
5.1.2	The Weddell Sea	94
5.2	Future Work	97
5.3	Final Considerations	100
	References	107

List of Figures

1.1	Antarctica's thickness and elevation of grounded ice and ice shelf trends	2
1.2	Schematic of the meridional overturning circulation in the Southern Ocean	5
1.3	Fronts of the Antarctic Circumpolar Current	6
1.4	Idealised schematics of ACC fronts	7
2.1	Map of observed cross-slope transects	14
2.2	Hydrography of cross-slope transects	17
2.3	Long-term mean conditions of the Southern Boundary	19
2.4	Stages of the Southern Boundary	20
2.5	Seasonal variability of the Southern Boundary	23
2.6	Hovmöller diagram transect 1	26
2.7	Hovmöller diagram Transect 4	27
3.1	Map of the Southern Ocean and the Bellingshausen Sea	35
3.2	Long-term mean conditions	39
3.3	Vertical profiles of potential temperature	40
3.4	Long-term mean conditions, ERA5	42
3.5	Spatial and temporal temperature variability	44
3.6	Anomalies and composites	47
3.7	Vertical profiles of potential temperature and practical salinity at 83°W, 72.5°S	48
3.8	Composites of potential temperature and practical salinity from a meridional transect located at 83°W, warm and cold regimes	50
3.9	Composites of potential temperature and practical salinity from a zonal transect located at 72°S, warm and cold regimes	51
3.10	Basic ocean heat budget	55
3.11	Composites of sea level pressure and sea surface heights and anomalies of current speeds, warm and cold regimes	56
3.12	Anomalies of wind speeds, zonal and meridional wind components, warm and cold regimes	58

3.13	Anomalies of sea ice concentration, warm and cold regimes; correlation maps	60
3.14	Timeseries of sea ice concentration, potential temperature and practical salinity	61
3.15	Schematics of processes and conditions for warm and cold regimes	65
4.1	Map of the study region at the Greenwich Meridian	70
4.2	Hydrography of glider transects	74
4.3	Mean glider transect and standard deviation	75
4.4	Glider transects A and C; current speeds	78
4.5	Regimes across the Southern Boundary	79
4.6	Θ/S Diagram glider transect A	80
4.7	Θ/S Diagram glider transect C	81
4.8	Geostrophic velocities of transects A and C	82
4.9	Mixing length scale diagnostics, transect A	85
4.10	Mixing length scale diagnostics, transect C	86
4.11	Hovmöller diagrams of frontal structure	88
5.1	Future Observations	99
A1	Long-term mean wind speed (Summer, Winter)	103
A2	Summer wind field anomalies	104
A3	Winter wind field anomalies	105
A4	Sea ice concentration anomaly	106

List of Abbreviations

AASW	Antarctic Surface Water
ACC	Antarctic Circumpolar Current
ADT	Absolute Dynamic Topography
LADCP	Lowered Acoustic Doppler Current Profiler
ASC	Antarctic Slope Current
ASL	Amundsen Sea Low
CATS2008	Circum-Antarctic Tidal Simulation 2008
CDW	Circumpolar Deep Water
CSW	Continental Shelf Water
GLORYS	GLORYS12V1 reanalysis
DAC	Dive Average Current
ENSO	El-Niño-Southern-Oscillation
EOF	Empirical Orthogonal Function
mCDW	modified Circumpolar Deep Water
MLS	Mixing Length Scale
MEI	Multivariate ENSO Index
PF	Polar Front
UCDW	Upper Circumpolar Deep Water
SACCF	Southern ACC Front
SADCP	Shipboard Acoustic Doppler Current Profiler
SAF	Subantarctic Front
SAM	Southern Annular Mode
SLA	Sea Level Anomaly
SOI	Southern Oscillation Index
SSH	Sea Surface Height
SST	Sea Surface Temperature
WAP	West Antarctic Peninsula

Chapter 1

Introduction

1.1 Motivation

Global sea level rise is a critical societal challenge. Over the twentieth century, the global-mean sea level has increased by approximately 1.5 mm y^{-1} (e.g. Oppenheimer et al., 2019; Dangendorf et al., 2019; Hay et al., 2017). The change in global-mean sea level is a net result of many individual geophysical and climatological processes, where the largest contributions to the global-mean sea level are attributed to ice mass loss and thermal expansion of the ocean (e.g. Frederikse et al., 2020; Church et al., 2013).

As the largest reservoir of terrestrial ice, the Antarctic ice sheet represents a significant contributor to sea level rise in a warming climate (Shepherd et al., 2012b) and has the potential to raise the global sea level by 58 m, if rapidly discharged (Fretwell et al., 2013). Over recent decades, the thickness (Shepherd et al., 2012a) and extent (Cook and Vaughan, 2010) of floating ice shelves has reduced, which has resulted in disrupted inland ice flow and triggered retreat (Konrad et al., 2018; Rignot et al., 2014), acceleration (Joughin et al., 2002; Rignot et al., 2004) and drawdown (Shepherd et al., 2002; Scambos et al., 2004) of many marine-terminating ice streams of Antarctica. These changes do not occur uniformly around the continent (Fig. 1.1). Instead, the highest rates of ice shelf thinning and retreat were reported in the West Antarctic sector (Shepherd et al., 2018), where the Amundsen and Bellingshausen seas and the West Antarctic Peninsula (WAP) are susceptible to the penetration of warm waters onto the continental shelf and underneath ice shelf cavities and resulting ocean-driven basal melt (Thoma et al., 2008; Pritchard et al., 2012). The retreat of grounding lines through basal melt is further associated with the destabilisation of grounded ice as ice shelves serve as an important mechanical support for the grounded ice upstream (Shepherd et al., 2018).

The amount of heat accessing the continental shelf and entering ice shelf cavities is dependent on many different factors that are unique within each of

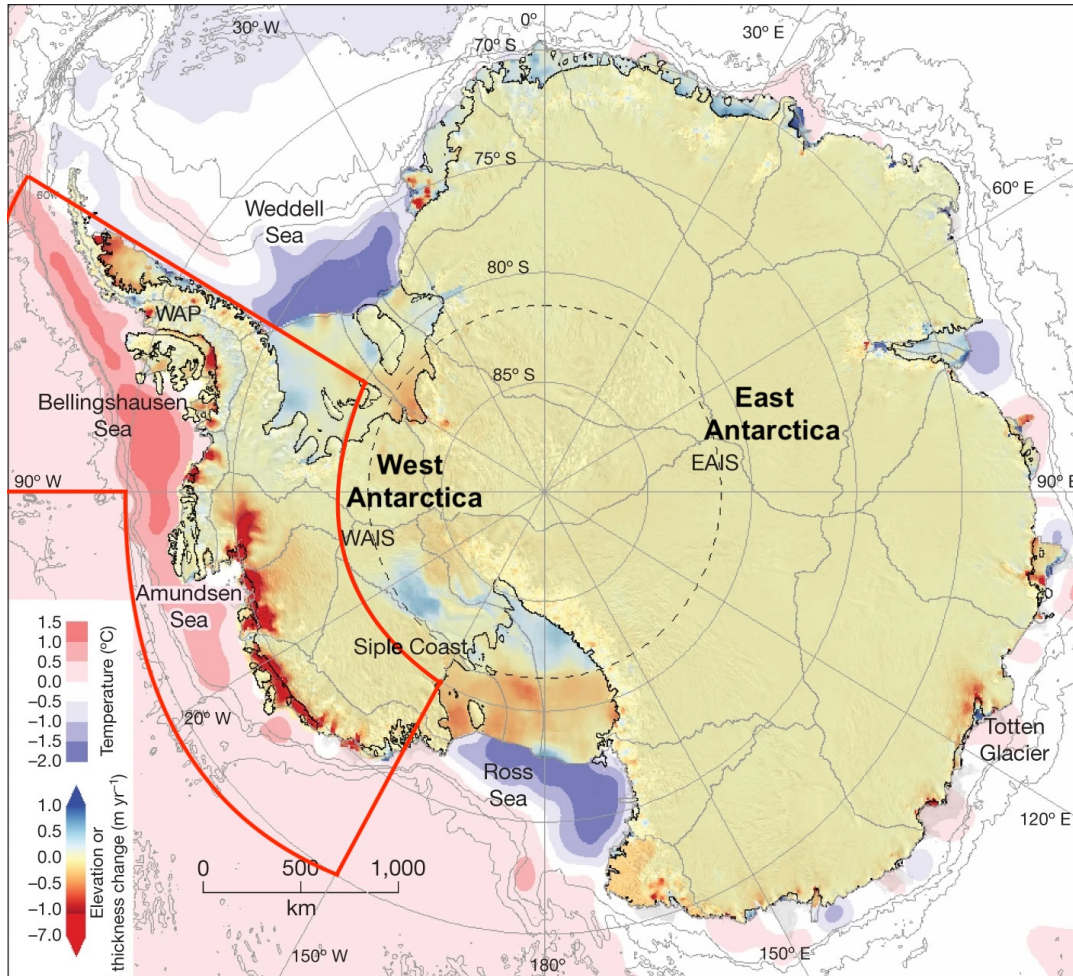


Figure 1.1: Average trend in thickness and elevation of Antarctica’s grounded ice and ice shelves determined between 1992 and 2017 north of 81.5°S (dashed grey circle) and from 2010 to 2017 elsewhere. Also shown is the depth (light grey contours) and estimated ocean temperature at the seafloor around Antarctica. The West Antarctic Sector is highlighted with the red box. Key geographic features are labelled. WAIS, EAIS and WAP are acronyms for West and East Antarctic ice shelves and the West Antarctic Peninsula. Figure modified from Shepherd et al. (2018).

the marginal seas around Antarctica. The atmospheric and oceanic circulation, cross-frontal exchange, interaction with bathymetric features, sea ice formation and melting and water mass transformation are important processes influencing the heat content on the continental shelf. However, with progressing global warming, the future Antarctic ice mass loss and its contribution to global sea level rise are likely to increase (e.g. Church et al., 2013). Therefore, understanding and quantifying the relative importance of these processes is essential to improve future climate predictions and their consequences.

1.2 The Southern Ocean

The Southern Ocean is described as the broad ocean region surrounding Antarctica. It is not separated from the Atlantic, Pacific and Indian oceans by continental land masses and is thus not defined as a formal geographic region (Talley et al., 2011). In general, the Southern Ocean is confined to the region south of 60°S , but its oceanic regime extends further north. The absence of land barriers in the latitude band (between the WAP and South America) largely influences the dynamics and current systems in the Southern Ocean. The result is a strong current system, the Antarctic Circumpolar Current (ACC) that dominates the large scale circulation in the Southern Ocean. The ACC flows continuously eastward and encircles Antarctica with its northernmost boundaries extending up to 35°S . The ACC is the main oceanographic feature that connects all ocean basins and is thus a key component of the global meridional overturning circulation (Fig. 1.2). The interbasin connection provided by the ACC is also a key component in interbasin exchange and allows the possibility of oceanic teleconnections (e.g. Wang et al., 2018; Peterson and White, 1998; White and Peterson, 1996).

The wind forcing of the Southern Ocean is dominated by eastward winds (Westerlies) in the latitude band $40\text{-}60^{\circ}\text{S}$. The induced surface wind stress generates a northward Ekman transport that converges north of the surface wind stress maximum (downwelling of surface waters into the ocean interior) and diverges south of the wind stress maximum (upwelling of deep waters into the surface layer). The induced surface wind stress forms the upper cell of the meridional overturning circulation (Fig. 1.2) and is the main driver of the ACC.

The ACC is characterised by a number of oceanic fronts that mark sharp transitions in water mass properties. The ACC fronts are termed from north to south as the Subantarctic Front (SAF), Polar Front (PF) and the Southern ACC Front (SACCF) (Fig. 1.3). The frontal regions are denoted by strongly sloping isopycnals shallowing to the south associated with strong deep-reaching eastward-flowing jets (Orsi et al., 1995) (Fig. 1.4). Within the ACC fronts the exchange between the surface and deep oceans is pronounced, as both upwelling of deep waters and subduction of surface waters are enhanced (Morrison et al., 2015; Stukel et al., 2017). The ACC transports the Southern Ocean's major source of heat, Circumpolar Deep Water (CDW), around Antarctica. The eastward transport of CDW is dominated by the frontal jets that extend to the ocean bottom. The jet speeds vary within each front and from front to front

of the ACC. The SAF is on average the most energetic of the Southern Ocean frontal jets (30 to 70 cm s⁻¹) (Hofmann, 1985). The eastward transport of the ACC is traditionally calculated through Drake Passage. The ACC is limited here by South America to the north and the WAP to the south. The two most recent observational programs, DRAKE and cDrake, provided estimates of the total volume transport that varies between 141±2.7 Sv and 173.3±10.7 Sv through Drake Passage (Koenig et al., 2014; Chidichimo et al., 2014). The southernmost edge of the ACC is known as the Southern Boundary (Fig. 1.4, yellow contour). Its definition is not based on the characteristics of a dynamical front (Talley et al., 2011), but rather as a boundary of water mass properties that separates warm ACC waters from colder waters further south (Orsi et al., 1995). Traditionally, the Southern Boundary is defined as the southernmost limit of Upper Circumpolar Deep Water (UCDW, $\theta > 1.5^\circ\text{C}$ and $S > 34.5$, (Orsi et al., 1995)). The distance of the Southern Boundary to coastal regions varies around Antarctica, where its northernmost displacement is located in areas of cyclonic gyres with clockwise surface circulation in the Weddell and Ross seas (Fig. 1.3).

In the regions south of the Southern Boundary, westward winds (Easterlies) prevail that induce a poleward Ekman transport of Antarctic Surface Water (AASW; formed by cooling and freshening of upwelled CDW in winter and ice melt in summer) onto the continental shelf. The poleward Ekman transport on the continental shelf generates coastal downwelling. Strong horizontal gradients occur between colder shelf waters and warm CDW (e.g. Baines and Condie, 1998; Whitworth et al., 1985; Jacobs, 1991). This gradient is also defined as the Antarctic Slope Front (ASF) (Thompson et al., 2018). Associated with the ASF, the Antarctic Slope Current (ASC) dominates the zonal circulation near the continental slope and shelf break flowing westward and is a nearly circumpolar current. The Antarctic Coastal Current (AACC) is located in close proximity to the coastline. Together, the ASC and AACC constitute the major westward currents within the Antarctic margins (Jacobs, 1991; Heywood et al., 2004). Regions such as the Bellingshausen Sea and the WAP experience weakest westward winds along the slope due to a low pressure system located above the Amundsen and Bellingshausen seas, the Amundsen Sea Low (ASL). The ASC is absent along the shelf break regions in most of the Bellingshausen Sea and WAP, whereas the AACC has been identified as a continuous current reaching from the WAP through the Bellingshausen Sea into the Amundsen Sea (Assmann et al., 2005; Holland et al., 2010; Schubert et al., 2021). Due to the absence of the ASC in most parts of the Bellingshausen Sea, the flow along the shelf break is

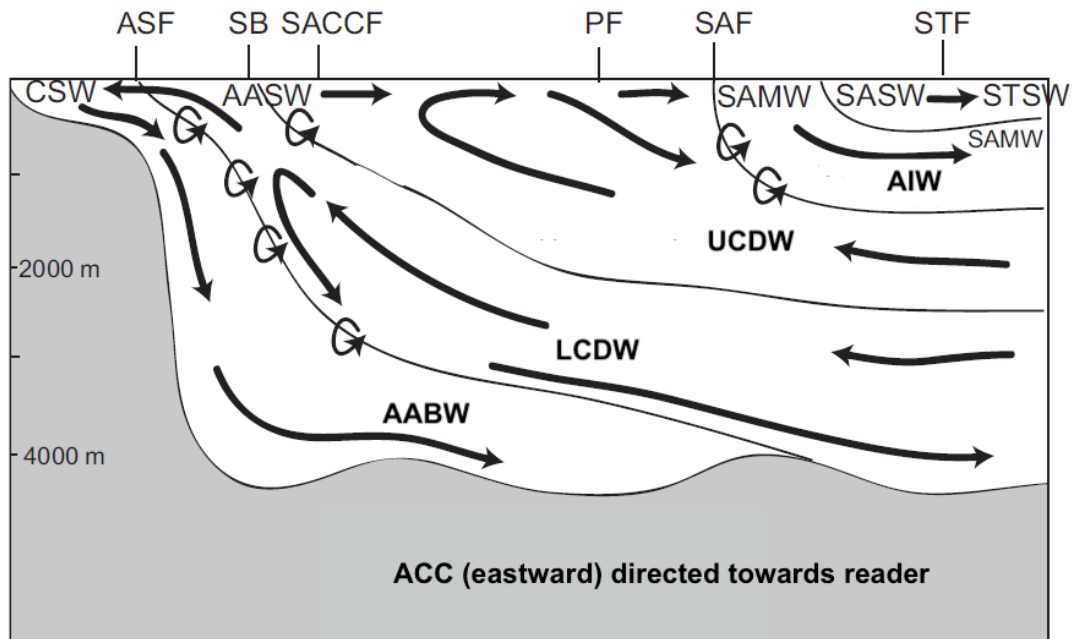


Figure 1.2: A schematic of a meridional section across the Southern Ocean showing the key water masses, the meridional overturning circulation and the fronts and boundaries of the ACC and frontal circulation features close to the Antarctic continent. The acronyms are: Antarctic Circumpolar Current (ACC), Continental Shelf Water (CSW), Antarctic Surface Water (AASW), Subantarctic Mode Water (SAMW), Subantarctic Surface Water (SASW), Subtropical Surface Water (STSW), Antarctic Intermediate Water (AIW), Upper Circumpolar Deep Water (UCDW), Lower Circumpolar Deep Water (LCDW), Antarctic Bottom Water (AABW), Antarctic Slope Front (ASF), Southern Boundary (SB), Southern ACC Front (SACCF), Polar Front (PF), Subantarctic Front (SAF), Subtropical Front (STF). Figure modified from Talley et al. (2011) and Speer et al. (2000).

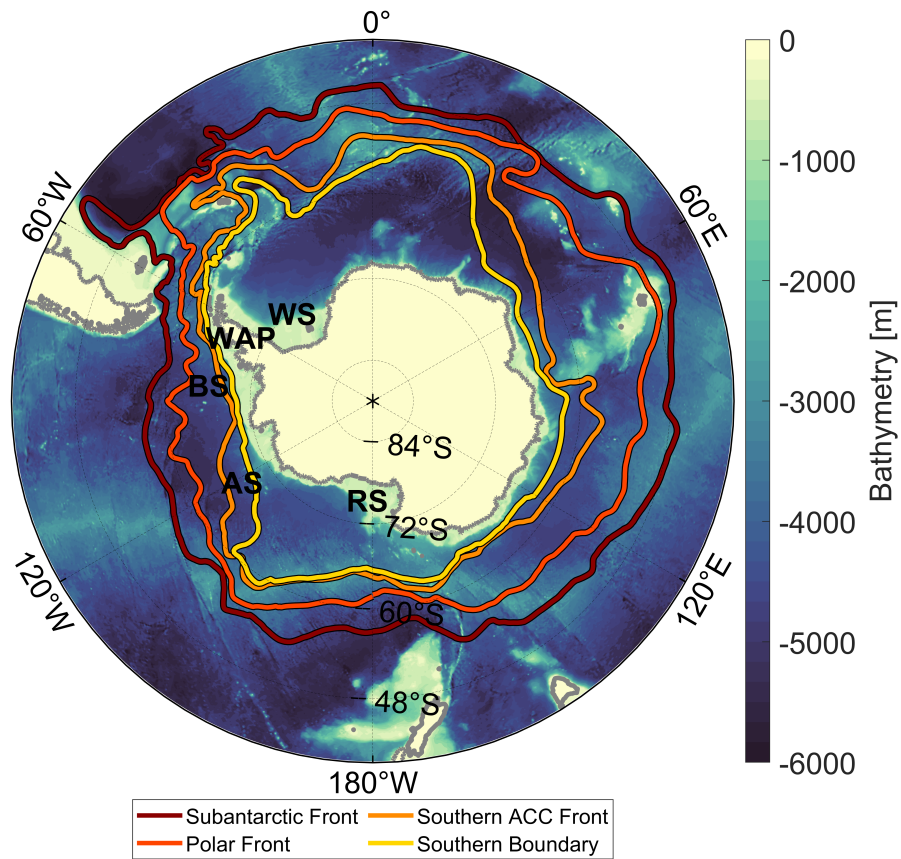


Figure 1.3: Map of the bathymetry around Antarctica from Schaffer et al. (2019) superimposed with contours of the Antarctic Circumpolar Current fronts from Orsi et al. (1995) sorted from red to yellow: Subantarctic Front (SAF), Polar Front (PF), Southern Antarctic Circumpolar Current Front (SACCF) and the Southern Boundary (SB). The black contour indicates the coastline. Key geographic features are labelled: Ross Sea (RS), Amundsen Sea (AS), Bellingshausen Sea (BS), West Antarctic Peninsula (WAP) and Weddell Sea (WS).

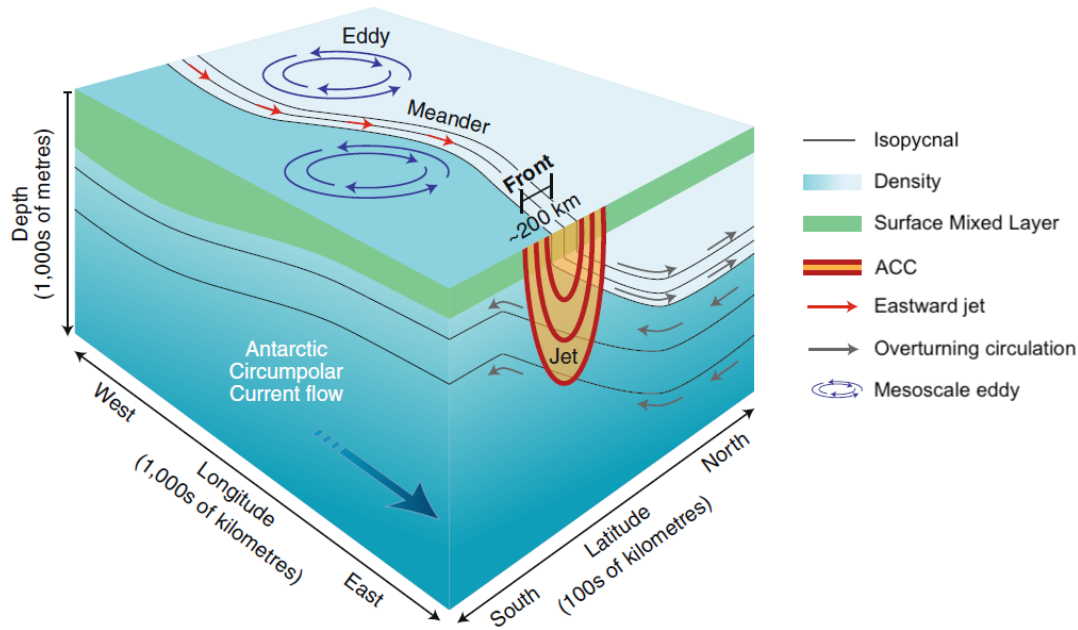


Figure 1.4: Schematic showing the physical characteristics of the idealised ACC fronts. The frontal region is characterised by strongly sloping isopycnals shallowing to the south (black line) and strong geostrophic jets (red arrows) that separate regions of high and low density. The upwelling and subduction processes associated with the overturning circulation are highlighted with grey arrows and mesoscale eddies interacting with the frontal regions are marked with blue arrows. Figure modified from Chapman et al. (2020).

therefore dominated by the frontal jet associated with the Southern Boundary of the ACC (Thompson et al., 2020), which is located in close proximity to the continental shelf in the West Antarctic sector. The ASC in the Amundsen Sea can act as barrier to cross-slope transport and regulate the amount of heat accessing the continental shelf (e.g. Thompson and Heywood, 2008). In the Bellingshausen Sea, the Southern Boundary is a crucial circulation feature that represents the southernmost barrier to mixing and regulates Antarctica’s thermal conditions (Naveira-Garabato et al., 2011; Yamazaki et al., 2021). In comparison to shelf break processes in the Amundsen Sea and the WAP, shelf break processes in the Bellingshausen Sea related to the Southern Boundary and its spatial and temporal variability are poorly observed. These processes are the subject of Chapter 2.

The local formation Antarctic Bottom Water (AABW, formed when cold, dense shelf water spills down the continental slope and mixes with CDW) drive the lower cell of the meridional overturning circulation near the Antarctic continent (Talley et al., 2011) (Fig. 1.2). The formation of dense shelf water is not uniform around the Antarctic continental shelf as it is influenced by water

mass properties and physical processes such as air-sea exchange, sea ice formation, opening and extent of coastal or open ocean polynya regions (areas of open water surrounded by ice-covered regions), ice shelf melt, and intrusions of CDW, or its colder modified variants (mCDW), onto the continental shelf. Dense shelf water properties can thus vary in temperature, salinity and seasonally produced volume, which also influences the properties of AABW locally. Major dense shelf water producing regions have been identified in the southern Weddell Sea, Cape Darnley, Prydz Bay, Adélie Coast and in the western Ross Sea, where dense shelf water is produced predominantly in winter (Narayanan et al., 2019). In contrast, regions such as the Amundsen and Bellingshausen seas experience more intense CDW intrusions and are thus kept in a warmer regime than the peak dense shelf water production regions year-round (Narayanan et al., 2019). Specifically for the Bellingshausen Sea, the temporal and spatial variability of local cold water formation as well as warm and cold regimes remain surprisingly understudied and are thus examined in Chapter 3.

Another important component that characterises the unstable structure of the ACC is the highly energetic eddy field. Eddy fluxes within the ACC generate torques that can shift jets or cause them to meander (Fig. 1.4) and can accelerate or decelerate the mean flow (e.g. Hughes and Ash, 2001; Williams et al., 2007). Regions of high eddy kinetic energy are generally associated with strong topographic features or subtropical extensions of western boundary currents (e.g. Malvinas–Brazil Current Confluence or Agulhas Retroflexion). Eddies are also responsible for the stirring of tracers away from the main ACC jets (Ferrari and Nikurashin, 2010) and play a crucial role in transporting heat poleward as no net meridional geostrophic flow can exist across unbounded latitudes (Rintoul et al., 2001). The strong frontal jets are thus not only important for the eastward transport of water masses around Antarctica, but also act as barriers to horizontal mixing (Naveira-Garabato et al., 2011; Thompson and Sallée, 2012; Chapman and Sallée, 2017). The Southern Boundary, which also represents the southernmost barrier to mixing, remains fairly understudied with respect to changing barrier properties in response to climate change. This is discussed in Chapter 4.

1.3 Research Questions and Thesis Structure

This thesis is based on three main research questions that aim to improve our understanding of the dynamics of the Southern Ocean. The research questions are investigated and discussed within the result chapters (Chapters 2-4). The research questions are:

1. Is the extent of warm waters on the continental shelf impacted by the spatial and temporal variability of the Southern Boundary?
2. Which processes are the main drivers of temperature variability on the Bellingshausen Sea continental shelf?
3. Which processes impact the mixing of water mass properties across the Southern Boundary?

In Chapter 2, hydrographic transects from CTD stations and a global ocean reanalysis product (GLORYS12V1, DOI: 10.48670/moi-00021, hereinafter referred to as GLORYS) are used to investigate the frontal structure of the Southern Boundary along the shelf break and slope of the Bellingshausen Sea. The observed data include a total of five CTD transects from the years 2007 and 2019 that are reproduced from GLORYS for comparison. GLORYS is further used to investigate the long-term spatial and temporal variability of the Southern Boundary in the Bellingshausen Sea. This chapter specifically investigates the penetration of warm waters onto the continental shelf in relation to the varying distance of the Southern Boundary to the shelf break.

Chapter 3 (submitted to JGR:Oceans, status: published, Oelerich et al., 2022) investigates the temperature variability on the Bellingshausen Sea continental shelf to identify processes that favour the warming or cooling of temperatures on the continental shelf. For this analysis the time period from 1993 to 2018 is considered, where a separation into warm and cold regimes and composite calculations aim to identify relevant processes for the Bellingshausen Sea temperature variability.

In Chapter 4 submitted to Ocean Science, status: in review, repeated and highly-resolved glider transects at the Greenwich Meridian in the Weddell Sea are used to investigate the variability of the Southern Boundary's frontal structure within short time scales. A specific focus is attributed to processes and mechanisms that impact the Southern Boundary's frontal structure, its frontal jet and mixing of properties across it. In order to identify how eddies interact with the Southern Boundary, AVISO satellite altimetry (DOI: 10.48670/moi-00148) is used to determine their location and rotational direction. Finally,

mixing length scale diagnostics are applied to establish the barrier properties of the Southern Boundary while and after an eddy has interacted with the Southern Boundary.

The results of Chapters 2-4 are summarised in Chapter 5 (Conclusions and Future Work) and their contributions to the broader community are synthesised. Additional research questions that arose from our studies within this thesis are considered and suggestions for future studies and observations are emphasised.

Chapter 2

Variability of the Antarctic Circumpolar Current's Southern Boundary in the Bellingshausen Sea

2.1 Introduction

The warming of the Southern Ocean over the past decades has been investigated in various studies (Gille, 2002; Gille, 2008; Swart et al., 2018). This warming is accompanied by an increasing heat content of the West Antarctic continental shelf (Schmidtke et al., 2014) and amplifying glacial melt rates (Pritchard et al., 2012). In response to basal melting and retreat of grounding lines, the thinning of ice shelves provides a significant contribution to the global sea level rise (Paolo et al., 2015). Additionally, the thinning of floating ice shelves in particularly the West Antarctic sector (Amundsen Sea, Bellingshausen Sea, West Antarctic Peninsula (WAP)) present most dramatic changes in correspondence to a changing climate (Cook and Vaughan, 2010; Paolo et al., 2015). However, the analysis of processes that are responsible for the thinning of ice shelves remains difficult in nearly unobserved regions such as the Bellingshausen Sea. This is due to limited observations and the dependency on various factors such as polar gyres, the complex boundary current system over the continental shelf (Thompson et al., 2018) and the variability and extent of warm water sources.

The major source of heat in the Southern Ocean, Circumpolar Deep Water (CDW), is transported by the Antarctic Circumpolar Current (ACC). The ACC connects all ocean basins around Antarctica (Rintoul et al., 2001) and contains various fronts. These fronts are defined by sharp transitions in water mass properties (Orsi et al., 1995; Kim and Orsi, 2014) and are termed over their meridional extent from north to south as the Subtropical Front (STF),

the Subantarctic Front (SAF), the Polar Front (PF), the Southern ACC Front (SACCF), and the Southern Boundary of the ACC (Orsi et al., 1995; Billany et al., 2010). The Southern Boundary of the ACC is the focus of this study and is globally defined as the southernmost limit of Upper Circumpolar Deep Water (UCDW, $\theta > 1.5^\circ$ and $S > 34.5$, Orsi et al. (1995)). In contrast to the Amundsen Sea further to the west, where evidence of a westward flowing Antarctic Slope Current (ASC) from observations and simulations exists (Zhang et al., 2016; Nakayama et al., 2018), the westward flow is absent in most of the Bellingshausen Sea and the WAP. As a result, the flow along the shelf break is dominated by the frontal jet associated with the Southern Boundary (Thompson et al., 2020). In the Bellingshausen Sea, the Southern Boundary is located in close proximity to the shelf break and is thus a crucial circulation feature that represents the southernmost barrier to mixing and regulates thermal conditions on the continental shelf (Naveira-Garabato et al., 2011; Yamazaki et al., 2021).

The southward extent of the Southern Boundary and its relation to the penetration of CDW onto the continental shelf of the Bellingshausen Sea are poorly investigated due to the lack of long-term observations and resulting lack of options to validate model output. However, the close proximity of the Southern Boundary to the Bellingshausen Sea continental shelf can increase the likelihood of cross-frontal mixing, which can impact the amount of heat accessing the continental shelf and reach ice shelf cavities located further south. Therefore, it is essential to improve the understanding of mechanisms and processes that impact the exchange processes between the Southern Boundary and continental shelf waters (CSW). This study further investigates the seasonal and interannual variability of the Southern Boundary in the Bellingshausen Sea. Its location with distance to the shelf break can vary based on changes in water mass properties, sea level pressure, local wind fields and/or non-local large-scale changes in the atmospheric circulation. The Ross Gyre, for instance, is one of the main current systems in the Southern Ocean that controls the proximity of warm waters of the ACC (Dotto et al., 2019; Roach and Speer, 2019). Another important factor is the Amundsen Sea Low, a semi-annual varying low pressure system in the Amundsen Sea that strongly impacts the atmospheric circulation and modulates the variability of sea ice concentration (Turner et al., 2013; Dotto et al., 2019). Moreover, relationships of the Southern Boundary to other climate indices such as the Southern Annular Mode (SAM) and the El-Niño-Southern-Oscillation (ENSO) are widely unknown. Therefore, temporal and spatial investigations of the Southern Boundary in the Bellingshausen Sea are crucial in understanding the role of the Southern Boundary in a changing

climate.

2.2 Data and Methodology

The hydrographic cross-slope transects (Fig. 2.1a) discussed in this study were observed during the research cruises JR165 in 2007 and NBP1901 in 2018/19 in the Bellingshausen Sea. In 2007, a total number of 262 full depth CTD profiles, including 3 cross-slope transects, were carried out between February 26th and April 16th using a CTD of the type Sea-Bird SBE 911 plus. As part of the research project TABASCO, 52 CTD profiles were accomplished between the 21st of December 2018 and the 23rd of January 2019, providing 2 cross-slope transects encircling the transects from 2007 (Fig. 2.1a). The operating CTD was a Sea-Bird SBE 9 Plus. The transects of potential temperature and practical salinity were used to identify water masses, define the Southern Boundary of the ACC with distance to the shelf break and to calculate geostrophic velocities referenced to observed current velocities measured by Shipboard and Lowered Acoustic Doppler Current Profilers (SADCP and LADCP).

The transects are projected onto a straight line and the coordinate system is rotated with respect to the transect, to accomplish a cross- and an along-slope component. The absolute along-slope geostrophic components are calculated and the geostrophic shear is referenced to the perpendicular component of the SADCP current velocities for the JR165 transects and to the LADCP current velocities for the NBP1901 transects after the tides were removed. M2 and S2 tides are removed using the Circum-Antarctic Tidal Simulation (CATS2008) with a uniform stereographic grid of 4 km provided by Earth & Space Research (DOI: 10.15784/601235, 2019). Tidal currents reach a maximum velocity of 2 cm s^{-1} on the continental shelf of the Bellingshausen Sea and show therefore only very little effects on the SADCP/LADCP data.

Furthermore, monthly data for each observed cross-slope transect such as potential temperature, practical salinity, absolute velocities and sea surface height (SSH) were extracted from the GLORYS12V1 reanalysis (DOI: 10.48670/moi-00021, 2020), hereinafter referred to as GLORYS. The monthly data are extracted from GLORYS over a time period from 2000 to 2018 (Fig. 2.1b). The model output was acquired through the Copernicus Marine Environmental Monitoring Service (CMEMS) and provides a global ocean eddy-resolving reanalysis with a horizontal resolution of $\frac{1}{12}^\circ$ ($\approx 3 \text{ km}$ in the Bellingshausen Sea region) and 50 vertical levels. GLORYS is based on the CMEMS forecasting system

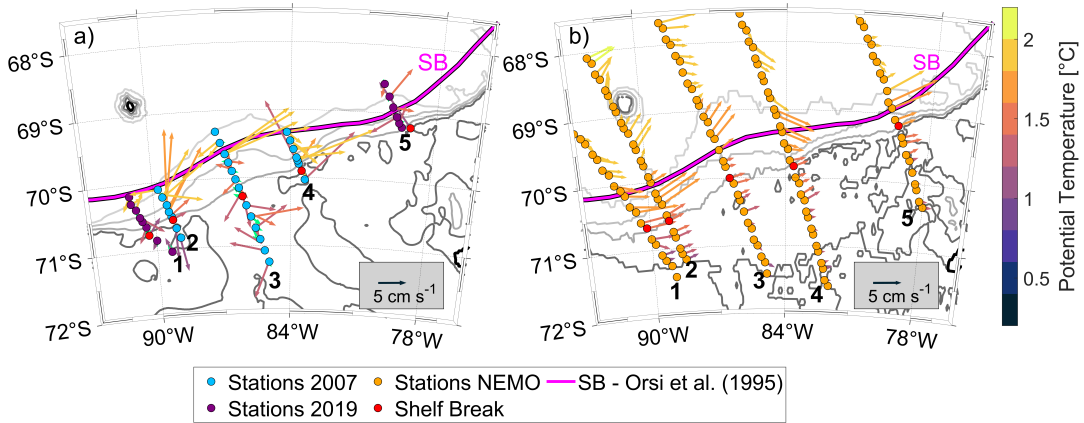


Figure 2.1: Map of cross-slope transects 1 to 5 for (a) observed stations from 2007 (blue) and 2019 (purple) and (b) stations extracted from GLORYS as monthly means from 2000 to 2018 (orange). The arrows mark the meridional and zonal velocities from SADC/LADCP data for the observations and velocities extracted from GLORYS that are averaged over the top 500 m and coloured by the temperature maximum. In (a) the M2 and S2 tides (green arrows) are calculated using the CATS2008 simulation. The Southern Boundary (magenta contour) is shown as defined by Orsi et al. (1995). The isobaths from (a) the IBCSO data set (Arndt et al., 2013) and (b) the GLORYS bathymetry are coloured in different shades of grey with the coastline (bold black), 500 m (black), 1000 m (dark grey), 2000 m (grey) and 3000 m (light grey) contours. The red dots show the station designated as the shelf break (closest to 1000 m) for each transect.

where the model component represents the NEMO platform driven at the surface by ECMWF ERA-Interim reanalysis. Furthermore, GLORYS assimilates data from observations such as sea level anomaly (SLA), satellite-based sea surface temperature (SST), sea ice concentration and in-situ temperature profiles. For more detailed information on GLORYS please see section 3.2 in Chapter 3.

The data from GLORYS are used in comparison with the observations to investigate how accurately the model represents water masses, stratification and current structures across the Southern Boundary. Due to the lack of long-term observations in hardly accessible regions such as the Bellingshausen Sea, GLORYS is further used to investigate the spatial and temporal variability of the Southern Boundary along the continental slope of the Bellingshausen Sea. The spatial and temporal analysis of the Southern Boundary is based different possible definitions of the Southern Boundary one of which is the definition by Orsi et al. (1995) ($\theta > 1.5^\circ\text{C}$ in a depth of about 200 m). This study further introduces a definition of the Southern Boundary based on the subsurface temperature maximum ($\theta_{\max} > 1.7^\circ\text{C}$, independent of depth). Our reasoning for introducing the alternative definition is based on slightly warmer temperatures of CDW represented in GLORYS (see chapter 2 section 2.3 for further details). In the

following, the seasonal and interannual variability of the Southern Boundary in the Bellingshausen Sea is investigated in more detail, where the distance of the Southern Boundary to the shelf break and the southward extent of warm waters ($\theta_{\max} > 1.5^\circ\text{C}$, independent of depth) are brought into context.

2.3 Hydrography and Frontal Structure of the Bellingshausen Sea across the Shelf Break and Slope

The observed hydrographic properties in the Bellingshausen Sea at the transition from shelf to open water in the upper 1500 m can be subdivided into 3 different water masses (transects 1 and 4, Fig. 2.2a-c and g-i). At the surface all observed transects show a relatively fresh surface mixed layer near the freezing point. The water mass properties agree with findings from Carter et al. (2008) and Zhang et al. (2016) and represent the Antarctic Surface Water (AASW). The vertical extent of AASW varies in depth and extends deeper into the water column on the continental shelf and across the continental slope than further offshore. In transect 1, AASW extends to a depth of about 250 m across the shelf break and slope and shallows to about 150 m with greater distance to the shelf break. In transect 4, AASW is overall shallower and extends from 150 m at the shelf break and shallows to 100 m further north. Transect 4 demonstrates a warmer surface layer from the shelf break northwards, which indicates surface warming in summer. Further offshore $\theta_{\max} \approx 1.85^\circ\text{C}$ along with an oxygen minimum (not shown) indicates Upper Circumpolar Deep Water (UCDW) extending from 200-800 m. The transition from colder CSW and warmer off-shelf waters is also characterised by the tilted 27.8 kg m^{-3} isopycnal shallowing towards the slope. On the continental shelf, a water mass slightly fresher and colder than UCDW is identified as modified Circumpolar Deep Water (mCDW) (Thompson et al., 2020; Schulze-Chretien et al., 2021). The layer of mCDW is located below the AASW layer and extends down to the seabed. In comparison, the long-term mean of the water mass properties extracted from GLORYS (transects 1 and 4, Fig. 2.2d-f and j-l) demonstrate similar hydrographic stratification and all key water masses are represented. However, the AASW is with a depth of about 100 m slightly shallower than shown by the observed transects. Additionally, the transition from CSW to UCDW is less sharp in GLORYS than in the observations but the shallowing of the 27.8 kg m^{-3} isopycnal spans over

a broader region (at least in transect 1). The southern extent of UCDW in GLORYS is about 8 to 10 km closer to the shelf break than in the observations.

All observed transects show the southern limit of UCDW in association with an eastward flow (Fig. 2.2). The velocities of the flow vary between 5 to 10 cm s⁻¹ in its core. The eastward flow varies in distance to the shelf break for each transect and extends from the surface to a depth of about 1000 m. In addition to the eastward flow, transect 1 (Fig. 2.2c) and 2 (not shown), located in the western Bellingshausen Sea, present a bottom intensified westward flow slightly below the UCDW layer and very close to shelf break and slope. This bottom-intensified westward flow is thought to be a first initiation of the ASC in the West Antarctic Circulation System (Thompson et al., 2020). Transect 1 extracted from GLORYS in the western Bellingshausen Sea does not show a bottom intensified westward flow (Fig. 2.2f). There is only a very weak indication of a westward flow at the shelf break in a depth of about 1000 m. The core eastward flow is in nearly the same location as in the observations, but reaches further offshore. Note that the identified differences between the observed transects and the transects extracted from GLORYS are expected when comparing observations to long-term means or even reanalysis data. The coarser resolution provided by GLORYS may not resolve small scale changes in stratification and circulation features. The bathymetry from GLORYS and observed transects differs significantly in some areas of the continental shelf, shelf break and slope. The GLORYS bathymetry at the shelf break and slope is up to 300 m deeper than in the observed transects predominantly in the western Bellingshausen Sea, whereas south of 71°S the GLORYS bathymetry, is shallower than available bathymetric data products (e.g. R-Topo2, (Schaffer et al., 2016)) suggest, specifically within the major throughs as described in section 3.2. It is acknowledged that a deeper bathymetry near the shelf break can increase the access of warm waters onto the continental shelf. Differences in bathymetry may further impact the overall structure and strength of the flow patterns in GLORYS. Thus there is scope for future work by investigating the flow patterns using a model or reanalysis with improved bathymetry.

The southern limit of UCDW is globally defined as the Southern Boundary with $\theta > 1.5$ °C in a depth of about 200 m by Orsi et al. (1995) and is well documented as a source of warm waters leading to sea ice melt in previous studies (Nakayama et al., 2018; Zhang et al., 2016; Dinniman et al., 2012). However, the water mass properties around Antarctica change in time and space (e.g. Auger et al., 2021). Therefore, the approach of defining the Southern Boundary based on the temperature maximum of UCDW independent of depth

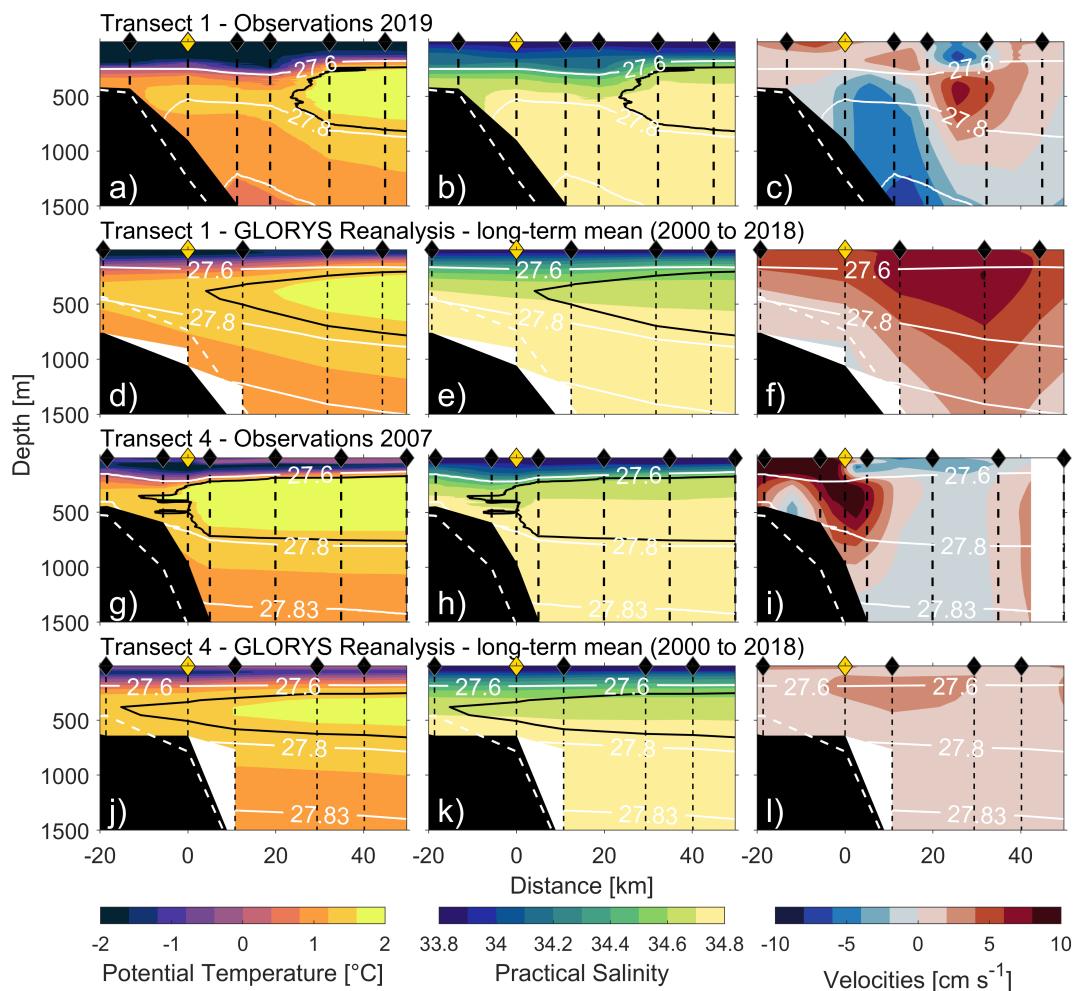


Figure 2.2: Observed hydrographic cross-slope transects 1 (a-c) and 4 (g-i) and long-term means extracted from GLORYS for the same transect locations. Transect 1 (d-f) and 4 (j-l) show the potential temperature (left panel, a-j), practical salinity (middle panel, b-k) and geostrophic velocities (right panel, c-l). The bold white contours show potential density and the black contour marks the temperature of 1.5 °C. The dashed white line indicates the bathymetry based on the IBCSO data set (Arndt et al., 2013)) and the black-shaded area presents the bathymetry based on the observed depth at each station or the GLORYS bathymetry. Eastward velocities are defined as positive.

provides a more locally accurate definition of the Southern Boundary in the Bellingshausen Sea. θ /S-Diagrams (not shown) indicate UCDW with a temperature of $\theta_{\max} \approx 1.85^\circ \text{C}$ for the observations and $\theta_{\max} \approx 1.7^\circ \text{C}$ for GLORYS. A water mass modification in GLORYS over time can be ruled out. The differences in UCDW temperature between observations and GLORYS may indicate a temperature bias in GLORYS. This bias does not necessarily influence the general dynamics found in the Bellingshausen Sea region, but has to be considered for the definition of the Southern Boundary. In all observed and simulated transects, the Southern Boundary is identified which supports the existence of a consistent structure containing UCDW close to the shelf break.

2.4 Location of the Southern Boundary in the Bellingshausen Sea

The long-term mean of GLORYS, generated by monthly means from 2000 to 2018, represents the long-term mean conditions of potential temperature and flow dynamics of the Bellingshausen Sea (Fig. 2.3a,b). The two different definitions of the Southern Boundary investigated in this study include the global definition of UCDW ($\theta > 1.5^\circ$ at a depth of about 200 m, Orsi et al. (1995)) and an adaption for GLORYS using $\theta_{\max} > 1.7^\circ\text{C}$ independent of depth. The southernmost extent of water masses exceeding $\theta_{\max} > 1.5^\circ\text{C}$ are defined independent of depth. In the long-term mean (Fig. 2.3), the Southern Boundary demonstrates spatial variations with respect to its distance to the shelf break. Both definitions of the Southern Boundary are aligned and located in the centre of the eastward flow associated with the Southern Boundary. The eastward flow is confined to the region between the 1000 m and 3000 m isobaths, where largest distances of the Southern Boundary to the shelf break are found between 82-87°W following the topography. Minimum distances of the Southern Boundary to the shelf break are found in the eastern Bellingshausen Sea between 78-82°W. In this area, the southernmost extent of warm waters is found in close proximity to the shelf break on the eastern Bellingshausen Sea continental shelf.

Aside from purely spatial variations of the Southern Boundary in the Bellingshausen Sea, temporal variations also highlight dramatic changes in the location of the Southern Boundary with distance to the shelf break. Demonstrating the variability pattern of the Southern Boundary is challenging, as the temporal variations are dominated by interannual rather than seasonal variability and

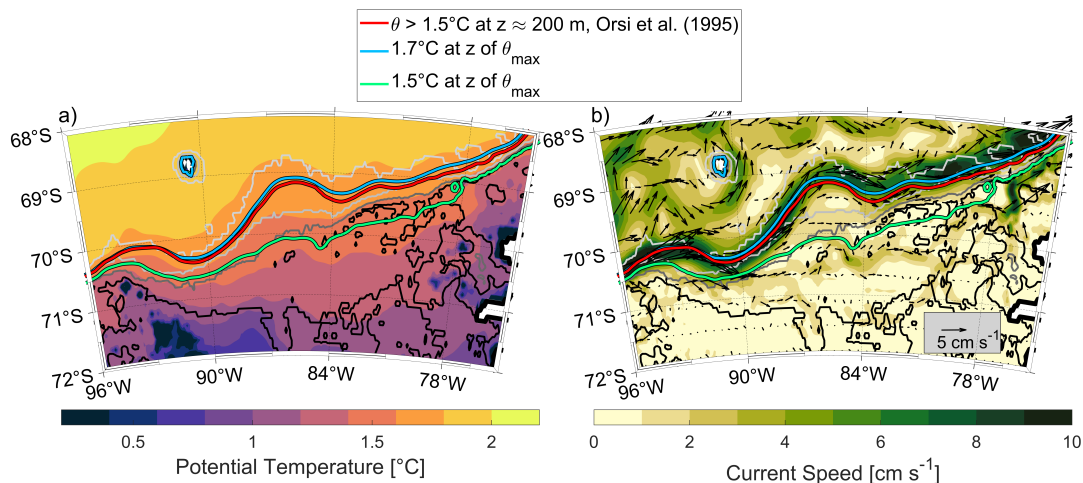


Figure 2.3: Map of the Bellingshausen Sea showing (a) temperature maximum and (b) speed of the long-term mean extracted from GLORYS. The red and blue contours mark two different definitions of the Southern Boundary with $\theta > 1.5^\circ\text{C}$ at a depth of about 200 m (red) as defined by Orsi et al. (1995) and $\theta_{max} > 1.7^\circ\text{C}$ at the depth of the temperature maximum (blue). The green contour indicates the southernmost extent of warm water masses exceeding $\theta_{max} > 1.5^\circ\text{C}$ at the depth of the temperature maximum. The isobaths are coloured as in Fig. 2.1b.

are dependent on many factors, such as lateral structure of temperature, current speed and wind stress curl (Fig. 2.4a-l).

From 2000 to 2018, three major stages highlight the strong spatial and temporal variability of the Southern Boundary in the Bellingshausen Sea. The differences between these three stages are far greater than the seasonal variability (see section 2.5), so here we ignore seasonality. The first stage (Fig. 2.4a-c and j-l) represents the conditions that occur most commonly over the time period considered and are thus fairly comparable to the long-term mean conditions. The two definitions of the Southern Boundary are meandering differently than in the long-term mean, but both remain aligned along the Bellingshausen Sea continental slope region and both are located in the centre of the eastward flow. The eastward flow is continuous from west to east and shows no interruptions of the flow pattern. The wind stress curl (Fig. 2.4c,l) is calculated from the wind field extracted from ERA5 (DOI: 10.24381/cds.f17050d7, 2020) and demonstrates weakly negative values in the eastern Bellingshausen Sea (78-82°W). A weakly negative wind stress curl can suggest a weak uplift of isopycnals near the shelf break, which can support the access of warm waters onto the continental shelf. The uplift of isopycnals enhancing the access of warm waters onto the continental shelf has been demonstrated to be an important indicator in previous studies in the West Antarctic Sector and the Amundsen Sea (e.g. Schmidtko et al., 2014; Dotto et al., 2019).

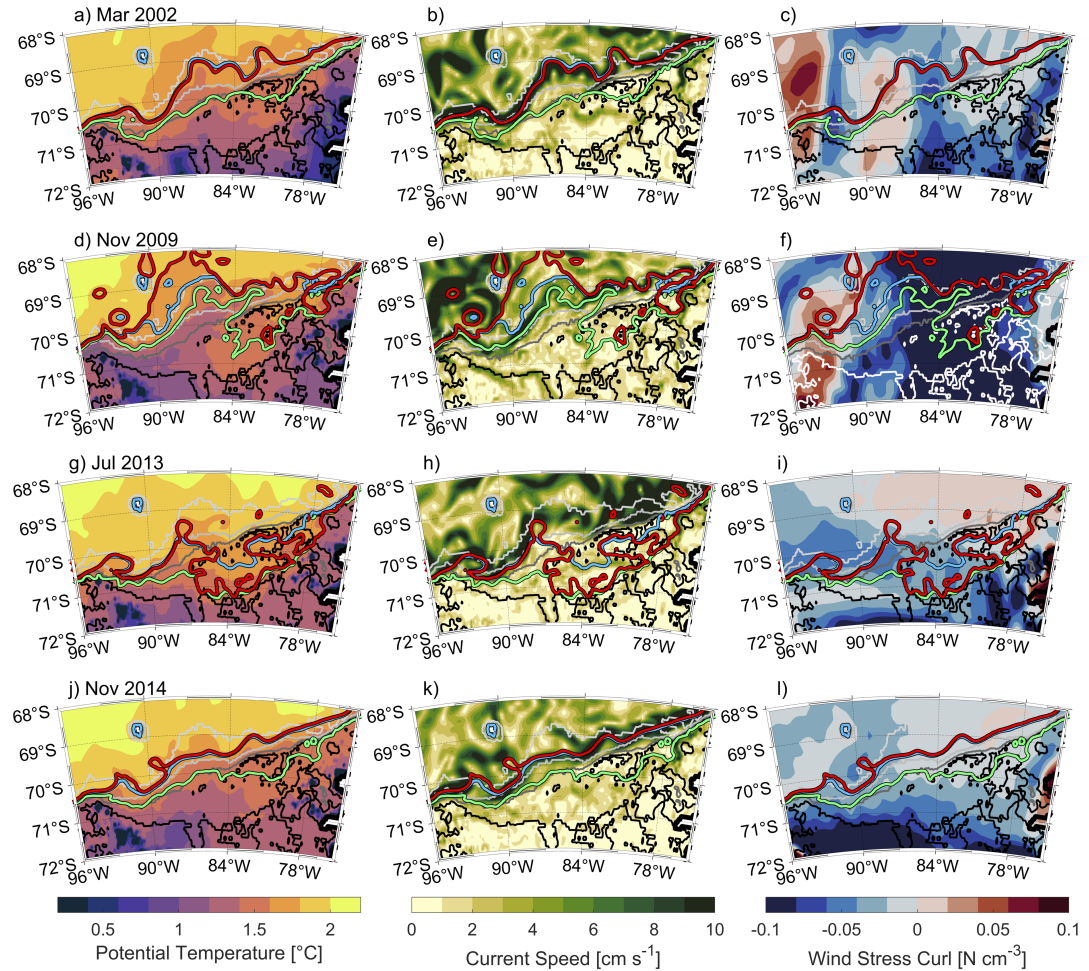


Figure 2.4: Example of monthly means from GLORYS for (a-c) March 2002, (d-f) November 2009, (g-i) July 2013 and (j-l) November 2014 marking different stages of the Southern Boundary's location. The subfigures show potential temperatures (left panel, a-j), current speed (middle panel, b-k) and wind stress curl (right panel, c-l). Potential temperatures and current speeds are shown at the depth of the temperature maximum. The wind stress curl is calculated from the wind field extracted from ERA5. The red and blue contours mark two different definitions of the Southern Boundary with $\theta > 1.5^\circ\text{C}$ at a depth of about 200 m (red) as defined by Orsi et al. (1995) and $\theta_{\max} > 1.7^\circ\text{C}$ independent of depth (blue). The green contour indicates the southernmost extent of warm water masses exceeding $\theta_{\max} > 1.5^\circ\text{C}$ independent of depth. The isobaths are coloured as in Fig. 2.1b.

The second stage (Fig. 2.4d-f) displays distances of the Southern Boundary to the shelf break in the western Bellingshausen Sea along with a northward displacement of both Southern Boundary contours (Fig. 2.4d-f, red and blue contours), whereas the northward displacement is much greater in the Southern Boundary contour defined with $\theta > 1.5^\circ\text{C}$ at a depth of about 200 m (Fig. 2.4d-f, red contour). Both Southern Boundary contours are dislocated from the eastward flow along the shelf break. The wind stress curl in the eastern Bellingshausen Sea is strongly negative suggesting a stronger uplift of isopycnals than in the first stage shown before. This stronger uplift of isopycnals potentially explains the increased extent of warm water on the Bellingshausen Sea continental shelf (Fig. 2.4f, green contour) as compared to the previous stage. Further analysis of the GLORYS timeseries suggests an inflow of cold surface waters originating from the Amundsen Sea and extending to a depth of 200-300 m (not shown). This could be a potential explanation for the strong dislocation of both Southern Boundary contours predominantly in the western Bellingshausen Sea. Although the strongly negative wind stress curl suggests a significant change in the atmospheric circulation predominantly in the eastern Bellingshausen Sea, the inflow of cold surface waters from the Amundsen Sea does not indicate a local cause. Furthermore, there are no available observations for this time period in the Bellingshausen Sea region. Thus inflowing cold water masses originating from the Amundsen Sea can not be confirmed for the real ocean.

The third stage occurs in July 2013 where both Southern Boundary contours extend furthest onto the Bellingshausen Sea continental shelf (Fig. 2.4j-l). The southward shift of the Southern Boundary occurs predominantly in the eastern and central Bellingshausen Sea. In this region, both Southern Boundary contours are not aligned with the eastward flow near the shelf break. The eastward flow further demonstrates a strong current speed pattern between $79.5\text{-}80^\circ\text{W}$. During this stage, the southward shift of the Southern Boundary can cause warm waters to penetrate the continental shelf nearly unrestricted. If the warm water masses accessing the shelf were to reach ice shelf cavities located in the southern Bellingshausen Sea the result would be rapid ice shelf melt. Moreover, the wind stress curl (Fig. 2.4l) appears much weaker compared to previous years. The general warming of the continental shelves within the West Antarctic sector between the years 2012 and 2014 and the penetration of off-shelf CDW, or its colder modified variants (mCDW), onto the shelf agrees with findings by Nakayama et al. (2018) and Schmidtke et al. (2014), who relate the warming of the West Antarctic continental shelves to a strong La Niña event.

2.5 Variability of the Southern Boundary

2.5.1 Seasonal Variability

The seasonal variability of the Southern Boundary with distance to the shelf break is estimated for both definitions of the Southern Boundary and for southernmost extent of warm waters at all transect locations in the Bellingshausen Sea shown in Fig. 2.1. The seasonal variability of the Southern Boundary is calculated using climatologically-averaged monthly means extracted from GLO-RYS over the time period from 2000 to 2018. The transects in the western Bellingshausen Sea (transects 1 to 2) show similar patterns for both definitions of the Southern Boundary (Fig. 2.5a, example transect 1). The standard deviation of the monthly means increases in winter months indicating a stronger interannual variability. In contrast, transects in the central and eastern Bellingshausen Sea (transects 3, 4 and 5) present a different signal. At first, the both Southern Boundary definitions display a similar trend towards minimum distances to the shelf break in winter months (Fig. 2.5b, example transect 4), but the two definitions are not in the same location and show the Southern Boundary defined with $\theta_{\max} > 1.7^{\circ}\text{C}$ up to 50 km further north than the Southern Boundary defined with $\theta > 1.5^{\circ}\text{C}$ at a depth of about 200 m (Fig. 2.5b, blue and red dots). The Southern Boundary based on $\theta > 1.5^{\circ}\text{C}$ in a depth of about 200 m is closer to the shelf break for transects 4 and 5 consistently, but indicates a larger monthly standard deviation. In contrast to transects 4 and 5, transect 3 (not shown) presents larger distances of the Southern Boundary to the shelf break as it is located in the region where in general largest distances of the Southern Boundary to the shelf break are found due to the eastward flow following the topography.

Billany et al. (2010) observed maximum distances to the shelf of the Southern Boundary during winter months (May to August) and minimum distances during summer months (November to January) at the Greenwich Meridian in the Weddell Sea based on a timeseries of altimetry data from 1993 to 2008. This seasonal pattern is recognisable in the western Bellingshausen Sea. However, the investigations on seasonal variability of the Southern Boundary highlight that the seasonal variability pattern varies significantly on a local scale and emphasise that significantly more long-term observations are needed to understand the seasonal and spatial variability of the Southern Boundary around Antarctica.

The southernmost limit of warm waters ($\theta_{\max} > 1.5^{\circ}\text{C}$) (Fig. 2.5, green

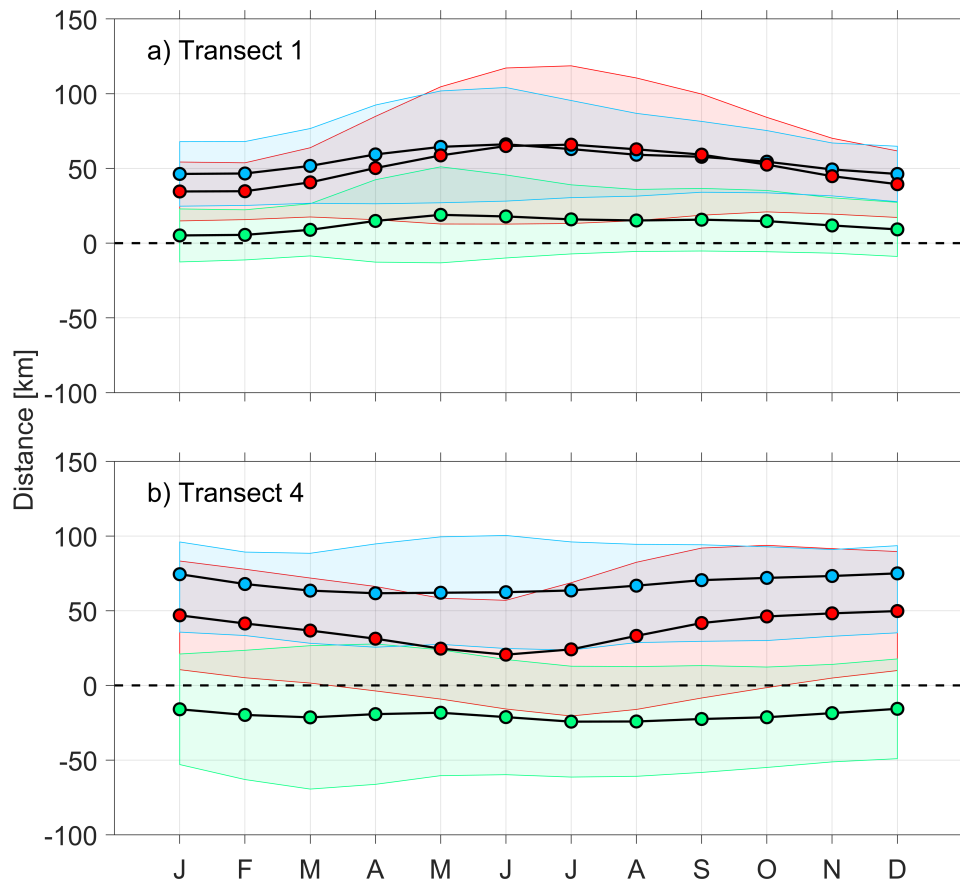


Figure 2.5: Example of calculated seasonal cycles of (a) transect 1 and (b) transect 4 with shaded standard deviations marking the shift of the Southern Boundary with distance to the shelf break. The seasonal cycles are calculated by climatologically-averaging the monthly output from GLORYS for each of the transects within the time period from 2000 to 2018. The red and blue dots mark the two different definitions of the Southern Boundary with $\theta > 1,5^{\circ}\text{C}$ at a depth of about 200 m after Orsi et al. (1995) (red dots) and $\theta_{\max} > 1.7^{\circ}\text{C}$ independent of depth (blue). The green dots indicate the southward extent of warm waters and are defined with $\theta_{\max} > 1.5^{\circ}\text{C}$ independent of depth.

dots) displays a spatial evolution from west to east. In the western Bellingshausen Sea (transects 1 and 2) the seasonal cycles show warm water masses off the continental shelf throughout, where transect 1 shows largest distances of warm waters to the shelf break. Transect 3 (not shown) could be determined as a transition zone, with access of warm waters to the shelf predominantly in winter months. Transects 4 and 5 demonstrate warm waters with access onto the continental shelf throughout the year and indicate only weak seasonal variability.

Overall, the seasonal variability of the Southern Boundary definitions and the southernmost limit of warm waters is fairly weak with maximum displacements of the Southern Boundary of 50 km, at least in GLORYS. Nevertheless, they provide a small contribution of shifts in the location of the Southern Boundary in its southward extent. However, there are substantial interannual shifts of the Southern Boundary that dominate over its seasonal variability.

2.5.2 Interannual Variability and Relation to Warm Water Penetration onto the Shelf

Considering the displacements of the Southern Boundary and warm water intrusions onto the shelf on an interannual time scale are aimed to provide more information on possible relations to changing current structures, water mass formation and large-scale events occurring in the atmospheric circulation. Aside from small-scale fluctuations from 2000 to 2018, the Southern Boundary and the southward extent of warm waters in GLORYS demonstrate strong interannual variability. The strong interannual variability is apparent in all transects extracted from GLORYS, whereas variability patterns differ between the western and eastern Bellingshausen Sea (Figs. 2.6 and 2.7). Particularly the years from 2008 to 2010 and from 2012 to 2014 demonstrate two major patterns of different variability in different parts of the Bellingshausen Sea.

The first event from 2008 to 2010 shows greater distances of the Southern Boundary to the shelf break in the western and central Bellingshausen Sea with distances to the shelf break of up to 220 km (Fig. 2.6, example transect 1). In addition, potential temperature at the depth of the temperature maximum (Fig. 2.6a) decreases by about 0.3°C which is accompanied by an increase in practical salinity (Fig. 2.6b) on the continental shelf. Furthermore, a rather weak change in SSH from -1.6 m to -1.62 m, a interrupted speed pattern and a deepening of the temperature maximum off the shelf break, are identifiable during that time (Fig. 2.6c-e). This event corresponds with the second stage of the Southern

Boundary introduced in section 2.4. The signal of a northward displacement of the Southern Boundary weakens spatially from west to east and there is no clear indication of a northward displacement for the easternmost transects (transects 4 and 5).

Subsequently the event from 2012 to 2014 demonstrates the Southern Boundary with access of up to 100 km on the Bellingshausen Sea continental shelf. This southward shift is indicated by both definitions of the Southern Boundary and coincides with the southernmost extent (up to 190 km) of warm waters onto the continental shelf throughout the time period. The warming of the continental shelf is accompanied by a weak increase in SSH to -1.6 m (thermal expansion). An important factor to note is further that the eastward flow associated with the Southern Boundary along the shelf break and slope has not shifted south and is thus not aligned with the Southern Boundary during this time period. These findings correspond to the third stage of the Southern Boundary locations described in section 2.4. A signal of this variability pattern is identified in transects 3 to 5, whereas it is absent for the westernmost transects 1 and 2.

Correlations of the Southern Boundary with distance to the shelf break and climate indices such as the Southern Annular Mode (SAM), Multivariate ENSO Index (MEI), Southern Oscillation Index (SOI) and the Amundsen Sea Low Index do not show a clear relation and only weakly correlate ($r < 0.3$). The weak correlation to shifts of the Southern Boundary to SAM and MEI agrees with findings from Billany et al. (2010). However, there is a strong relation between the distance of the Southern Boundary to the shelf break and the southward extent of warm waters on the Bellingshausen Sea continental shelf for all transects ($r > 0.6$). This indicates a dependency of the Southern Boundary's location and the penetration of warm waters onto the continental shelf. This relation gains importance as warm waters have access to the eastern continental shelf continuously throughout the considered time period.

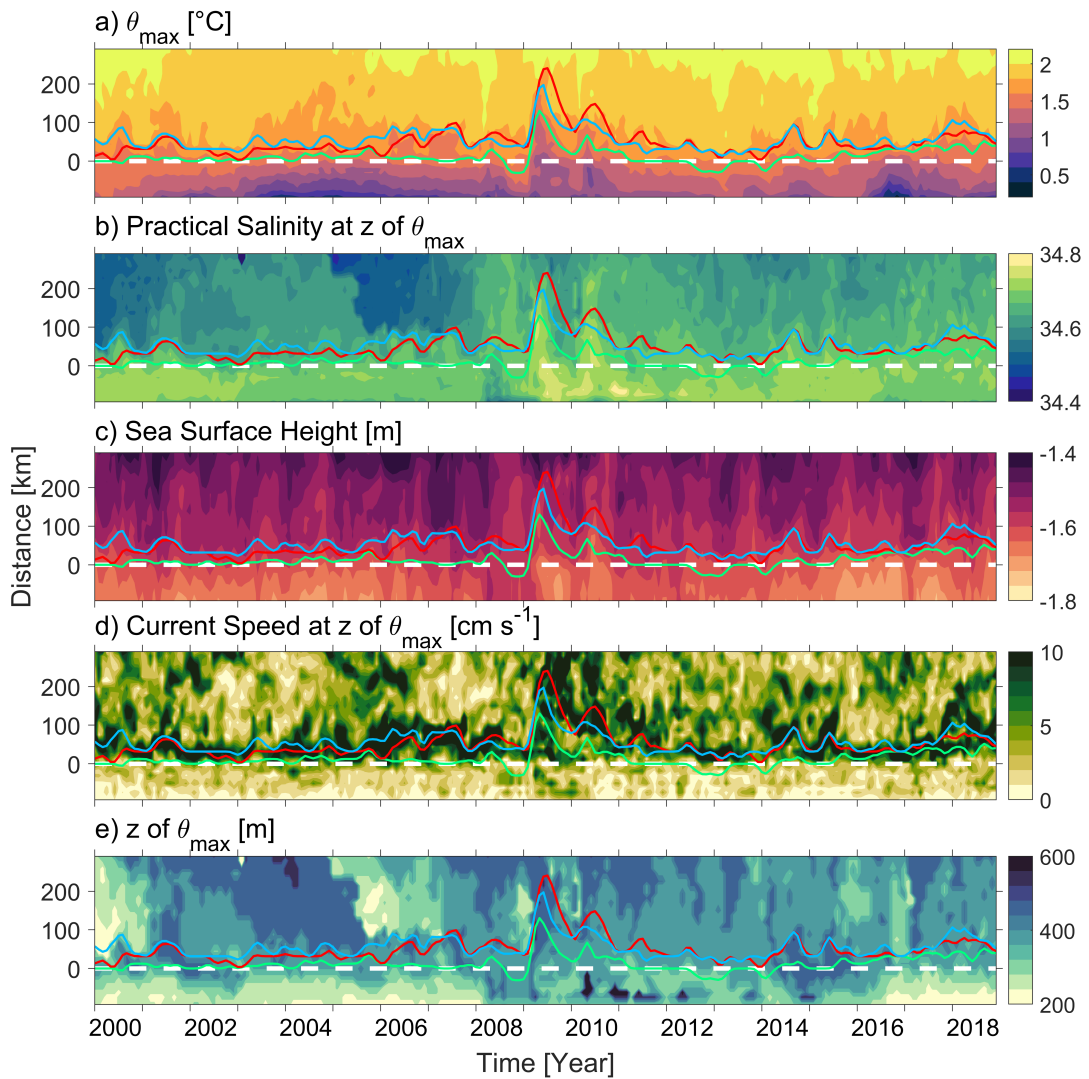


Figure 2.6: Hovmöller-Diagram of transect 1 extracted from GLORYS from 2000 to 2018 showing (a) potential temperature, (b) practical salinity, (c) SSH, (d) current speed and (f) depth of the temperature maximum against distance to the shelf break. The contours of the Southern Boundary definitions and the southern extent of warm waters are coloured as in Fig. 2.3.

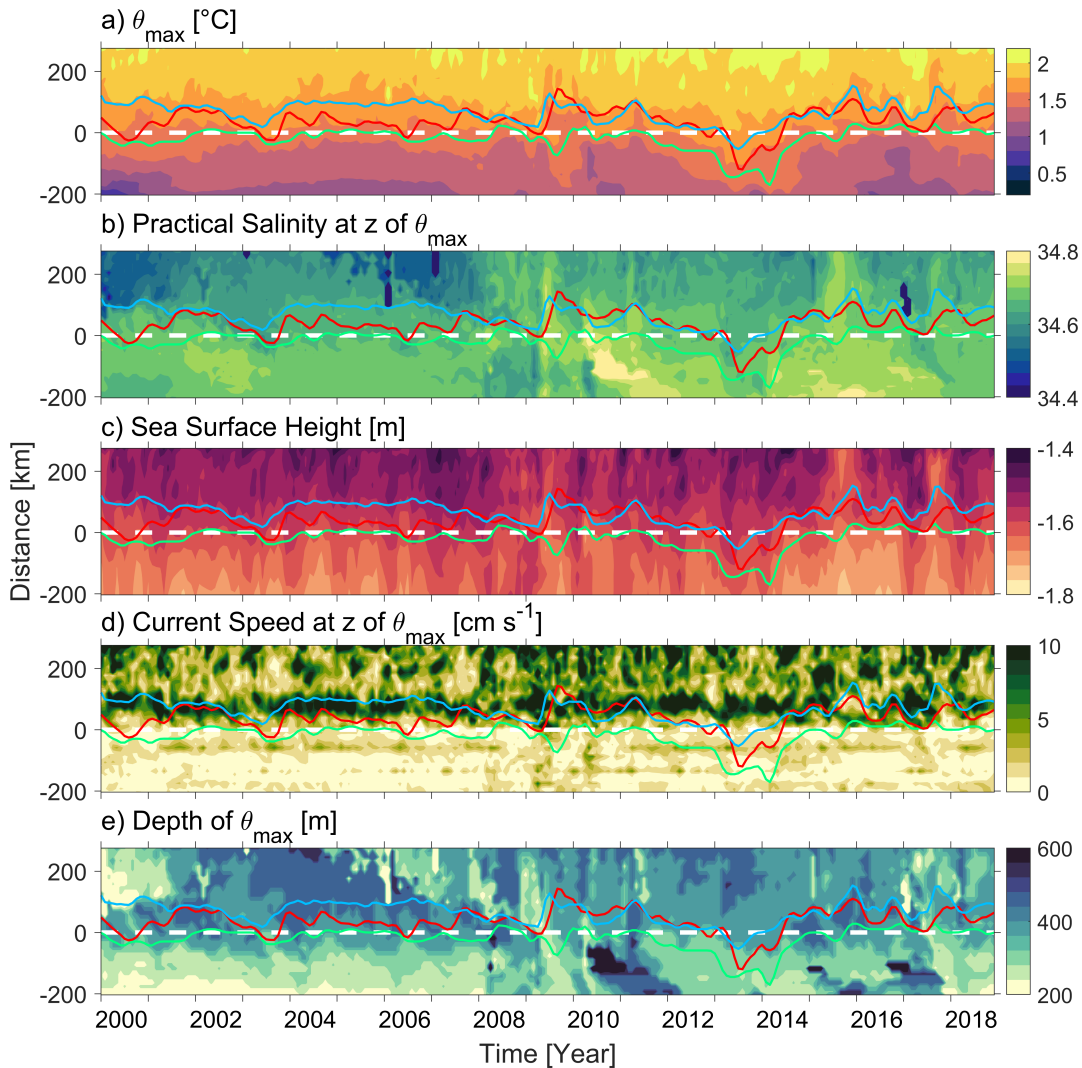


Figure 2.7: Hovmöller-Diagram of transect 4 extracted from GLORYS from 2000 to 2018 showing (a) potential temperature, (b) practical salinity, (c) SSH, (d) current speed and (f) depth of the temperature maximum against distance to the shelf break. The contours of the Southern Boundary definitions and the southern extent of warm waters are coloured as in Fig. 2.3.

2.6 Summary and Conclusions

In this study, observations of hydrographic cross-slope transects from 2007 and 2018/19 are used in comparison to transects extracted from GLORYS. Firstly, the aim was to establish the representation of water masses, stratification and flow structures in GLORYS. Due to the persistent warming of continental shelf waters in the West Antarctic sector associated with the melting of ice shelves, this study focused on the southernmost boundary of UCDW, the Southern Boundary. Previous studies have demonstrated that the ASC as part of the Antarctic Slope Front is absent in most of the Bellingshausen Sea and therefore the Southern Boundary dominates the Bellingshausen Sea shelf break and

slope region associated with an eastward flow. The Southern Boundary and its spatial and temporal variability are thus important features to consider when investigating the spatial and temporal variability of warm waters accessing the Bellingshausen Sea continental shelf.

In general, we found the hydrography from the observations is fairly comparable to the hydrography in GLORYS. Main water masses such as AASW, CDW and mCDW are represented within the reanalysis and nearly in the same location as shown in observed hydrographic transects (Fig. 2.2). Differences occur when comparing the flow patterns which are very likely to be related to the coarser horizontal and vertical resolution provided by GLORYS, the comparison to long-term means (features of smaller scale have likely been smoothed out or not been reproduced in GLORYS) and differences in bathymetry between GLORYS and observations. Large troughs such as the Belgica and Latady troughs are not clearly resolved in the reanalysis bathymetry. For future investigations, a reanalysis with a higher resolution and more recent bathymetry might help to improve the representation of flow patterns in GLORYS.

Due to the significant lack of long-term observations, we further analysed the Southern Boundary and its variability in GLORYS. For defining the Southern Boundary we used the global definition from Orsi et al. (1995), $\theta > 1.5^{\circ}\text{C}$ at a depth of about 200 m, and an adapted version for GLORYS, $\theta_{\text{max}} > 1.7^{\circ}\text{C}$ independent of depth. Both definitions of the Southern Boundary are aligned over the majority of the time period from 2000 to 2018 and are mostly located in the centre of the eastward flow along the shelf break. The long-term mean of the two Southern Boundary definitions highlighted spatial variations along the shelf break. Maximum distances of the Southern Boundary to the shelf break were found between 82-87°W, whereas minimum distances of the Southern Boundary to the shelf break were identified in the eastern Bellingshausen Sea. Additionally, the southward extent of warm waters was defined as $\theta_{\text{max}} > 1.5^{\circ}\text{C}$ independent of from depth, which was found to have almost continuous access to the continental shelf of the eastern Bellingshausen Sea throughout the time period from 2000 to 2018. The southward extent of warm waters on the continental shelf was mostly restricted to areas near the shelf break.

The Southern Boundary presented overall weak seasonal variability in comparison to strong interannual events in the years from 2008 to 2010 and 2012 to 2014. However, a clear identification of the processes unfolding these the events and the resulting variability of the Southern Boundary could not be identified in this study. Correlations to various climate indices do not demonstrate a

clear relation to the variability of the Southern Boundary and its distance to the shelf break. Nevertheless, we identified a close relationship between the distance of the Southern Boundary to the shelf break and the southward extent of warm waters on the continental shelf ($r > 0.6$). Investigating the access of warmer waters onto the continental shelf in response to a southward shift of the Southern Boundary is an important area of research, specifically in areas where the Southern Boundary is located close to the continental shelf of Antarctica. However, more observations are needed to confirm the relationship between the location of the Southern Boundary and the southward extent of warm waters in the Bellingshausen Sea for the real ocean. To quantify the role of the Southern Boundary in a changing climate, it is further necessary to understand the main drivers of its variability. This can only be accomplished with more long-term observations, such as transects of moorings crossing the Southern Boundary over a wider area along the shelf break. Future glider campaigns are needed to capture the Southern Boundary's frontal structure repeatedly and highly resolved and the deployment of surface drifters and floats would help to quantify the role of eddies impacting the Southern Boundary's frontal structure and location. We further suggest investigations of satellite-based sea ice concentrations in comparison to the Southern Boundary with distance to the shelf break that can potentially increase our understanding of how and to what extent the Southern Boundary impacts the northward sea ice extent.

Although this study has highlighted the close relationship between the Southern Boundary and southward extent of warm waters in specifically the eastern Bellingshausen Sea, it has not been shown whether the temperature of water masses in southern Bellingshausen Sea is affected by a southward shift of the Southern Boundary. The following chapter therefore investigates the spatial and temporal variability of temperatures and driving mechanisms in the southern Bellingshausen Sea.

Chapter 3

Wind-induced Variability of Warm Water on the Bellingshausen Sea Continental Shelf

This chapter has been published in the *Journal of Geophysical Research: Oceans*. The text in the chapter is included as published with the same title (Oelerich et al., 2022). R. Oelerich was responsible for the work, under supervision of Karen J. Heywood, Gillian M. Damerell and Andrew F. Thompson, who provided scientific input and helped to revise the text for publication.

3.1 Introduction

The major oceanic source of heat onto the Antarctic continental shelf is Circumpolar Deep Water (CDW) circulating eastward within the Antarctic Circumpolar Current (ACC). Surface heat and freshwater fluxes can also make a significant contribution to regional budgets and modify stratification that also feeds back on the geostrophic circulation and associated tracer transport (Couto et al., 2017). The southernmost part of the Antarctic Circumpolar Current is generally considered to play an important role in bringing warm water onto the continental shelf particularly in the west Antarctic shelf seas (e.g., Jenkins and Jacobs, 2008; Dinniman and Klinck, 2004; Martinson and McKee, 2012). Here we consider the Bellingshausen Sea (Fig. 3.1), where the Antarctic Circumpolar Current approaches most closely to the shelf break (e.g., Jenkins and Jacobs, 2008; Thompson et al., 2020; Schulze-Chretien et al., 2021).

CDW is the main water mass that has been associated with the thinning of West Antarctic ice shelves through basal melt (e.g. Paolo et al., 2015; Cook et al., 2016). Troughs on the continental shelf of Antarctica provide direct routes for CDW, or slightly colder modified CDW (mCDW), to gain access to coastal regions (Wåhlin et al., 2010; Jacobs et al., 2011). The Bellingshausen

Sea lies between two more well-studied regions, the Amundsen Sea to the west and the West Antarctic Peninsula (WAP) to the east, where unmodified CDW ($\theta > 1.5^\circ\text{C}$) can access the deeper troughs on the shelf (e.g., Dotto et al., 2019; Martinson and McKee, 2012; Jenkins and Jacobs, 2008). Shoreward transport across the shelf can enable mCDW ($\theta < 1.5^\circ\text{C}$) to reach deep cavities below the ice shelves inducing a retreat of their grounding lines (Dutrieux et al., 2014; Jenkins et al., 2010; Konrad et al., 2018).

Most of the ice shelves along the coast of the southern Bellingshausen Sea have experienced a significant loss in volume and increased basal melt rates over the past decades (Rignot et al., 2019; Hogg et al., 2017; Paolo et al., 2015), and ocean forcing has been implicated. Jenkins and Jacobs (2008) observed mCDW with a temperature warmer than 1°C flooding the Bellingshausen Sea continental shelf and an inflow of warm water into the ice shelf cavities. Schulze-Chretien et al. (2021) analysed ship-based observations and showed that submarine troughs provide topographically-steered pathways for mCDW from the shelf break towards the deep embayments close to the floating ice shelves. mCDW enters the continental shelf through the eastern side of one of the Bellingshausen Sea's major troughs, the Belgica Trough (Fig. 3.1c). Seal-acquired observations have indicated a cyclonic circulation within this trough with flow extending towards the coast along its eastern boundaries and returning to the shelf break along western boundaries (Zhang et al., 2016). Model studies and seal-acquired observations have provided evidence for a coherent westward current along the Bellingshausen Sea coastline, the Antarctic Coastal Current acting as a link between the WAP and the Amundsen Sea (Schubert et al., 2021; Holland et al., 2010).

Around much of Antarctica, the Antarctic Slope Current (ASC) provides westward transport along the continental slope. Beneath it, the Antarctic Slope Undercurrent, a bottom-intensified current, flows eastward (Chavanne et al., 2010). The formation and persistence of the ASC is mostly attributed to surface wind stress, and the intensity and variability of the ASC largely control the rate at which heat associated with CDW moves across the slope and onto the continental shelf (Thompson et al., 2018). Wind-driven variations in intensity of the Antarctic Slope Undercurrent have been suggested as a mechanism for the transport of heat into major troughs of the Amundsen Sea (Dotto et al., 2020; Walker et al., 2013).

In contrast, the ASC is absent in the central and eastern Bellingshausen Sea (Thompson et al., 2018), as it is in the WAP. There are insufficient observations to determine if the Antarctic Slope Undercurrent is a persistent feature in this

section of the Antarctic continental shelf (Thompson et al., 2018). These arguments suggest that mechanisms for heat transport onto the continental shelf may differ from those of the Amundsen Sea. The eastward flow marking the southern limit of the Antarctic Circumpolar Current (Thompson et al., 2020) is found in close proximity to the shelf break in the Bellingshausen Sea and WAP allowing CDW unhindered access to the continental shelf (e.g., Nakayama et al., 2018; Graham et al., 2016; Martinson et al., 2008; Smith et al., 1999). However, it remains unclear whether variations in location and intensity of the frontal jet are associated with variations in the regional wind patterns and whether the frontal jet influences the heat transported onto the Bellingshausen Sea continental shelf and towards the ice shelf cavities. At the western limit of the Bellingshausen Sea, there is evidence for a bottom intensified ASC above the slope (Zhang et al., 2016; Nakayama et al., 2018; Thompson et al., 2020). Thompson et al. (2020) identified an eastward current at the western limit of the Bellingshausen Sea (west of the Belgica Trough) located between a shallow westward flow of surface waters and a deeper westward flow that extends from 1500 m to the seafloor. This eastward current is associated with the shoreward extent of offshore CDW and is suggested to be the source of warm water entering the Belgica Trough (Thompson et al., 2020).

Wind fields in the West Antarctic sector are dominated by a low pressure system, the Amundsen Sea Low (ASL), centred in the Amundsen Sea (Hosking et al., 2013; Hosking et al., 2016). Many studies have suggested that variations in the CDW inflow to the Amundsen Sea are linked to the wind field above the continental shelf break (e.g., Kim et al., 2017; Steig et al., 2012; Thoma et al., 2008). Dinniman et al. (2012) demonstrated with a regional ocean-sea ice-ice shelf simulation that the inflow of CDW onto the WAP shelf is dependent on both wind strength and ACC transport. Due to the positioning of the ASL, eastward winds occur above the shelf break and slope that directly control the cross-slope heat flux through current fluctuations within both major troughs, the Getz-Dotson and the Pine Island-Thwaites Troughs (e.g., Wählin et al., 2013; Assmann et al., 2013; Thoma et al., 2008). Ekman pumping associated with the regional wind pattern is another possible mechanism to deliver warm waters onto the continental shelf (e.g., Kim et al., 2017; Kimura et al., 2017; Assmann et al., 2019). Similarly, Martinson et al. (2008) suggested wind-driven upwelling of offshore CDW as a possible mechanism for the delivery of CDW onto the WAP shelf. However, unlike the Amundsen Sea, the winds associated with the ASL in the Bellingshausen Sea tend to be onshore rather than along-shore, so this region experiences the weakest along-slope winds of the Antarctic

margins (Hazel and Stewart, 2019; Turner et al., 2013). Modelling studies and observations at the WAP indicate that when the mean shelf break flow encounters curving bathymetry, some of the water within the ACC is carried onto the shelf by momentum, if the forcing is strong enough (Dinniman and Klinck, 2004; Klinck et al., 2004). At the WAP eddy heat fluxes at the shelf break were also identified as a mechanism for on-shelf heat transport (Couto et al., 2017). Conditions that are favourable for mCDW to access the continental shelf and to reach the southern Bellingshausen Sea are still uncertain, largely due to the lack of long-term observations in this particularly inaccessible area.

Although much of the literature concerning interannual variability in heat content over the West Antarctic continental shelf has focused on shelf break processes, other studies have highlighted processes local to the shelf. St-Laurent et al. (2015) and Webber et al. (2017) emphasised the influence of local sea ice formation and air-sea heat fluxes on water temperatures over the Amundsen Sea continental shelf. Additionally, Kim et al. (2021) found much larger variability in mCDW properties in the Dotson Trough close to the coast, as compared to at the shelf break. Warm and cold regimes in the Amundsen Sea have been identified using observations (e.g., Jenkins et al., 2018; Webber et al., 2017) and models (e.g., Nakayama et al., 2018; Dutrieux et al., 2014; Dotto et al., 2019). However, the lack of long-term observations on the continental shelf of the Bellingshausen Sea means that interannual temperature variability there has not yet been studied.

In this study, we identify conditions and processes related to warm and cold regimes on the continental shelf of the Bellingshausen Sea, particularly within Eltanin and Latady bays near the southern coast using a high-resolution global ocean reanalysis. We have been unable to find a name in the literature for the large bay at the southern end of the Latady Trough (Fig. 3.1), and will therefore refer to it as Latady Bay. We test the hypothesis that changes of the ASL's location and intensity in the Bellingshausen Sea determine the ocean conditions on the continental shelf. We use the GLORYS12V1 reanalysis firstly to describe spatial and temporal variability of temperature, heat content and surface heat fluxes, secondly to identify conditions that represent warm and cold conditions in the Bellingshausen Sea, and thirdly to identify processes that are responsible for warming and cooling. The paper is organized as follows: section 2 introduces and describes the GLORYS12V1 reanalysis in the Bellingshausen Sea. Section 3 quantifies and discusses spatial and temporal variability. Section 4 presents warm and cold regimes using composites and anomalies with respect to the long-term mean, and discusses processes driving warming or cooling with

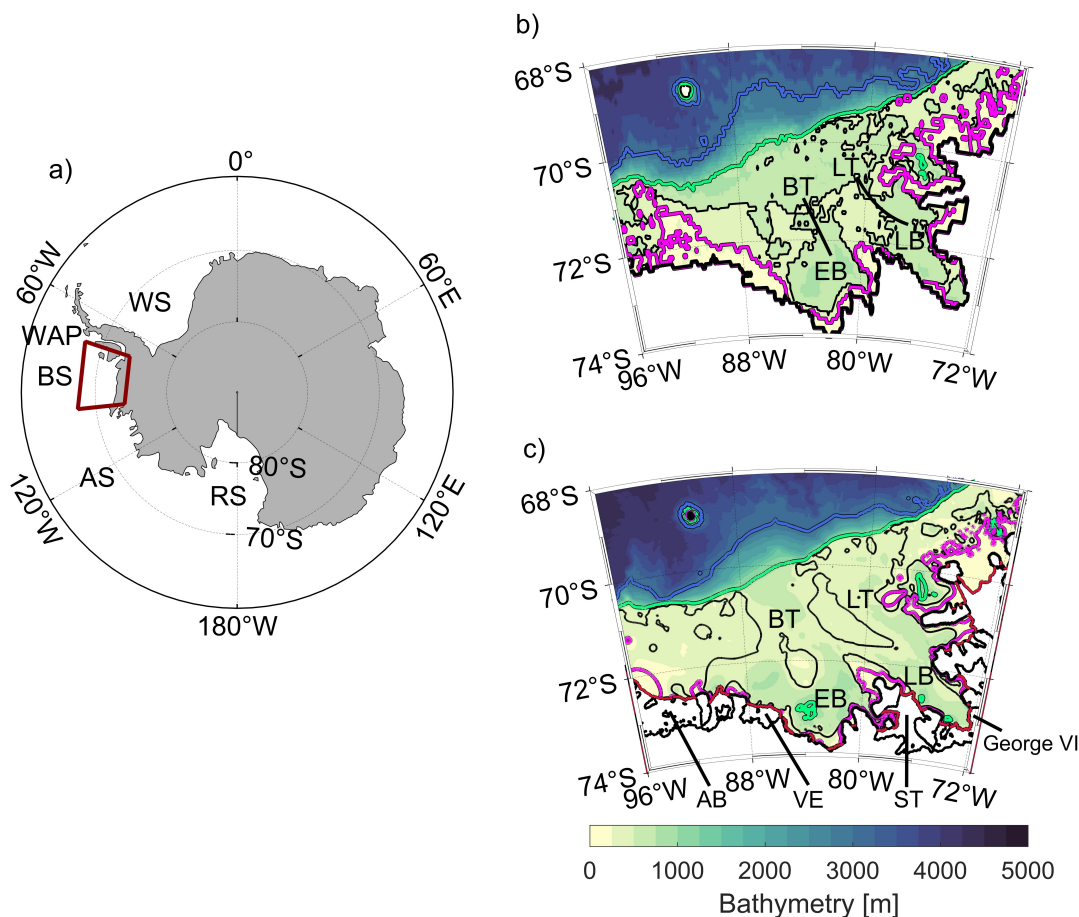


Figure 3.1: (a) Map of the Southern Ocean, with the study region outlined by a red box (b) bathymetry of the Bellingshausen Sea (red box in a)) extracted from GLORES (GEBCO8) with black lines indicating the Belgica and Latady trough locations, and (c) bathymetry of the Bellingshausen Sea extracted from the R-Topo2 data product (Schaffer et al., 2016). The coloured contours indicate the 3000 m isobath (blue), the 1000 m isobath (green), the 500 m isobath (grey) and the 300 m isobath (magenta) with the coastline (bold black). For the purposes of this study, the shelf break is defined as the 1000 m isobath. Ice shelves along the coast are indicated by red contours. Key geographic features in (a) and (b) are labelled: Bellingshausen Sea (BS), Amundsen Sea (AS), West Antarctic Peninsula (WAP), Ross Sea (RS), Weddell Sea (WS), Belgica Trough (BT), Latady Trough (LT), Eltanin Bay (EB), Latady Bay (LB), Abbot Ice Shelf (AB), Venable Ice Shelf (VE), Stange Ice Shelf (ST), Wilkins Ice Shelf (WI) and George VI Ice Shelf (George VI).

comparison to previous studies. Section 5 summarises the main conclusions and offers suggestions for future work.

3.2 The GLORYS12V1 Reanalysis and Climatology

The GLORYS12V1 reanalysis, hereinafter referred to as GLORYS, provided by the Copernicus Marine Environment Monitoring Service (CMEMS), is a global ocean product with a horizontal resolution of $\frac{1}{12}^\circ$ (~ 3 km in the Bellingshausen Sea) and 50 vertical z-levels covering the altimetry era from 1993 onward (DOI: 10.48670/moi-00021, 2021, (Fernandez and Lellouche, 2021)). All variables are provided on the same regular grid (Fernandez and Lellouche, 2021). Typically, most recent products are available with a 24-month delay. This study uses output up to December 2018. GLORYS assimilates sea level anomalies of all altimetric satellites, potential temperature and practical salinity profiles from the CMEMS CORAv4.1 database and sea ice concentration from the satellite data processing and distribution center of Ifremer (CERSAT database, <https://cersat.ifremer.fr/>). The implemented sea ice model is LIM2 and fully coupled to the ocean. Climatological river run-off based on (Dai et al., 2009) and freshwater fluxes from icebergs for Antarctica are implemented. The GLORYS ocean model component is the NEMO platform driven at the surface by ERA-Interim atmospheric forcing. In this study, we show wind fields extracted from the fifth generation of the European Center for Medium-Range Weather Forecasts (ECWMF) global climate reanalysis, ERA5 (Hersbach et al., 2019) that reflects the same patterns of variability as its predecessor ERA-Interim within the considered time period in the Bellingshausen Sea, but with much higher horizontal resolution (0.36° vs ERA-Interim 1°). The model bathymetry is based on ETOPO1 for the deep ocean and GEBCO8 for the coast and continental shelf (Fig. 3.1b) and does not include ice shelf cavities (discussed further below).

Regional models with higher resolution and a more detailed bathymetry, providing a more accurate representation of the major troughs than in GLORYS, have been used to simulate the Bellingshausen Sea area (Flexas et al., 2022; Nakayama et al., 2018; Graham et al., 2016). Moreover, katabatic winds driving the sea ice away from coastal regions (e.g., coastal polynya region) may occur in the southern Bellingshausen Sea. Due to the sporadic and short-lived occurrence of katabatic winds, they are not well captured in the monthly mean

and annual mean analysis provided in this study. Katabatic winds are thus not considered in detail. Nonetheless, using a global reanalysis such as GLORYS has the advantage that it captures the response to larger-scale temporal and atmospheric variability better than regional high-resolution models. Therefore, we find GLORYS best suited to investigate temporal and spatial variability as it assimilates all available data and provides a continuous time series of 26 years, longer than available for most regional models. Here, we use annual and monthly means of potential temperature, sea surface height (SSH), current velocities and sea ice concentration in combination with wind velocity and wind stress curl from 1993 to 2018 in the Bellingshausen Sea domain (Fig. 3.1). We take the means of these parameters over the whole time period from 1993 to 2018 as representative of the long-term mean state (Fig. 3.2).

The main focus of this study is the properties of mCDW ($\theta < 1.5^\circ\text{S}$), which is the water mass most likely to enter ice shelf cavities and contribute heat to the melting process (e.g., Jacobs et al., 2012; Kimura et al., 2017; Assmann et al., 2019). The average depth of the thermocline, the upper boundary of mCDW, over space and time on the Bellingshausen Sea continental shelf is approximately 300 m (Fig. 3.3). Spatially-averaged vertical profiles (Fig. 3.3) indicate variations of the thermocline depth from 270 m to 370 m associated with bottom temperature variations. Bottom temperature variations indicate two regimes, a cold regime and a warm regime. In the cold regime, the bottom temperatures of the average vertical profile (Fig. 3.3) are colder than average and the thermocline is shallower. Likewise, if the bottom temperatures of a vertical profile are warmer than average the thermocline is deeper. In order to capture the temperature variations in lower levels of the water column, we use vertically-averaged temperatures from 300 m to 1000 m (or to the seabed for shallower areas) for spatial and temporal analysis. Hereinafter all vertical averages imply 'below 300 m' unless stated otherwise.

The results are similar if the average is calculated using the water column below the temperature maximum, so the latter is not presented here. We also tested using the CDW layer thickness which has been demonstrated to be the main driver in heat content variability on the Amundsen Sea continental shelf (e.g., Thoma et al., 2008; Jenkins et al., 2018; Kim et al., 2021), but this approach gave similar results to the average temperature below 300 m, so is not presented here.

In general, GLORYS has small regional temperature biases (less than 0.4°C) in temperature with respect to the Worlds Ocean Atlas climatology 2013 and in-situ data (Drévilion et al., 2021). Drévilion et al. (2021) further stated that

the largest biases of up to 0.4°C may occur in the 50-100 m layer and in the northern Atlantic and Southern Ocean. In this study, our analysis is mainly focused on vertically-averaged temperatures below 300 m which minimizes the possibility of biases as much as possible.

The frontal jet (Fig. 3.2c,d), representing the ACC's Southern Boundary, occurs between the shelf break (1000 m isobath) and the 3000 m isobath. Its distance to the shelf break varies along the continental slope of the Bellingshausen Sea depending on the bathymetry. The frontal jet is closest to the shelf break in areas with a comparatively steep slope, such as between $90\text{-}92^{\circ}\text{W}$ and $72\text{-}81^{\circ}\text{W}$. In contrast, the frontal jet is located further away from the shelf break in areas with a relatively moderate slope, such as between $82\text{-}87^{\circ}\text{W}$. The frontal jet coincides with the 1.5°C isotherm, separating warmer off-shelf waters from colder waters further south, as shown by the long-term mean of vertically averaged potential temperature (Fig 3.2a)

Wind fields extracted from ERA5 (Fig. 3.4b,c) reveal a cyclonic rotation around a low pressure system, the ASL (Fig. 3.4a,b). The cyclonic rotation is also associated with a negative wind stress curl (Fig. 3.4d). Large negative values of the wind stress curl occur south of 72°S and indicate Ekman upwelling which results in an uplift of isopycnals in this region. The zero wind stress curl at $90\text{-}96^{\circ}\text{W}$ above the continental slope coincides with the lowest sea level pressure and weakest wind intensity in the Bellingshausen Sea area and suggests that the ASL is centred further to the west (Fig. 3.4a). Ekman transports modulated by wind direction and intensity are directed away from the central continental shelf, where a minimum in SSH supports the cyclonic gyre within $79\text{-}89^{\circ}\text{W}$ and $71\text{-}74^{\circ}\text{S}$ (Fig. 3.2b). Assmann et al. (2005), using coupled ice-ocean simulations, also found the region to be dominated by a cyclonic gyre with a similar longitudinal extent as in GLORYS. Moreover, recent studies observed individual cyclonic circulation features within the major troughs of the Bellingshausen Sea with inflow of mCDW along the eastern boundaries of the troughs up to the ice shelves (Schulze-Chretien et al., 2021; Zhang et al., 2016). The on-shelf transport appears to follow the 500 m contour in GLORYS, however the cyclonic circulation within individual troughs on the Bellingshausen Sea continental shelves is not indicated clearly as the trough pathways are not well represented. Note that the troughs represented in GLORYS are narrower than in the available bathymetric data products (e.g. R-Topo2, (Schaffer et al., 2016)). Regions in the GLORYS troughs that are shallower than the actual depth may act as a topographic barrier by constraining the southward

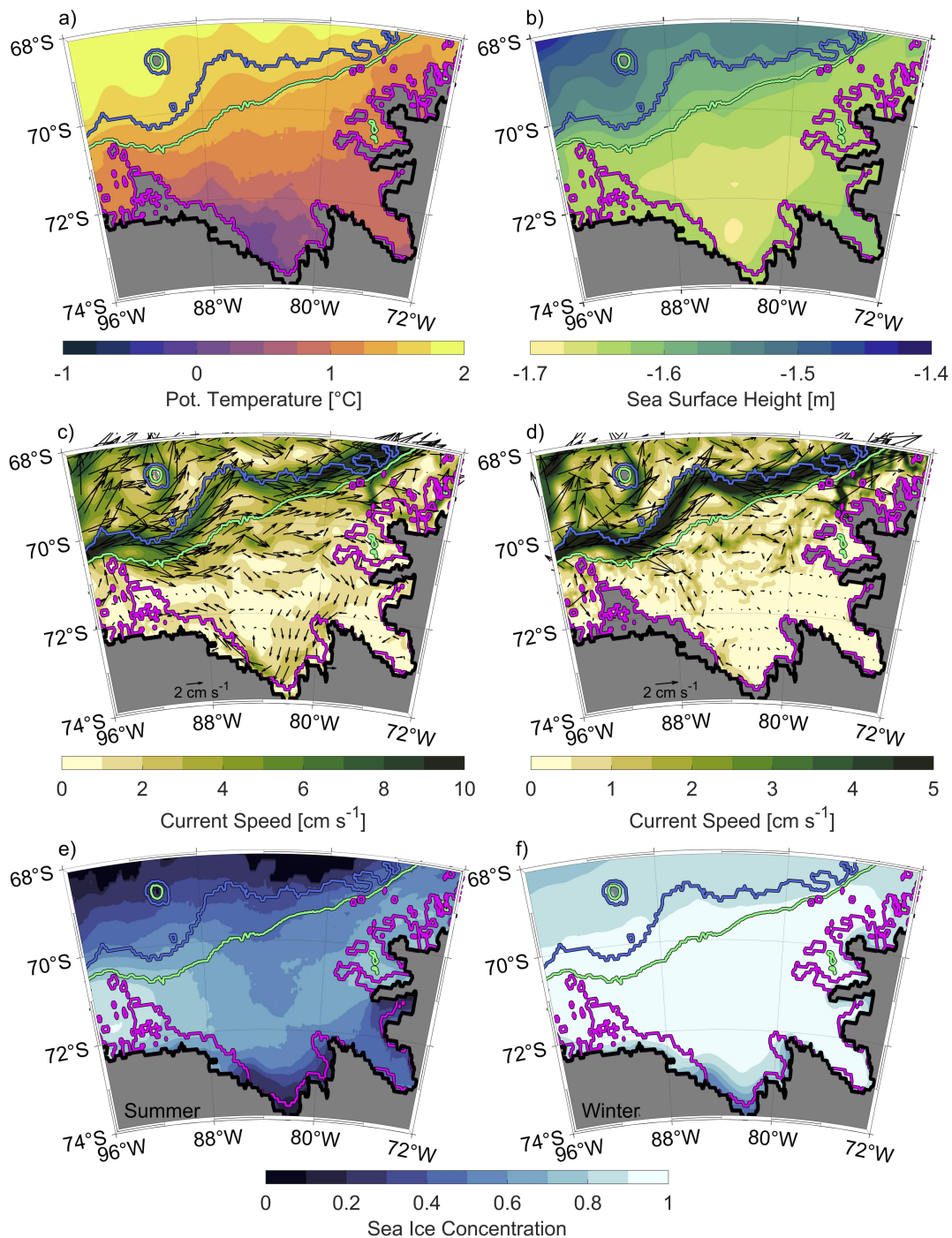


Figure 3.2: Long-term mean from 1993 to 2018 of (a) potential temperature below 300 m, (b) Sea Surface Height (SSH), (c) current speed above 300 m superimposed with velocity arrows, (d) current speed below 300 m superimposed with velocity arrows, (e) summer sea ice concentration and (f) winter sea ice concentration, all extracted from the GLORYS reanalysis. Note the different scales used in panels (c) and (d). Isobaths are shown with coloured contours as in Fig. 3.1 with the exception of the 500 m isobath.

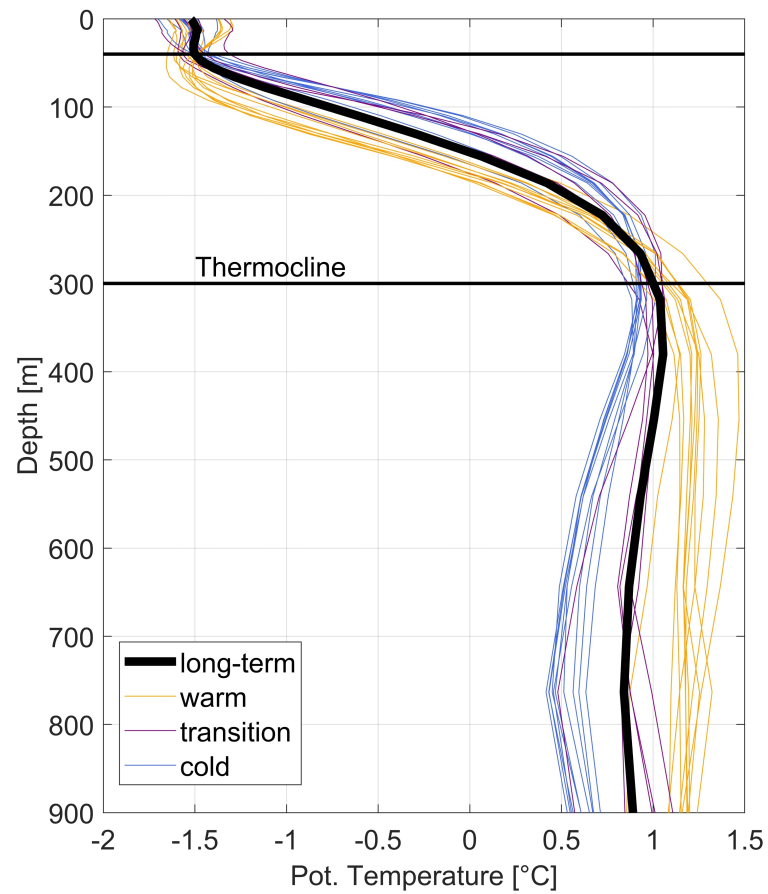


Figure 3.3: Vertical profiles of potential temperature averaged over all on-shelf grid points (i.e., points shallower than 1000 m). Annual average profiles for the warm years (1993-1995 and 2008-2015, orange lines), cold years (1997-2006, blue lines) and transition years (1996, 2007 and 2016-2018, purple lines). The warm, cold and transition years are defined as in section 3.3. The long-term mean vertical profile is shown as a thick black line. Horizontal black lines indicate top and bottom of the average thermocline with the bottom of the thermocline located at a depth of 300 m on average.

heat transport in lower layers associated with mCDW. The southernmost areas between 79-88°W influenced by the cyclonic wind circulation exhibit strong meridional SSH gradients (Fig. 3.2b) and reveal the Antarctic Coastal Current, which is most clearly identifiable in the vertically-averaged current speeds from the surface to 300 m (Fig. 3.2c). The Antarctic Coastal Current has also been identified in previous studies and reaches from the WAP through the Bellingshausen Sea into the Amundsen Sea (Assmann et al., 2005; Holland et al., 2010; Schubert et al., 2021).

Current speeds below 300 m (Fig. 3.2d) are much weaker on the Bellingshausen Sea shelf than in the frontal jet. Velocities below 300 m near the shelf break suggest an inflow of warmer waters onto the shelf at 70.5°S and 89-90°W. Once on the shelf, warm water masses flow roughly parallel to the shelf break, flooding the central and eastern shelf between 70-71°S until they recirculate with the frontal jet at 76°W. Warmer temperatures on the shelf north of 71°S (Fig. 3.2a) further indicate the inflow of warmer water ($> 1^\circ\text{C}$) suggesting access of CDW, or its modified variants, to the continental shelf. Summer sea ice concentrations (Fig. 3.2e) throughout the central and eastern Bellingshausen Sea shelf vary between 50-70%. Winter sea ice concentrations (Fig. 3.2f) are 100% throughout the Bellingshausen Sea continental shelf with the exception of the southern continental shelf between 79-87°W. Low sea ice concentrations in the southernmost region on the Bellingshausen Sea continental shelf indicate a coastal polynya near the Venable and Stange ice shelves. Strong north-westward winds south of 72°S (Fig. 3.2c) might facilitate the transport of sea ice towards the western Bellingshausen Sea shelf, where the highest concentrations, between 80-90%, are found (Fig. 3.2e) in summer. The long-term summer and winter sea ice concentrations are represented well in GLORYS and reflect key features and patterns similar to satellite observations of summer and winter sea ice concentrations demonstrated by Parkinson and Cavalieri (2012).

A significant limitation of GLORYS is the lack of ice-shelf cavities and thus a representation of water mass transformation as mCDW circulates within these cavities and becomes more buoyant due to the addition of glacial meltwater. This process plays an important role in the heat budget of the continental shelf (e.g. Couto et al., 2017), and its absence in these simulations may result in a positive bias (more ocean heat loss) in the surface heat loss discussed in section 4. It has also been proposed that the ice-shelf pump mechanisms contribute to setting the overturning magnitude in the Bellingshausen Sea (Thompson et al., 2020; Ruan et al., 2021) although the trough circulations that deliver warm water to the ice shelf cavities are largely barotropic features (Wählin et al.,

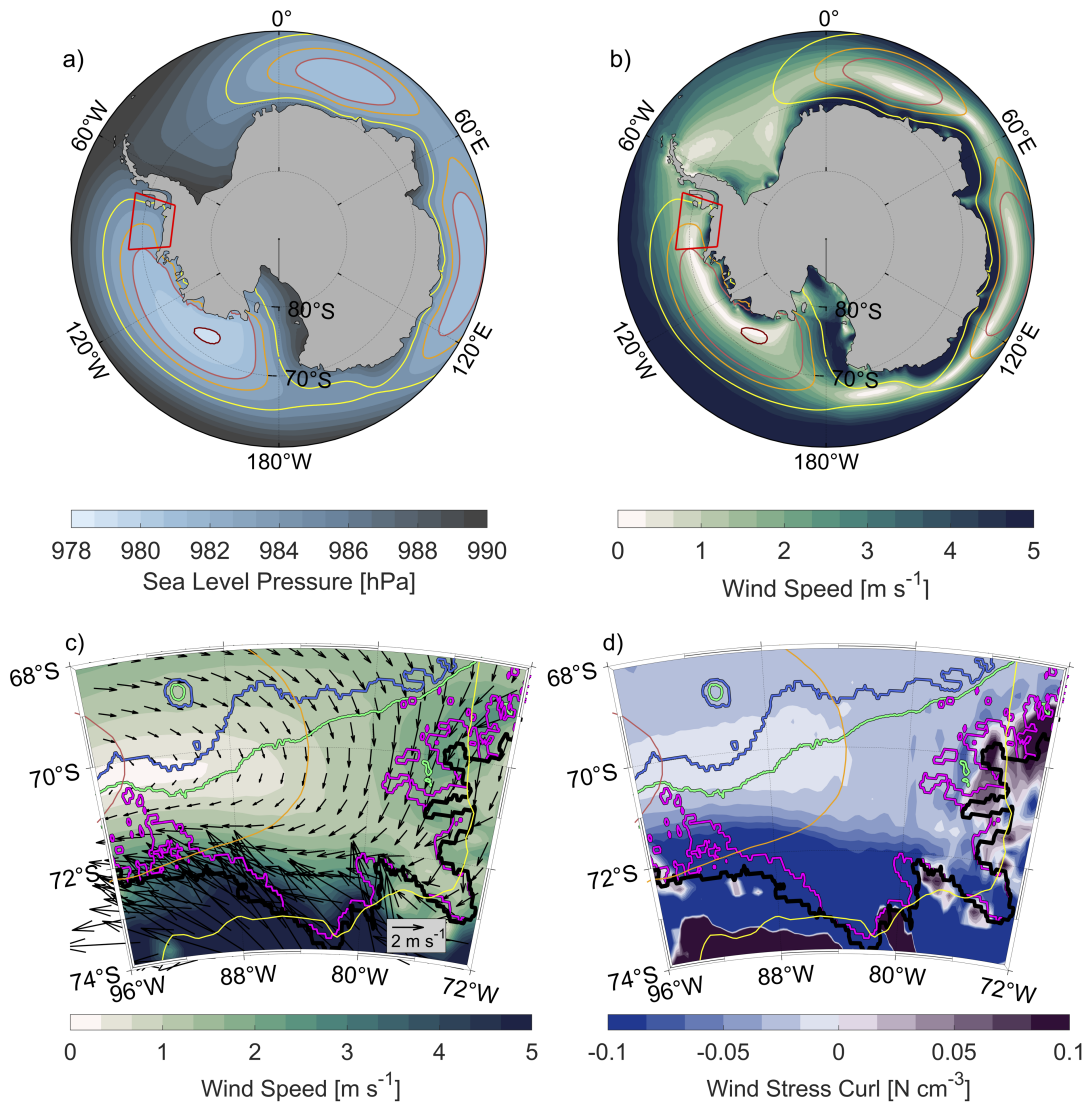


Figure 3.4: Long term mean from 1993 to 2018, extracted from ERA5, of (a) sea level pressure and (b) wind speed around Antarctica, (c) wind speed superimposed with arrows of wind velocity and (d) wind stress curl in the Bellingshausen Sea region. In all panels, the coastline of Antarctica is shown as a black contour, and sea level pressure contours are shown as thin green (980 hPa), red (982 hPa), orange (983 hPa) and yellow (985 hPa) lines. The low pressure region between 70-180°W is known as the Amundsen Sea Low. For (c) and (d) isobaths are shown as in Fig. 3.2.

2020), which should be adequately captured, to the extent that is possible with the model's bathymetry.

In summary, while the circulation on the shelf does not exactly match the observations, due to limitations in the model bathymetry and lack of ice shelf representation, we do find access of warmer water onto the Bellingshausen Sea continental shelf in the reanalysis long term mean. In the following section, we investigate the dominant patterns of spatial and temporal variability in water temperature below 300 m on the continental shelf.

3.3 Modes of Variability of Ocean Temperature on the Continental Shelf

For our analysis Empirical Orthogonal Functions (EOF) are calculated from the vertically-averaged potential temperatures below 300 m. Waters at these depths are most likely to enter ice shelf cavities and contribute to the melting process. To ensure that only deep water masses on the continental shelf, such as mCDW are considered, areas shallower than 300 m and deeper than 1000 m are excluded from the calculation. In order to focus on interannual variability and to avoid seasonal effects in our study, we calculate EOFs from annual means.

This study focuses on the 1st EOF mode (Fig. 3.5a), which describes the pattern of the most dominant mode of variability and explains 65% of the variance. Further modes explain less than 20% each and are not considered further. Large values (positive or negative) imply that a grid point has a large amplitude of temporal variability associated with this spatial pattern. The 1st EOF mode presents a weak amplitude of temporal variability at the shelf break throughout the central and eastern Bellingshausen Sea. This is because the temperature of the water below 300 m near the shelf break does not vary as much as that further south in Latady and Eltanin Bay (Fig. 3.6a,b). South of 71°S EOF values increase towards coastal regions, where EOF maxima are predominantly found within Eltanin and Latady bays near the coast. The western edge of the Bellingshausen Sea (west of 91 °W) presents an EOF temperature variability that is out of phase compared with other parts of the shelf. This is likely due to the relatively shallow region between 90-92°W, that may be considered the boundary between the Bellingshausen Sea and the Amundsen Sea, and thus between two different dynamical regimes.

The EOF timeseries (Fig. 3.5b), hereinafter called principal component (PC), describes the weighted amplitude representing the spatial variability of

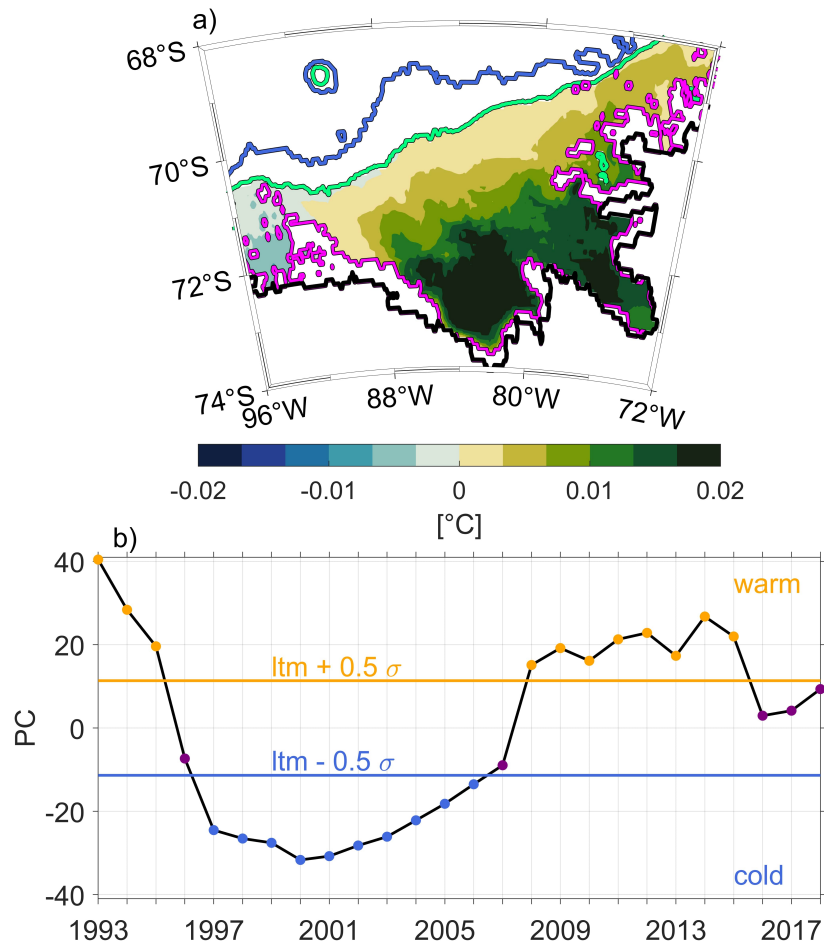


Figure 3.5: (a) 1st EOF mode for potential temperature below 300 m on the Bellinghousen Sea continental shelf. The EOF has been calculated from 1993 to 2018 annual means, where areas deeper than 1000 m and shallower than 300 m have been excluded. Isobaths are coloured as in Fig. 3.2. (b) PC (unitless) of the 1st EOF mode. Horizontal lines represent upper and lower boundaries for warm (orange) and cold (blue) years which are calculated as $l_{tm} \pm 0.5\sigma$, where l_{tm} is the long term mean and σ the standard deviation of the PC.

temperature below 300 m and highlights the two main regimes (warm and cold). Using a weighted amplitude of variability is important for the purpose of defining warm and cold regimes, as the temperatures below 300 m in the Bellingshausen Sea do not vary uniformly for all areas of the continental shelf (Fig. 3.5a). Years in which the $PC > ltm + 0.5 \sigma$, where σ is the standard deviation of the PC and ltm is the long-term mean, are considered warm years (11 years in total, 1993-1995 and 2008-2015). Similarly, years in which the $PC < ltm - 0.5 \sigma$ are considered to be cold years (10 years in total, 1997-2006). The years 1993 and 2000 are the warmest and coldest years of the period, respectively. The remaining years that do not qualify as either warm or cold will be referred to as transition years. Periods of pronounced warm and cold years mostly agree with those identified by Nakayama et al. (2018), who described simulated colder and warmer mCDW in the years from 2001-2006 and 2009-2014 using a regional configuration of the Massachusetts Institute of Technology general circulation model (MITgcm) for the Amundsen Sea and Bellingshausen Sea region. There exist slight differences in the timing of warm and cold years in GLORYS and the work of Nakayama et al. (2018). A possible explanation for these differences is that the ECCO-v4 surface forcing was used in the MITgcm simulation, which is based on ERA-Interim but differs slightly (Nakayama et al., 2017). The separation of warm and cold years in the neighbouring Amundsen Sea near the Dotson ice shelf by Jenkins et al. (2018) only partly agrees with our determinations of warm and cold periods in the Bellingshausen Sea. Oceanic regime transitions derived from hydrographic observations discussed by Jenkins et al. (2018) indicated a cold period from 2000-2003, warm period between 2004-2011, and a further cold period from 2012 to 2016, where 2009 was the peak warm phase and 2006-2007 intermediate years. A clear difference between the Bellingshausen and Amundsen seas with respect to warm and cold regimes occurs during the most recent cold period from 2012 to 2016 in the Amundsen Sea. The Amundsen Sea cold period has been described extensively in previous studies using observations (Jenkins et al., 2018; Webber et al., 2017) and simulations (Dutrieux et al., 2014; Dotto et al., 2019). Dutrieux et al. (2014) and Webber et al. (2017) demonstrated that ocean conditions are partly attributable to atmospheric forcing and sea ice formation in the Amundsen Sea. In contrast, the Bellingshausen Sea EOF mode suggests 2012 to 2015 to be warm years and 2016 to 2018 to be transition years. This suggests that water temperatures in the Amundsen and Bellingshausen seas are not always in phase and may be controlled by different processes. The findings agree with the out of phase EOF temperature variability at the western edge of the Bellingshausen Sea (west of

91 °W, transition to the Amundsen Sea, Fig. 3.5a).

We use a PC-based definition of warm and cold years to calculate warm and cold composites (PC-weighted mean of all warm and all cold years) and anomalies (composite minus the long-term mean fields described in section 3.2). The anomalies (Fig. 3.6a,b) present anomalously warm and cold temperatures below 300 m consistent with the variability pattern provided by the 1st EOF mode and are, as expected, correlated to its PC (not shown). Generally, the spatial distribution indicates that on-shelf temperatures south of 71°S are increasingly warm from the shelf break towards the coast for the warm regime and increasingly cold towards the coast for the cold regime, as expected from the EOF map where the 1st EOF mode increases towards the coast (Fig. 3.5a). Maximum temperature anomalies of more than 0.5°C are found within Eltanin and Latady bays in the south of the Bellingshausen Sea continental shelf.

To explore the presence of mCDW and the difference in water mass stratification on the Bellingshausen Sea continental shelf for warm and cold regimes, we select a vertical profile at a location (83°W and 72.5°S, Fig. 3.6, yellow dots) characterised by the strongest anomalies in temperature below 300 m within Eltanin Bay (Fig. 3.7). Below the relatively fresh surface mixed layer near the freezing point, identified as Antarctic Surface Water, the cold regime has a temperature maximum of 0.5°C at a depth of about 250-300 m. This temperature maximum is colder than that of the warm regime, suggesting more modification of CDW in the cold regime. Water masses below the thermocline cool to about -0.7°C and slightly freshen towards the seabed. In contrast, the warm regime presents a slightly warmer surface mixed layer and a warmer temperature maximum up to almost 1°C, coinciding with increased salinity of up to 34.84. This water mass, identified as weakly modified CDW (mCDW), extends throughout the remaining water column down to the sea bed. These findings show the increased presence of mCDW in Eltanin Bay in the warm regime, with temperatures almost 2°C greater than in the cold regime.

To identify the vertical and spatial extent of mCDW, we show a meridional transect crossing the shelf break and a zonal transect crossing the continental shelf. The meridional and zonal transects intersect at 72°S as shown in Fig. 6 (white dashed lines). Note that the zonal transect is terminated by land at the eastern end, and by very shallow water (< 30 m) at the western end. The meridional and zonal transects (Figs. 3.8 and 3.9) demonstrate that the lower water column is occupied by a colder and fresher water mass south of 71.3 °S in the cold regime, whereas the lower water column in the warm regime is dominated by mCDW. We define two isopycnals (27.6 kg m^{-3} and 27.8 kg m^{-3} , potential

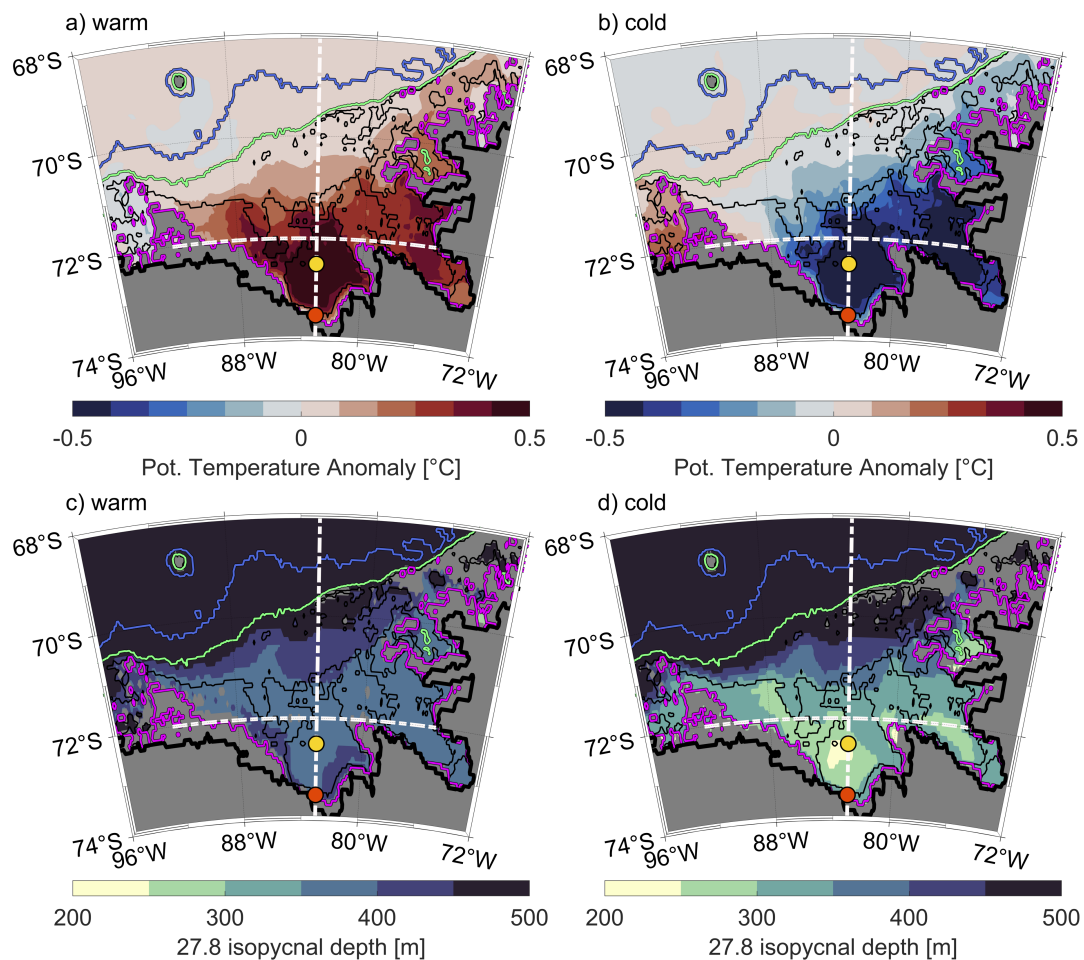


Figure 3.6: (a,b) Anomalies of vertically-averaged potential temperature from 300 m to the bottom of the shelf, where positive anomalies (red) imply higher temperatures, and (c,d) composites of the 27.8 kg m⁻³ isopycnal depth, for the warm (a,c) and cold (b,d) regimes. Yellow and orange dots mark the locations where temperature and salinity profiles are taken to describe the vertical structure of water masses (Figs. 3.7 and 3.14 respectively). White dashed lines show the meridional and zonal transect locations (shown in Figs. 3.8 and 3.9). Isobaths are colored as in Fig. 3.2.

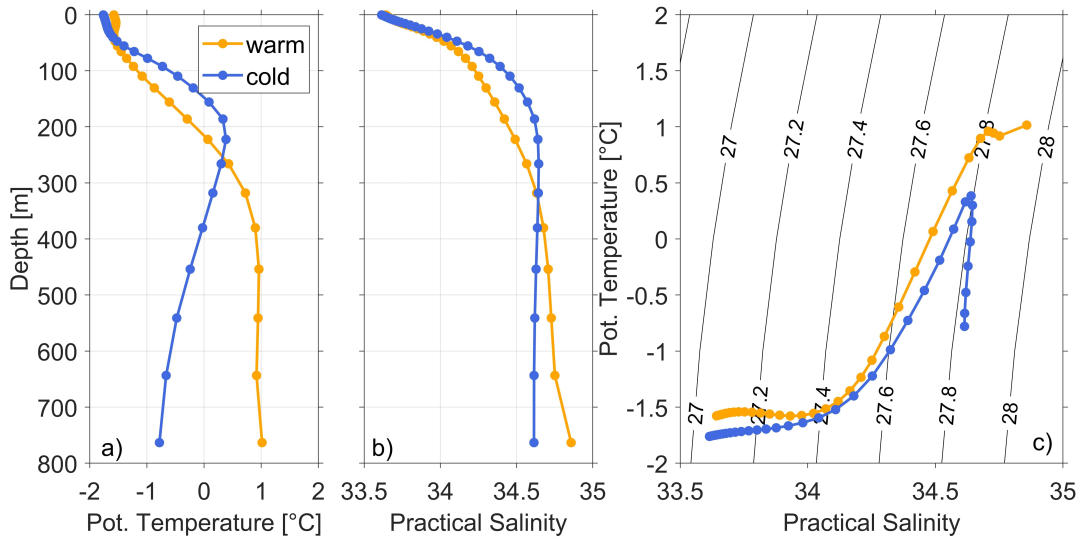


Figure 3.7: Vertical profiles of (a) potential temperature and (b) practical salinity along with (c) θ -S diagrams for the warm (orange) and cold (blue) composites with contours of potential density. The profiles are taken from 72.5°S and 83°W (Fig. 3.6, yellow dots), a location with high inter-annual variability in the temperature below 300 m.

density) to identify upper and lower boundaries for mCDW on the continental shelf. The 27.6 kg m⁻³ and 27.8 kg m⁻³ isopycnals at the shelf break are in a similar depth in the cold and the warm regimes (Fig. 3.8), which suggests that neither the warm nor the cold regime would allow greater access of CDW, or mCDW, onto the continental shelf in the meridional transect. Composites of the 27.8 kg m⁻³ isopycnal depth (Fig. 3.6c,d) confirm the same isopycnal depth above shelf break and continental slope for both regimes. Both isopycnals are shallower in the central and southern Bellingshausen Sea in the cold regime (Figs. 3.8b,d and 3.9b,d) than in the warm regime (Figs. 3.8a,c and 3.9a,c). Specifically the 27.8 kg m⁻³ isopycnal in the cold regime indicates that mCDW does not occupy deeper layers of the water column within Eltanin Bay (Fig. 3.8b,d). Composites of the 27.8 kg m⁻³ isopycnal depths (Fig. 3.6c,d), confirm the stronger uplift of this isopycnal in the cold regime, predominantly within Eltanin and Latady bays and near coastal regions. A possible explanation for the shallower isopycnals in the central and southern Bellingshausen Sea in the cold regime is the heaving of isopycnals in response to changes in SSH. The SSH levels for both regimes are discussed in section 4 in more detail.

In order to establish whether water mass properties found in GLORYS are representative of conditions in the Bellingshausen and Amundsen seas, we compare the model output with existing hydrographic observations from these shelf seas. Previously observed hydrographic transects crossing the Belgica and Latady troughs in 2007 and 2018/19 (Ruan et al., 2021; Schulze-Chretien et

al., 2021) show similar characteristics to GLORYS for the zonal transect in the warm regime (Fig. 3.9a), where mCDW occupies the lower layers of the water column from 300 m to the seabed with similar water mass properties and maximum temperatures of up to 1.6 °C. Jenkins et al. (2018), on the other hand, observed the water mass stratification in a cold year near Dotson ice shelf in the Amundsen Sea, which indicated that mCDW is only present in lower layers of the water column reaching from 700 to almost 1000 m. These findings are substantially different to the water mass stratification of cold years presented by GLORYS in the Bellingshausen Sea, where both transects (meridional and zonal) show mCDW higher up in the water column with uplifted 27.6 kg m^{-3} and 27.8 kg m^{-3} isopycnals in the southern and central Bellingshausen Sea in the cold regime. The zonal transect from GLORYS of the warm regime (Fig. 3.9a) shows a similar water mass stratification in the south of the Bellingshausen Sea as compared to the observed water mass stratification of Jenkins et al. (2018) in a warm year. The meridional and zonal transects of the warm regime demonstrate the presence of mCDW on the Bellingshausen Sea continental shelf including in Eltanin and Latady bays, and in close proximity to the coastline and thus theoretically close to the ice shelf cavities.

We have shown that the water mass stratification differs significantly between the warm and the cold regimes in GLORYS on the southern Bellingshausen Sea continental shelf. Meridional and zonal transects and vertical profiles indicate that differences mainly occur in the lower layers of the water column and are related to the presence of mCDW in Eltanin and Latady bays.

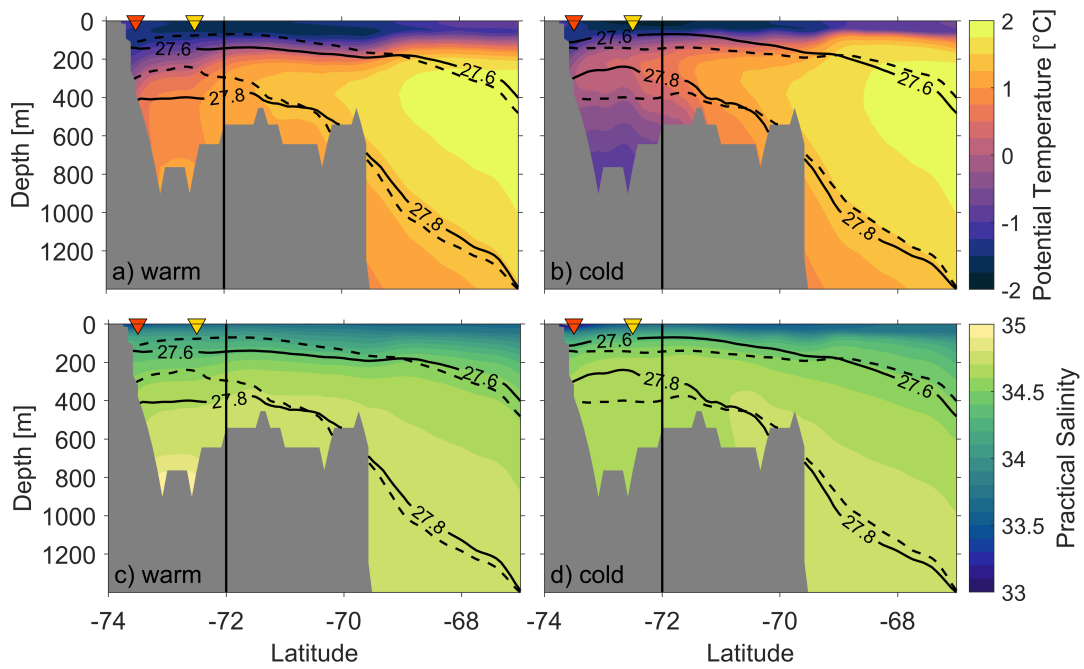


Figure 3.8: Composites of the meridional transect covering 67-74°S at 83°W (as displayed in Fig. 3.6, white dashed lines) from GLORYS with (a,b) potential temperature and (c,d) practical salinity for the warm (a,c) and cold (b,d) regimes. Solid black lines on all panels are potential density for the warm (a,c) and cold (b,d) composites, whereas dashed black lines show the potential density of the opposite regime to highlight the differences between warm and cold regimes. The triangles indicate the locations of vertical profiles at 73.5°S (orange) and 72.5°S (yellow) as marked in Fig. 3.6. The shaded areas (gray) display the Bellingshausen Sea shelf bathymetry of the meridional transect crossing the shelf break. The vertical black line shows the location at 83°W, 72°S, where the meridional and zonal transects intersect.

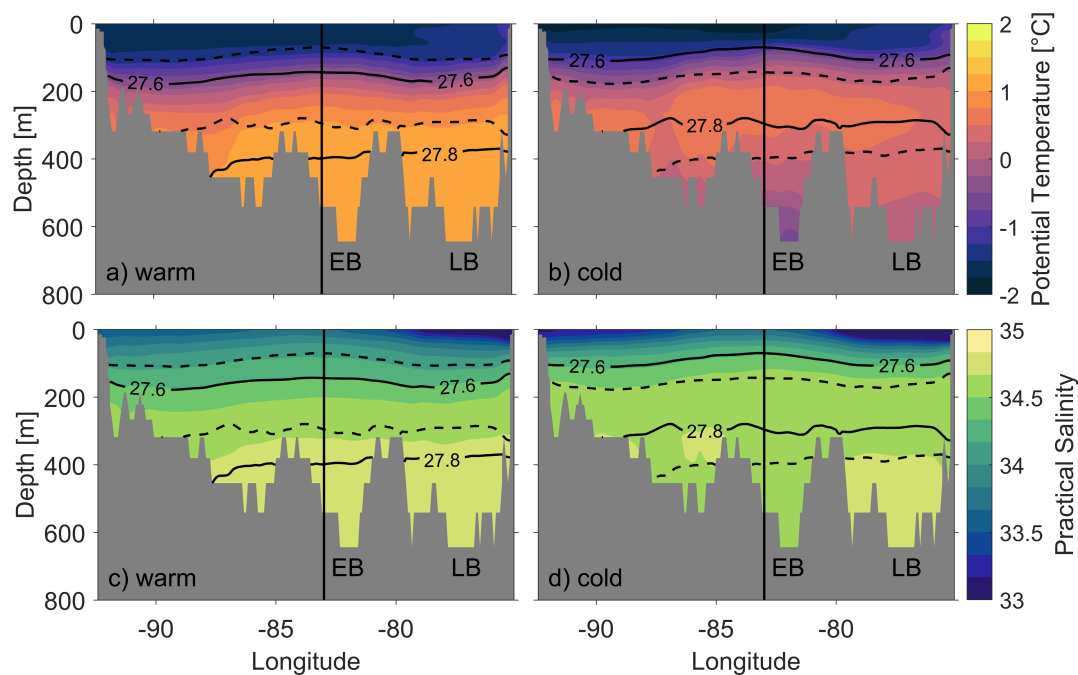


Figure 3.9: Composites of the zonal transect covering 75-92.5°W at 72°S (as displayed in Fig. 3.6, white dashed lines) from GLORYS with (a,b) potential temperature and (c,d) practical salinity of the warm (a,c) and cold (b,d) regimes. Solid black lines on all panels are potential density for the warm (a,c) and cold (b,d) composites, whereas dashed black lines show the potential density of the opposite regime to highlight the differences between warm and cold regimes. The shaded areas (gray) display the Bellingshausen Sea shelf bathymetry of the zonal transect crossing the Bellingshausen Sea continental shelf. The acronyms EB and LB mark the locations of Eltanin and Latady bays in the zonal transect. The vertical black line shows the location at 83°W, 72°S, where the meridional and zonal transects intersect.

3.4 Mechanisms Leading to Warm and Cold Regimes on the Continental Shelf

We now seek to determine whether net meridional heat transport Q_{hf} or net air-sea flux Q_{surf} , dominate the temporal change in heat content $\frac{d\bar{H}}{dt}$ south of 72°S.

The monthly-mean heat content for the volume south of 72°S is defined as:

$$\bar{H} = \int_{x_e}^{x_w} \int_{y_s}^{y_n} \int_{-h}^0 \rho c_p (\bar{\theta} - \theta_{ref}) dx dy dz, \quad (3.1)$$

where $\bar{\quad}$ indicates the monthly average, ρ is the potential density, $c_p = 3982 \text{ J (kgK)}^{-1}$ is the specific heat capacity, and θ is the potential temperature. $\theta_{ref} = -1.8^\circ\text{C}$ is a reference temperature, which for simplicity we take as the coldest temperature recorded in GLORYS in this domain, x is the zonal distance where x_w and x_e define the zonal limits, y is the meridional distance with y_s (latitude of the coast) and $y_n(72^\circ\text{S})$ defining the meridional limits, z is height and h the local sea bed depth of GLORYS.

We calculate the monthly-mean meridional heat flux \bar{F}_h through each grid cell of the zonal transect at 72°S as:

$$\bar{F}_h = \rho c_p \bar{v} (\bar{\theta} - \theta_{ref}), \quad (3.2)$$

where \bar{v} is the meridional velocity component normal to the transect, positive northwards. Note that when the data were analysed only annual and monthly means from GLORYS were available on the CMEMS platform for the time period considered in this study. Therefore, the eddy heat flux and diffusive heat flux have not been considered in detail. Then the monthly-mean net heat transport \bar{Q}_{hf} through the zonal transect (as indicated in Fig. 3.6, white dashed lines) is given by:

$$\bar{Q}_{hf} = \int_{x_w}^{x_e} \int_{-h}^0 \bar{F}_h dx dz. \quad (3.3)$$

Note that the net volume transport through the entire zonal transect is near zero on average ($\approx 0.02 \pm 0.02 \text{ Sv}$) and thus inflow equals outflow as the net evaporation minus precipitation, ice melt and river run-off are negligible in this region in GLORYS.

The air-sea-ice flux \bar{Q}_{surf} within the area south of 72°S is not provided by the reanalysis output but is deduced as the difference between the two terms above:

$$\bar{Q}_{surf} = \frac{d\bar{H}}{dt} - \bar{Q}_{hf}, \quad (3.4)$$

where $\frac{d\overline{H}}{dt}$ is the change in heat content over the monthly time interval. Note that the air-sea flux $\overline{Q_{surf}}$ includes processes involved with sea ice formation and melt as well as the air-sea heat fluxes. The annual-mean net volume heat content, heat transport and heat flux for a given year are then:

$$\langle \frac{dH}{dt}, Q_{hf}, Q_{surf} \rangle = \frac{\sum \frac{d\overline{H}}{dt}, \overline{Q_{hf}}, \overline{Q_{surf}}}{12}, \quad (3.5)$$

where $\langle \cdot \rangle$ indicates the average of the monthly-means within a given year.

The timeseries of $\frac{dH}{dt}$, Q_{hf} and Q_{surf} from 1993-2018 are shown in Fig. 3.10. The basic ocean heat budget illustrates the variability of $\langle \frac{dH}{dt} \rangle$ south of 72°S associated with the variability of $\langle Q_{hf} \rangle$ (crossing 72°S) and $\langle Q_{surf} \rangle$ and further highlights the differences in the heat budget components for warm and cold years. The monthly-means illustrate the seasonal variations, with positive $\frac{d\overline{H}}{dt}$ and $\overline{Q_{surf}}$ (surface heat uptake) during summer and negative $\frac{d\overline{H}}{dt}$ and $\overline{Q_{surf}}$ (surface heat loss) during winter (Fig. 3.10).

In the following we assess annual means to determine which of the above mentioned processes are dominant in the warm and cold regimes. $\langle \frac{dH}{dt} \rangle$ is negative during the warm regime from 1993 to 1996, also shown by the PC (Fig. 3.5b). This decrease in heat content is driven by a net northward $\langle Q_{hf} \rangle$ and negative $\langle Q_{surf} \rangle$ during those years until the cold regime begins in 1997.

After entering the cold regime, $\langle \frac{dH}{dt} \rangle$ is slightly positive and remains almost constant until 2008. The gradual increase in temperature over time is driven by a net southward $\langle Q_{hf} \rangle$ and a slightly positive $\langle Q_{surf} \rangle$ (ocean heat uptake). This gradual warming over time results in a transition to the second warm regime in 2008.

During the warm regime (2008 to 2015), $\langle \frac{dH}{dt} \rangle$ is more variable, also seen in higher variability of monthly means of heat budget variables. During the second warm regime, $\langle Q_{hf} \rangle$ is northward apart from in 2010 and 2011. $\langle Q_{surf} \rangle$ vary significantly during this period. A positive $\langle Q_{surf} \rangle$ in 2014 results in a short-term increase in $\langle \frac{dH}{dt} \rangle$ even though $\langle Q_{hf} \rangle$ is northward. In 2015 $\langle Q_{surf} \rangle$ is negative, due to increased heat loss in winter and weaker heat uptake in summer. Thus, the change in heat content arises as a residual between a large values of heat uptake in the summer and heat loss in the winter.

Overall, we find that water masses within Latady and Eltanin Bays experience warming (increasing heat content over time) during the cold regime and cooling (decreasing heat content over time) during the warm regime. The heat budget for the southern Bellingshausen Sea suggests that air-sea fluxes dominate over lateral ocean heat transport, at least in the GLORYS. Note that

the heat budget may be impacted by the lack of ice shelf cavities in GLORYS. Nonetheless, this finding is surprising as the southward heat transport associated with CDW and mCDW is often thought to be the main driver of enhanced ice shelf melt on the west Antarctic continental shelves.

We have shown that warm and weakly modified CDW can reach Eltanin and Latady bays on the Bellingshausen Sea continental shelf in GLORYS. Furthermore, we have demonstrated that a net southward heat transport and warming of the shelf occur primarily in cold years, which indicates a warming process within the cold regime. Conversely, the warm regime experiences a cooling of the waters in Eltanin and Latady bays. Therefore, we now seek to understand which dynamical processes and mechanisms are involved in controlling the change in heat content south of 72°S of subsurface waters within Eltanin and Latady bays.

In section 3.1 we hypothesized that the inflow of CDW into Eltanin and Latady bays is associated with changes in the strength and/or an intensification of the ASL. The long-term mean of sea level pressure shows that the ASL extends into the Bellingshausen Sea (Fig. 3.4). Composites of the sea level pressure for the warm and cold regimes (Fig. 3.11a,b) indicate a change in both the ASL's intensity and its eastern extent into the Bellingshausen Sea. The results show that in the cold regime the ASL is weaker and does not extend as far east into the Bellingshausen Sea compared with the warm regime, where the ASL is stronger and extends further east into the Bellingshausen Sea.

To understand the changes in atmospheric circulation between the warm and the cold regime, we consider the zonal and meridional wind components separately. Along with meridional and zonal wind vectors we consider the magnitude of wind speeds from both components compared with the long-term mean (Fig. 3.12). Note that positive anomalies are directed eastward for zonal winds and so represent either an increase in eastward or a decrease in westward wind speed. Similarly, positive anomalies for the meridional component are directed northward and so represent an increased northward wind speed or decreased southward wind speed.

For the purposes of the following discussion, we divide the study region into three boxes, as shown on Fig. 3.12. Box A covers the area offshore, and over the continental slope and shelf break, where Ekman transport away from the continental shelf occurs. Box B covers the area of the study region which is bounded by land to the east. Box C covers the southernmost areas, including Eltanin Bay and the coastal polynya mentioned in section 3.2. Since, the Eltanin and Latady bays show a similar overall pattern of temperature

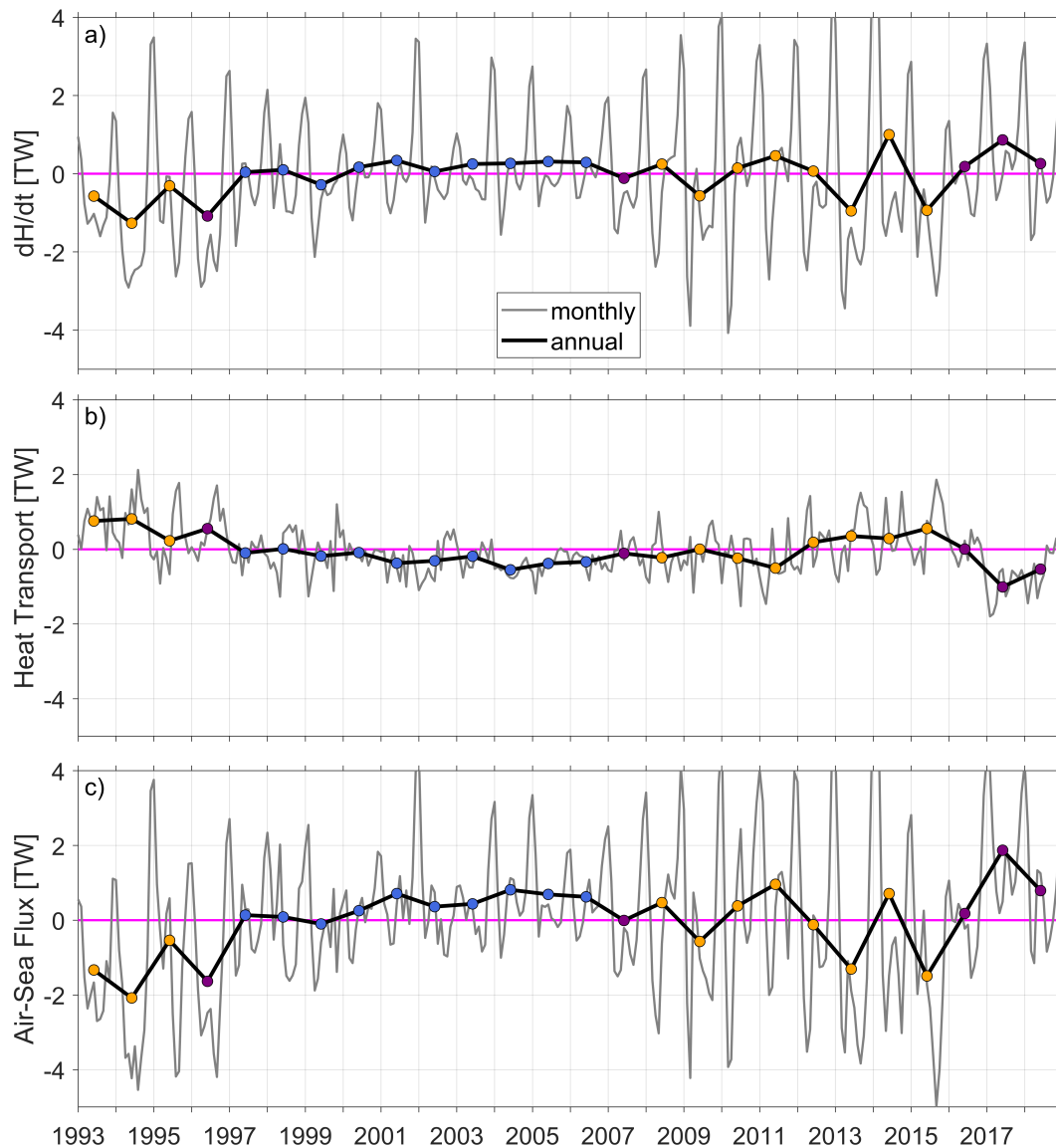


Figure 3.10: Monthly (grey lines) and annual means (black lines) of the net (a) temporal heat content change $\frac{dH}{dt}$, (b) heat transport Q_{hf} through the zonal transect at 72°S (positive northwards) and (c) air-sea flux Q_{surf} (positive air to sea) for the area south of 72°S in the southern Bellingshausen Sea (see equations (1)-(5) in section 3.4 for further details). Note that the air-sea flux Q_{surf} includes processes involving sea ice formation and melt and that annual mean values are positioned in the centre of the averaged year. Coloured dots represent cold (blue), transition (purple) and warm (orange) years (as in Fig. 3.5e). The zero line is highlighted in magenta.

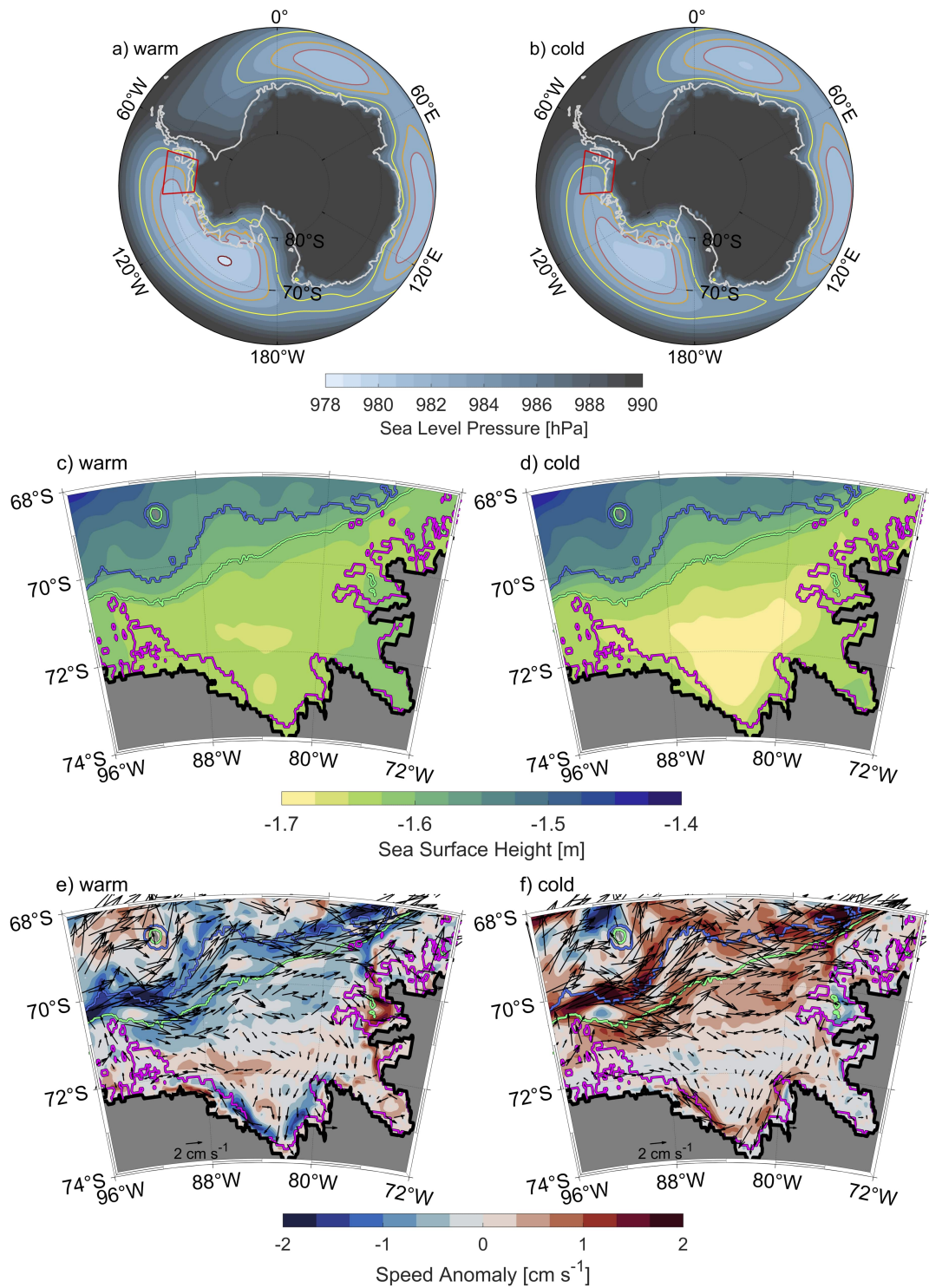


Figure 3.11: Composites of (a,b) sea level pressure and (c,d) SSH for the warm (a,c) and cold (b,d) regimes. (e,f) Anomalies of current speeds averaged from the surface to 300 m with superimposed current velocities from composites of the warm (e) and cold (f) regimes. The red box (a,b) highlights the Bellingshausen Sea region and sea level pressure contours and isobaths are coloured as in Fig. 3.4. Positive anomalies (e and f, red) imply higher current speeds.

variability (Fig. 3.5a), Latady Bay is not included in Box C. We confine our analysis to Eltanin Bay and the coastal polynya region, which are representative of the wider southern Bellingshausen Sea shelf.

Box A, which covers the shelf break region, shows a time-mean wind direction to the south-east and is investigated to discuss the Ekman transport away from the Bellingshausen Sea continental shelf in the warm and cold regimes. The wind direction and intensity show significant seasonality in box A (Fig. A1). In summer, the ASL is located further east and further north, leading to westward winds in box A (Fig. A2). In winter, the ASL is located further west and further south, leading to eastward winds in box A (Fig. A3). The long-term mean winds are similar to the winter winds indicating that the wind patterns displayed for winter are representative of much of the year, so anomalies in wind for the cold and warm regimes shown for winter will dominate over those for summer. In winter (and in the long-term mean), the cold regime is characterised by greater wind speeds, with an increase in both eastward and southward wind components (Figs. A3b,d,f and 3.12b,d,f). This means that the Ekman transport away from the continental shelf increases and leads to lower SSH on the shelf (Fig. 3.11d). The summer wind speeds show an increase in westward and northward winds (in the west of box A) and southward winds (in the east of box A) in the cold regime compared with the summer long-term mean (Fig. A2b,d,f). This will increase Ekman transport onto the continental shelf in the summer, but as noted previously this will be a smaller effect than the increased Ekman transport off the continental shelf in the rest of the year. The net effect over the whole year will be to increase SSH gradients over the continental slope, consistent with greater current speeds seen in the frontal jet (Fig. 3.11f). In the warm regime, wind speeds in winter (and in the long-term mean) and both the eastward and southward wind components (Figs. A3a,c,e and 3.12a,c,e) weaken, so the Ekman transport (while still directed away from the shelf) reduces. Resulting SSH gradients over the continental slope (Fig. 3.11c) reduce, consistent with lower speeds in the frontal jet (Fig. 3.11e). The proximity of the frontal jet to the shelf break (Fig. 3.11e,f) can be seen as an indicator for the proximity of CDW to the shelf break. Our results do not indicate a change in the proximity of the frontal jet to the shelf break in the warm or cold regimes. Thus, the proximity of CDW to the shelf break remains unchanged. This is also confirmed by composites of potential temperature and practical salinity of warm and cold regimes (not shown), which do not show significant differences in the shelf break area. Overall, box A displays increased Ekman transport off the shelf, increased SSH gradients over the continental

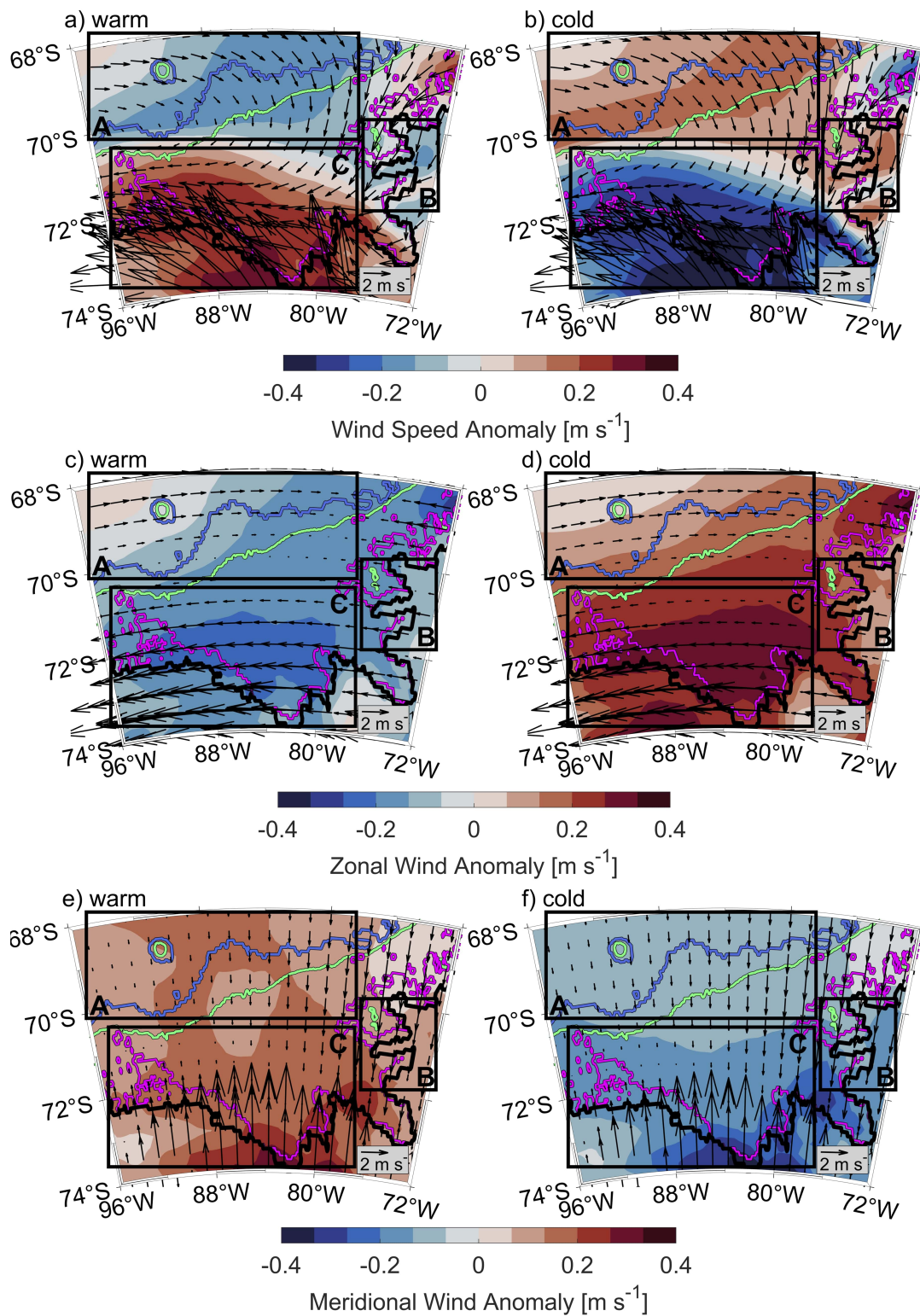


Figure 3.12: Anomalies of (a,b) wind speeds, (c,d) zonal wind components and (e,f) meridional wind components. All subfigures (a-f) are superimposed with velocity vectors from the composites for the warm (a,c,e) and cold (b,d,f) regimes. Boxes A, B and C highlight areas discussed in the text. Isobaths are coloured as in Fig. 3.2.

slope and increased frontal jet intensity in the cold regime.

Box B, which covers the eastern Bellingshausen Sea, shows a time-mean wind direction to the south and is investigated to discuss the potential impacts of wind direction and intensity on SSH and potential impacts on the Antarctic Coastal Current in warm and cold regimes. This region shows only minor differences between winter and summer (Figs. A1, A2, A3), so the seasonality is not discussed further. The cold regime shows increased southward winds and slightly weakened westward winds (Fig. 3.12d,f), so overall wind speeds (Fig. 3.12b) increase. The increased southward winds in the cold regime increase the Ekman transport towards the eastern boundary of the Bellingshausen Sea and possibly southeast into Latady Bay. These conditions likely explain why the overall decrease in SSH on the continental shelf in the cold regime is more pronounced in the centre of the Bellingshausen Sea and Eltanin Bay, and less pronounced towards the eastern boundary and within Latady Bay (Fig. 3.11d). The net result is that the zonal SSH gradients increase in Box B in the cold regime, consistent with the increase in the south-westward flowing Antarctic Coastal Current in this area (Fig. 3.11f). Conversely, the warm regime demonstrates decreased wind speeds in box B (Fig. 3.12a), reducing the Ekman transport and thus the SSH gradients and the strength of the Antarctic Coastal Current (Fig. 3.11e).

Box C, which covers the southern Bellingshausen Sea, shows a time-mean wind direction to the north-west and is investigated to highlight impacts of wind direction and intensity on sea ice concentration, heat loss to the atmosphere and cold, dense water formation in warm and cold regimes. In box C, it is the warm regime that shows increased wind speeds (Fig. 3.12a), with an increase in both the westward and northward wind components (Fig. 3.12c,e), especially in winter. We suggest that these wind conditions are responsible for reduced sea ice concentration in the warm regime (Fig. 3.13a), where sea ice is more rapidly blown away from the coast to the northwest, which enlarges the coastal polynya. The reduction in sea ice concentration results in increased heat loss to the atmosphere and thus an increase in convection and the formation of cold dense water in winter. In the warm regime, the sea ice concentration near the coast in the southern Bellingshausen Sea is reduced in both winter and summer in comparison to the cold regime (Fig. A4). The cold regime has reduced wind speeds in box C (Fig. 3.12b), which will increase the sea ice concentration all year round (Fig. 3.13b) and thus reduce heat loss to the atmosphere, convection and wintertime formation of cold dense water. Periods of reduced sea ice concentrations in warm years (Fig. 3.14a) allow for an on

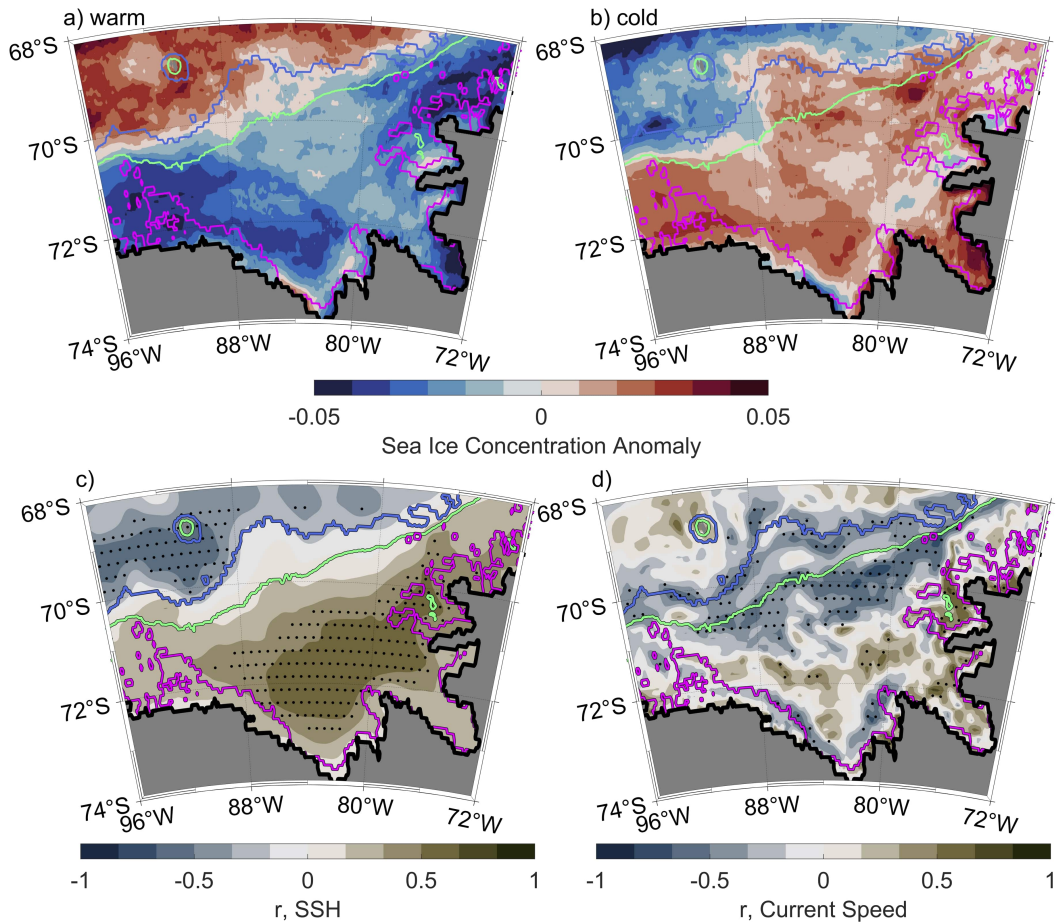


Figure 3.13: (a,b) Sea ice concentration anomalies for the warm (a) and cold (b) composites. (c,d) Map of the correlation between the PC of the EOF for (c) SSH and (d) current speed averaged from the surface to 300 m. Stippling on (c) and (d) indicates statistically significant areas at a confidence level of 95%, with the critical values estimated by bootstrapping. Isobaths on panels a-d are coloured as in Fig. 3.2.

average deeper mixed layer depth (94 ± 21 m) and a deeper ventilation of cold, fresh surface waters (Fig. 14b,c) that erodes the CDW layer below. Periods of increased annual mean sea ice concentration in cold years (Fig. 3.14a) show an on average shallower mixed layer depth (64 ± 20 m) and less deep ventilation of cold, fresh surface waters (Fig. 3.14b,c). This reduced seasonality results in a slow build-up of mCDW. Note that the location shown in Fig. 3.14 is near the edge of increased sea ice concentration further to the west in cold years (Fig. 3.13b). Thus, increased salinity during the periods of cold, dense water formation in winter (Fig. 3.14c) is related to brine rejection during sea ice formation. The gradual warming seen in the bottom temperatures (Fig. 3.14d) is consistent with the net southward heat transport across 72°S into Eltanin and Latady bays and positive air-sea fluxes south of 72°S (ocean heat uptake) in cold years (Fig. 3.10b,c).

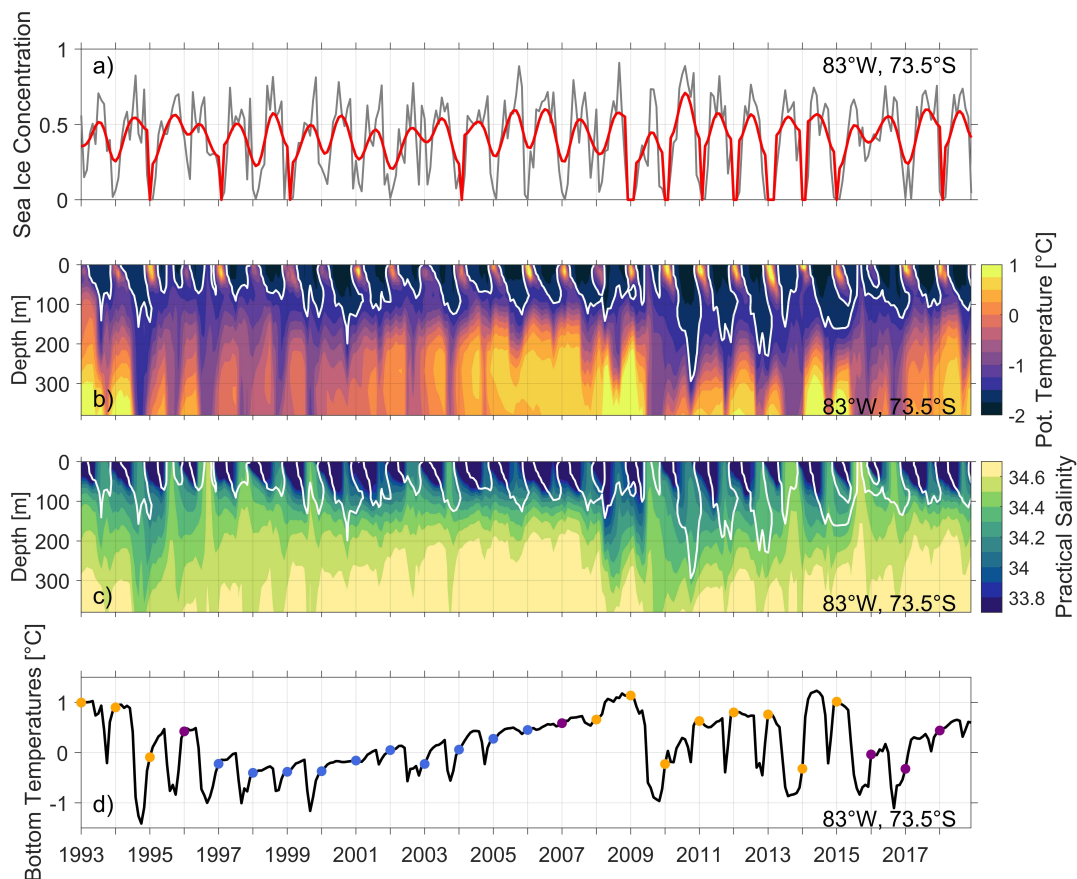


Figure 3.14: (a) Timeseries at 83°W, 73.5°S, showing: (a) monthly sea ice concentration (grey) and monthly sea ice concentration smoothed over 12 months (red), Hovmöller diagrams of (b) potential temperature and (c) practical salinity and (d) bottom temperatures. The white contour marks the -1.5°C isotherm associated with cold, dense water formation. The coloured dots in (d) indicate bottom temperatures for the years of the warm and cold regime as defined in Fig. 3.5.

The differences in sea ice cover, heat loss to the atmosphere, and subsequent formation of cold, dense water masses, provide a plausible explanation for the cooling of the water in Eltanin and Latady bays in the warm regime. The net southward heat transport across 72°S and positive air-sea fluxes south of 72°S in the cold regime provide a plausible explanation for the warming experienced in the cold years. Webber et al. (2017) presented observations of warming and cooling periods (spring 2009 and 2012) in Pine Island Bay in the Amundsen Sea. Although the years (2009 and 2012) from Webber et al. (2017) do not agree with the warming and cooling periods in the Bellingshausen Sea, the suggested mechanisms are consistent with our findings for the warm regime (cooling period, increased surface heat loss, deeper thermocline) and for the cold regime (warming period, decreased surface heat loss, shallower thermocline). In summary, our Bellingshausen Sea results imply a negative feedback mechanism that operates to maintain stable water mass temperatures in the long term: warming during the cold regime and cooling during the warm regime.

Venables and Meredith (2014) showed using observations from 1994 to 2014 near Ryder Bay on the WAP that reduced sea ice concentration leads to increased mixing and heat loss in winter, which is consistent with our results. The reduction in stratification persists into the following summer, preconditioning the water column for increased vertical mixing in the following winter so that more heat is mixed down in summer than was lost in winter. Our results in the southern Bellingshausen Sea suggest that during warm years the reduced sea ice concentration in summer and winter leads to more cold, dense water formation in winter and increased ocean heat uptake in summer (Fig. 3.14b). However, summer warming and winter cooling processes are much more variable in the warm regime than in the cold regime and do not provide a positive feedback loop suggested by Venables and Meredith (2014) on the WAP. Maintaining a long time series of year-round observations on the Bellingshausen Sea continental shelf similar to that on the WAP would be a valuable contribution to the Southern Ocean Observing System (SOOS, www.soos.aq).

Narayanan et al. (2019) argued from seal-acquired observations that in the years from 2004 to 2017 that there was no observable formation of dense shelf water in the Bellingshausen Sea. However, the density of seal data during winter months is sparse around the coast in Eltanin Bay, where convection and formation of cold dense water is found in GLORYS. Furthermore, the dense shelf water that Narayanan et al. (2019) referred to was defined as a salinity > 34.5 and temperatures $\leq -1.8^{\circ}\text{C}$ (Williams et al., 2016). This is more saline and colder than the cold dense water forming near the coast in Eltanin Bay

in GLORYS, so the possibility remains that some water, colder and denser than CDW but not as cold and dense as the definition used by Narayanan et al. (2019) was formed in the Bellingshausen Sea during this time period. However, we also acknowledge that the lack of ice shelf cavities and the lack of in situ ocean observations for data assimilation into GLORYS may impact the properties of coastal water masses in GLORYS. The modelling study by St-Laurent et al. (2015) in the Amundsen Sea demonstrated the importance of sea ice concentration and surface heat fluxes on warming and cooling periods, concluding that they directly impact ice shelf melt rates. The increased presence of buoyant ice shelf meltwater will also affect stratification in the region. In this study, we cannot confirm the impact on ice shelf melt rates and resulting water mass stratification in the Bellingshausen Sea as GLORYS does not include ice shelf cavities or ice shelf meltwater.

Overall, we have shown that changes in the ASL's location and intensity impact wind velocities, Ekman transports, SSH and current structures in the Bellingshausen Sea region. Strong correlation coefficients of SSH ($r \approx \pm 0.65$) and current speeds above 300 m ($r \approx -0.70$) with the PC to support the significance of these findings (Fig. 3.13c,d). We further demonstrate that the warm and cold regimes exhibit conditions that are linked to different tendencies of cooling and warming in association with wind-induced changes of sea ice concentration in the southern Bellingshausen Sea.

3.5 Conclusions

In this study we use the GLORYS12V1 reanalysis to study the temperature variability of waters below 300 m on the southern Bellingshausen Sea continental shelf over a period of 26 years from 1993 to 2018. The analysis of the 1st EOF mode and PC reveals a spatial pattern which demonstrates strongest temperature changes within Eltanin and Latady bays, and a temporal pattern that allows a separation into warm and cold regimes.

Our results show that our definition of warm and cold years in the Bellingshausen Sea only partly agrees with observations (Jenkins et al., 2018; Webber et al., 2017) and simulations (Dutrieux et al., 2014; Dotto et al., 2019) in the adjacent Amundsen Sea. The 1st EOF mode (Fig. 3.5) shows the opposite sign in the far west of the Bellingshausen Sea study region and agrees with the fact that the Amundsen Sea has a different variability pattern. Furthermore, our results show a negative feedback loop (warming in the cold regime, cooling in the warm regime) opposite to the positive feedback loop that Venables and

Meredith (2014) demonstrated with observations near Ryder Bay on the WAP. This might indicate that due to spatial distance and differences in atmospheric forcing between the Bellingshausen, Amundsen Seas and the WAP, warm and cold periods are not in phase in these regions.

Our analysis of the conditions and processes occurring in the warm and cold regimes reveal that changes in the ASL's location and intensity impact wind velocities and Ekman transports in the Bellingshausen Sea region. The ASL is more intense and extends further east during the warm regime than during the cold regime. A consequence of the ASL extending less far east in the cold regime is that regions north of 72°S experience higher wind speeds (increase in east and southward wind components, Fig. 3.12c,d). This increases the offshore Ekman transport and results in lower SSH on the Bellingshausen Sea continental shelf, where stronger SSH gradients above the continental slope and along the coast of Eltanin Bay amplify both the frontal jet and the Antarctic Coastal Current in the cold regime. Correlations with the PC confirm that the strongest relationship to the temperature variability below 300 m is found in the SSH ($r \approx \pm 0.65$) and current speeds above 300 m in areas affected by the frontal jet ($r \approx -0.70$). Importantly, the strong correlation between the PC and SSH (Fig. 3.13c) suggest that satellite altimetry may be able to give a remote indication of warm and cold conditions in the Bellingshausen Sea, although note that SSH from satellite altimetry is not currently as high resolution as the SSH in GLORYS (Armitage et al., 2018; Auger et al., 2022).

The warm and cold regimes are also linked to different tendencies of cooling and warming (Fig. 3.15). In the warm regime, a wind-induced reduction of sea ice results in increased heat loss to the atmosphere that drives convection and the formation of cold dense water in winter, which is associated with a cooling of Eltanin and Latady bays and a net northward heat transport. In contrast, increased sea ice conditions in the cold regime result in weakened heat loss to the atmosphere and a decrease in convection and formation of cold dense water in winter, which is associated with a gradual warming of Eltanin and Latady bays and a net southward heat transport.

Climate model simulations indicate that the ASL will likely migrate poleward and eastward during the remainder of this century (Hosking et al., 2016), which will cause a southward migration of eastward winds (Holland et al., 2019) and lead to stronger eastward winds along the continental slope of the Amundsen and Bellingshausen seas (Hosking et al., 2016). Stronger eastward winds above the continental slope would increase the offshore Ekman transport and result in even lower SSH on the Bellingshausen Sea continental shelf. Stronger

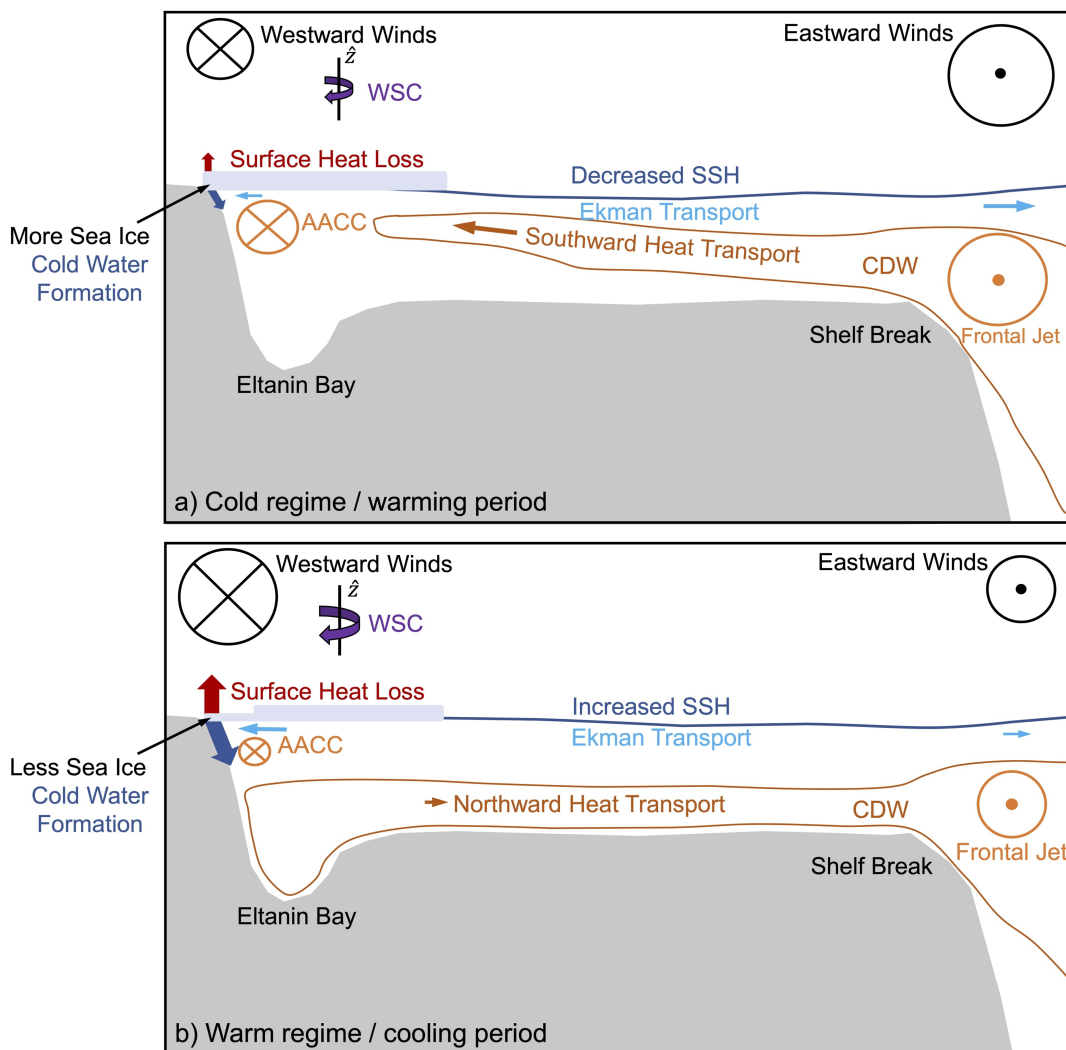


Figure 3.15: Schematics covering a meridional section from coast to shelf break presenting processes and conditions referred to in the main text during (a) the warming period in the cold regime and (b) cooling period in the warm regime. Wind stress curl is indicated with WSC.

SSH gradients above the shelf break and along the eastern and southern coast of the Bellingshausen Sea would result in an intensification of both the frontal jet and the Antarctic Coastal Current. A southward migration of the ASL might also result in weakened winds in the southern Bellingshausen Sea, as the strong north-west winds would move further south over the continental land mass. This would lead to an increase of sea ice concentration in the southern Bellingshausen Sea, and thus a reduction in the heat loss to the atmosphere and a decrease in convection and cold water formation in winter. This would suggest a gradual warming of Eltanin and Latady bays in the future.

Chapter 4

Stirring across the Antarctic Circumpolar Current's Southern Boundary at the Greenwich Meridian, Weddell Sea

This chapter has been submitted to Ocean Science special issue 'The Weddell Sea and the ocean off Dronning Maud Land: unique oceanographic conditions shape circumpolar and global processes – a multi-disciplinary study (OS/BG/TC inter-journal SI)'.

R. Oelerich, K. J. Heywood, G. M. Damerell, S. Swart, M. du Plessis and L. C. Biddle (in review). R. Oelerich has carried out the research and prepared the paper. K. J. Heywood and G. M. Damerell provided advice on the processing of glider data and all co-authors provided feedback on earlier drafts.

4.1 Introduction

The Southern Ocean hosts one of the largest current systems on Earth, the Antarctic Circumpolar Current (ACC). The eastward flow of the ACC circulates the Southern Ocean's major source of heat, Circumpolar Deep Water (CDW), and is characterised by strongly tilted isopycnals shoaling poleward (Orsi et al., 1995).

Traditionally, the ACC is described with the three major deep reaching fronts representing boundaries between zones with distinct water mass properties. The seasonal and interannual variability of transport, extent and location of these fronts have been studied extensively over past decades using water mass properties (e.g., Orsi et al., 1995; Kim and Orsi, 2014), fixed sea surface height (SSH) contours, gradients of SSH and mean transport positions (e.g., Sokolov and Rintoul, 2007; Sokolov and Rintoul, 2009a; Sokolov and Rintoul,

2009b; Billany et al., 2010; Gille, 2014; Gille et al., 2016). Enhanced density gradients across the fronts support strong oceanic jets that form the main contribution to the ACC transport and act as barriers to cross-frontal mixing (Naveira-Garabato et al., 2011; Thompson and Sallée, 2012; Chapman and Sallée, 2017). In some studies, the traditional three-front view of the ACC has been expanded by including the Southern Boundary of the ACC to the south (e.g., Billany et al., 2010). However, its definition is not based on the characteristics of a dynamical front (Talley et al., 2011), but rather as a boundary of water mass properties that separates warm ACC waters from colder water masses further south (Orsi et al., 1995). Therefore, the Southern Boundary is often not considered as part of the ACC (Sokolov and Rintoul, 2007) and its changing properties that can enhance or suppress cross-frontal mixing have not been studied extensively in the past.

The focus of this study is the Southern Boundary of the ACC (Fig. 4.1a), which is traditionally, climatologically and globally defined as the southernmost limit of Upper Circumpolar Deep Water (UCDW, $\Theta > 1.5^{\circ}\text{C}$ and $S > 34.5$, (Orsi et al., 1995)). The proximity of the Southern Boundary to the continental shelf break varies around Antarctica, where its northernmost displacements are located in areas of cyclonic gyres with clockwise surface circulation in the Weddell and Ross Seas. Specifically in areas where the Southern Boundary is located close to the continental shelf, such as in the West Antarctic Sector, it is considered to play an important role in processes that can aid or oppose the influx of warm waters onto the continental shelf (e.g., Dinniman and Klinck, 2004; Jenkins and Jacobs, 2008; Martinson and McKee, 2012). The Southern Boundary and its associated frontal jet further represent the southernmost boundary to mixing (e.g., Naveira-Garabato et al., 2011; Thompson and Sallée, 2012; Chapman and Sallée, 2017; Chapman et al., 2020) and mark the barrier between the northern limit of sea ice formation and the ACC. Thus, whether mixing across the Southern Boundary in summer influences the sea ice formation in the following winter is an important question addressed in this study.

Previous studies have shown that the mean positions of the major ACC fronts have not shifted southward in response to southward migrating, intensifying westerly winds due to recent climate change (e.g., Chapman et al., 2020; Gille, 2014; Shao et al., 2015; Gille et al., 2016). However, analysed in situ observations, historical reconstructions of ocean conditions, ensemble of coupled climate model simulations and idealized experiments have shown that the ACC's core eastward flow (at 52°S) has accelerated over the past decade (Shi et al., 2021). The acceleration in eastward flow of the ACC was not attributed

to changes in wind strength, but rather to intensifying meridional density gradients in response to upper ocean warming. Nonetheless, satellite altimetry and eddy resolving models suggested an intensifying eddy field within the ACC over the past decade in response to the long-term increase in westerly winds (e.g., Meredith and Hogg, 2006; Hogg et al., 2015; Patara et al., 2016). Studies have shown that mesoscale eddies across the ACC fronts sharpen density gradients and thus strengthen the frontal jets (Williams et al., 2007; Hughes and Ash, 2001), which in turn act to suppress the mixing across the ACC fronts and greatly reduce the meridional exchange of properties, such as heat and carbon (Naveira-Garabato et al., 2011). As a consequence, regions where the ACC fronts have weaker frontal jets, such as downstream of large bathymetric features, are characterized by less suppressed mixing across fronts and thus elevated meridional exchange of properties (e.g., Naveira-Garabato et al., 2011; Thompson and Sallée, 2012). The majority of studies almost entirely focused on the mean positions, transports and barrier properties of the major ACC fronts, whereas processes and dynamics affecting the frontal structure and the frontal jet of the Southern Boundary and meridional exchange of properties across it are poorly understood.

In this study, the Southern Boundary’s frontal characteristics, barrier/blender properties and short-term variability in the northern Weddell Sea are investigated. We specifically highlight the impacts of mesoscale eddies on the frontal structure of the Southern Boundary and test the hypothesis that eddies interacting with the Southern Boundary affect density gradients, frontal jet intensity, mixing length scales and mixing across the Southern Boundary. For our analysis we use repeat glider transects crossing the Southern Boundary at the Greenwich Meridian (Fig. 4.1b) and satellite altimetry to:(i) describe the Southern Boundary’s frontal structure and frontal jet intensity, (ii) identify the location, rotational direction and dynamics of mesoscale eddies interacting with the Southern Boundary and (iii) establish how eddies impact the Southern Boundary’s barrier/blender properties. We further investigate changes of the Southern Boundary’s location and frontal jet intensity using satellite altimetry from 1993 to 2020 and discuss the potential implications for the barrier/blender properties of the front as well as impacts on sea ice extent. This study is organised as follows: section 4.2 introduces the Southern Boundary’s frontal structure and its variability using the five glider transects. Section 4.3 describes and quantifies the effects of a mesoscale eddy on the frontal structure using two glider transects (transects A and C, Fig. 4.1b) . Section 4.4 evaluates mixing length scales and barrier properties of the Southern Boundary. Section 4.5 provides

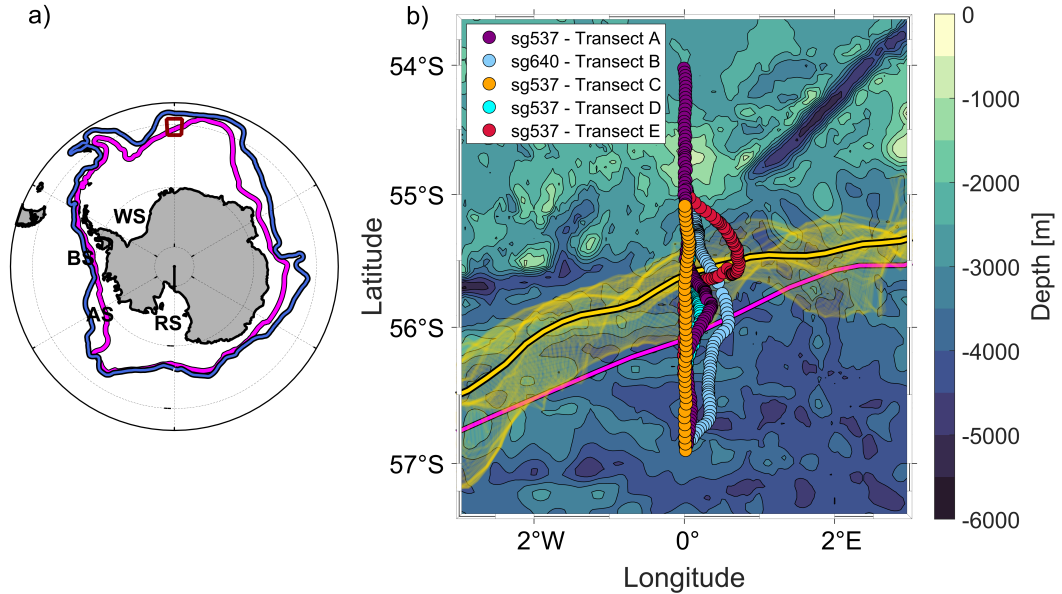


Figure 4.1: (a) Map of the Southern Ocean with the study region outlined by a red box and the climatological mean location of the Southern Boundary (magenta contour in (a) and (b)) after Orsi et al. (1995). (b) Five glider transects superimposed on the bathymetry Schaffer et al. (2019). Each coloured dot represents the position of the glider at the surface following a dive. The -1.16 m contour of absolute dynamic topography from satellite altimetry is shown as a mean over the observational time period (18th October 2019 to 18th February 2020, bold yellow) and daily over the same time period (transparent yellow). The significance of this contour is discussed in the main text of section 4.3. Key geographic features in (a) are labelled: Ross Sea (RS), Amundsen Sea (AS), Bellingshausen Sea (BS) and Weddell Sea (WS).

the main conclusions and offers suggestions for future work.

4.2 Frontal Structure of the Southern Boundary

As part of the 'Robotic Observations And Modelling in the Marginal Ice Zone' (ROAM-MIZ, www.roammiz.com) project, two Seagliders (SG537 and SG640) were deployed at the Greenwich Meridian in the northeastern Weddell Sea (SG537: 0.00°W and -55°S , SG640: 0.02°W and -55.01°S) and obtained a total of five repeated crossings of the Southern Boundary (Fig. 4.1, transects A-E). The average time taken to complete one crossing of the front was 16.6 days (transect A - 6th to 29th Nov (321.85 km); transect B - 12th Nov to 3th Dec (211.90 km), transect C - 29th Nov to 7th Dec (202.13 km); transect D - 7th Dec to 22th Dec (145.56 km) and transect E - 22nd Dec to 6th Jan (152.42 km). All ocean properties use the TEOS10 equation of state (IOC et al., 2010) and therefore temperature will refer to conservative temperature [$^{\circ}\text{C}$] and salinity will refer to absolute salinity [g kg^{-1}] throughout this study. The glider profiles

of temperature and salinity (Fig. 4.2) are vertically-gridded with an interval of 2 m. The gliders also provide an estimate of the currents experienced by the gliders during each dive, the dive average current (DAC). Independently from the DAC, we further provide an estimate of the surface currents by calculating the surface drift of the glider during communication with the satellite at the surface. The glider transects are observed in a cross-front orientation, so that the cross-transect velocities capture the flow associated with the Southern Boundary. The absolute along-stream geostrophic velocities are calculated by referencing the geostrophic shear to the component of the DAC perpendicular to the transects. The geostrophic velocities are then horizontally smoothed with a 15 km moving mean filter, which corresponds to the Rossby radius of the region of interest.

This study uses the daily satellite-altimetry-derived global sea level data product (SEALEVEL_GLO_PHY_L4_MY_008_047) provided by the Copernicus Marine Environment Monitoring Service (CMEMS) with a horizontal resolution of $0.25 \times 0.25^\circ$ (approximately 28 km x 16 km in the study region). It covers the period from 1993 onward (DOI: <https://doi.org/10.48670/moi-00148>, 2022) incorporating all altimetry-carrying Copernicus missions (Sentinel-6A, Sentinel-3A/B) and other collaborative missions (e.g.: Jason-3, Saral[DP]/AltiKa, Cryosat-2, OSTM/Jason2, Jason-1, Topex/Poseidon, Envisat, GFO, ERS-1/2, Haiyang-2A/B) (Pujol, 2022). Typically, most recent products are available with a 10-month delay. Absolute dynamic topography (ADT) representing sea surface height above the geoid, sea level anomalies (SLA) and surface geostrophic currents up to December 2020 are used in this study. Note that the SLA provided by the altimetry are relative to the 20-year mean from 1993 to 2012.

All glider transects (Fig. 4.2 and Fig. 4.3a,c) display water masses typical of the Southern Boundary at the Greenwich Meridian as identified in previous studies (e.g., Orsi et al., 1995).

The warming and freshening of the near surface water masses (top 50 m) from transect A to transect E (Fig. 4.2) are due to solar radiation and sea ice melt respectively as expected during austral spring and summer (October-January observations). The seasonal warming and freshening causes properties, such as temperature and salinity, to deviate from the mean sections more strongly near-surface than at depth (Fig. 4.3b,d). Antarctic Surface Water (AASW) occupies the top 150-200 m and always lies above Upper Circumpolar Deep Water (UCDW, 200-750 m). UCDW and Lower Circumpolar Deep Water (LCDW, 750-1000 m) occur north of the Southern Boundary. The southernmost

limit of UCDW in each glider transect locates the Southern Boundary within 55.55 to 55.82°S (28 km). This highly variable frontal region is identified by greater standard deviations of temperature and salinity (Fig. 4.3b,d) throughout the water column. The southernmost extent of UCDW (55.82°S) is found in transect D (Fig. 4.2d,i) and the northernmost extent of the southernmost UCDW (55.55°S) is found in transect C (Fig. 4.2c,h). The southernmost extent of UCDW found in these transects corresponds well with the location of strong ADT gradients which mark the presence of a frontal jet. The location of strong ADT gradients is in agreement with the work of Billany et al. (2010) who found the Southern Boundary co-located with the southernmost strong ADT gradients across the ACC between 1993 and 2008 within the same region. Moreover, the examination of the daily satellite altimetry over the entire area shown in Fig. 4.1 reveals that the -1.16 m ADT contour is co-located with strong ADT gradients and strong surface velocities provided by the altimetry that further align with strong velocities indicated by the DAC and surface drift (Fig. 4.4). Furthermore, the -1.16 m ADT contour is co-located with the southernmost extent of UCDW at the times when the gliders cross the Southern Boundary. This study therefore uses the -1.16 m ADT contour to identify daily locations of the Southern Boundary during the observational period. Note that the identification of the Southern Boundary using the fixed -1.16 m ADT contour is only valid for the observational period (approx. 2 months) and is as previous studies (e.g., Gille, 2014; Gille et al., 2016) demonstrated not appropriate over longer timescales, such as multiple years.

Across the Southern Boundary, most transects (A,B,D,E) demonstrate strong horizontal density gradients (Fig. 4.2 and Fig. 4.3) across the Southern Boundary. The 27.73 kg m⁻³ and 27.93 kg m⁻³ isopycnals mark the upper and lower boundary of UCDW and are in general shallowing to the south. The 27.93 kg m⁻³ isopycnal slopes strongly at the location of the Southern Boundary. In addition, in some areas, individual for each transect, the 27.73 kg m⁻³ isopycnal bowls downward. These areas coincide with colder and fresher water mass properties than in the ambient water in the upper 250 m of the water column and are located south of the Southern Boundary. In contrast, transect C demonstrates weaker horizontal density gradients in comparison to the other transects, which is implied by a less steeply sloping 27.93 kg m⁻³ isopycnal. The 27.73 kg m⁻³ isopycnal in transect C also does not bowl downwards and does not show the coincident changes in water mass properties as demonstrated in the other transects.

In summary, we have shown that the location of the Southern Boundary

and its frontal structure change on short time scales (approx. 16 days). The following section will focus on transects A and C to identify the processes that influence the frontal structure and specifically modify the horizontal density gradients across the front.

4.3 Effects of Mesoscale Eddies on Frontal Structure and Frontal Jet

In this study, mesoscale eddies in close proximity to the Southern Boundary (between 54.88°S and 56.63°S) are identified using SLA as introduced in section 4.2. The specific contours of SLA (0.06, 0.07 and 0.08 m) are chosen to identify mesoscale eddies influencing the frontal structure of the Southern Boundary (Fig. 4.4). For transect A, the SLA contours (Fig. 4.4a) reveal a mesoscale eddy (approx. 40 km wide) located to the south of the Southern Boundary at the Greenwich Meridian. In transect A, the glider captures the eddy's core and thus provides information on its rotational direction as well as its water mass properties. Surface current velocities from the altimetry, DAC and surface drift from the glider (Fig. 4.4a) provide evidence for a clockwise-rotating eddy with eastward velocities at its northern edge (55.8°S) and westward velocities at its southern edge (56.2°S). Due to its clockwise rotation, it is implied that the identified eddy is a cold-core eddy. Within a matter of days, the clockwise eddy is advected to the east with the ACC and is thus not captured again in transect C. As a result, neither sea surface slopes nor DAC nor surface drift from the glider (Fig. 4.4b) indicate a clockwise rotation. Thus, transect C contains information on the Southern Boundary's frontal structure without an eddy influencing it.

The temperature maximum for each vertical profile of transects A and C (Figs. 4.4 and 4.5) displays higher temperatures ($\Theta > 1.8^\circ\text{C}$) north and colder temperatures ($\Theta < 0.65^\circ\text{C}$) south of the Southern Boundary, thus demonstrating a warm to cold temperature gradient from north to south in both transects. The main differences between transect A and C in the temperature maximum occur in the transition zone between the warm regime in the north and the cold regime in the south. This is also the region where the clockwise eddy, captured in transect A, is located. Within the transition region, the temperature maximum in transect A demonstrates significantly lower temperatures (0.65-0.8°C at 56°S) than in transect C (Fig. 4.5), which provides further evidence that the captured eddy in transect A is a cold-core eddy.

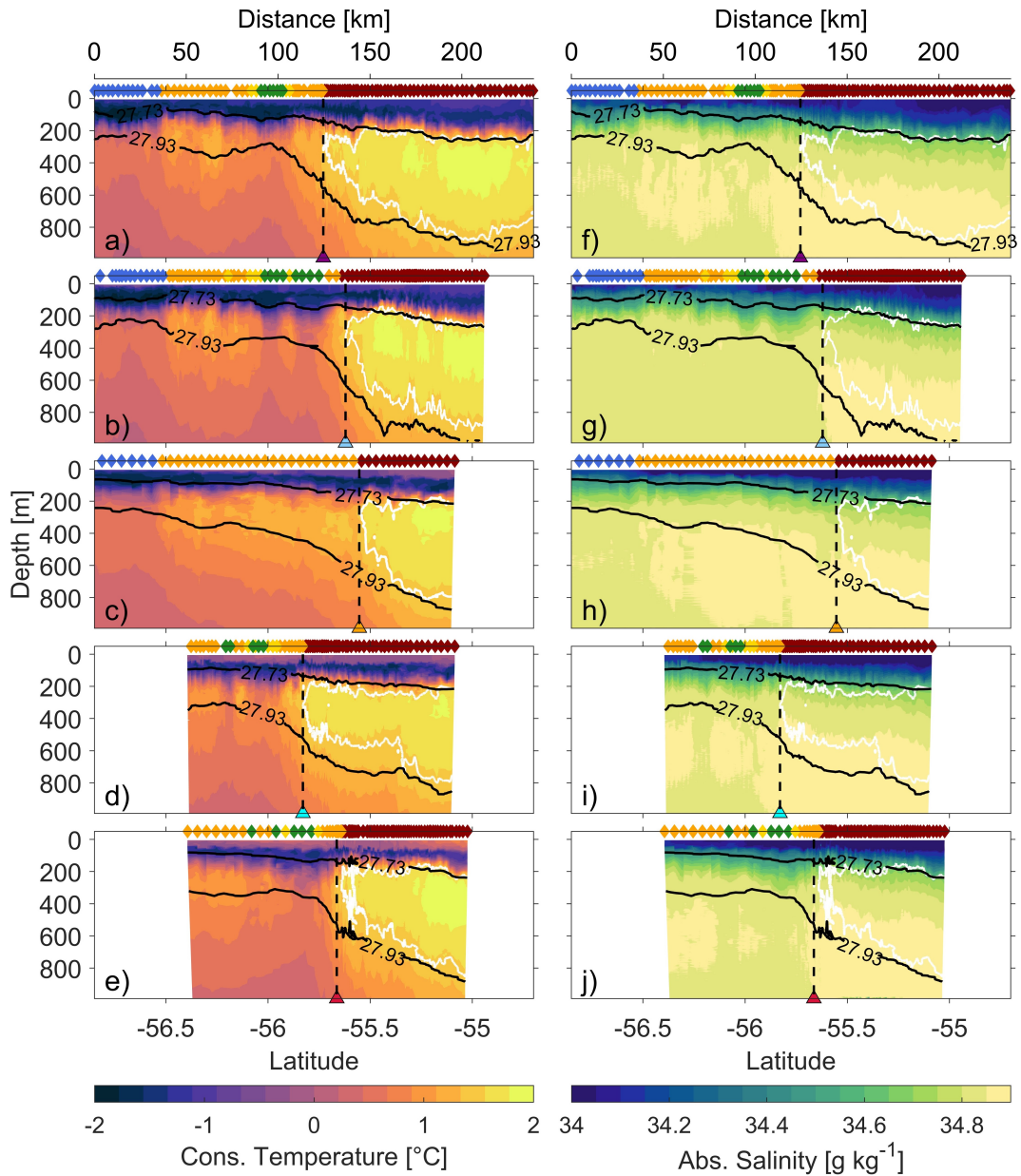


Figure 4.2: Hydrography of glider transects A-E showing conservative temperature (left column, panels a-e) and absolute salinity (right column, panels f-j) for each transect. Potential density contours of 27.73 kg m^{-3} and 27.93 kg m^{-3} are shown in black. The 1.5°C isotherm is shown with white contours. The triangles at the bottom of each panel, and the black dashed line extending upwards from each triangle, indicate the location of the Southern Boundary defined as the southernmost extent of UCDW (Orsi et al., 1995). The triangles are colored for each individual transect as in Fig. 1, and the same transect color coding is used in Fig. 4.3. The colors at the top of each panel represent our classification into areas north of the Southern Boundary (red), within a transition zone (orange), within the core of an eddy (green) and on the outer edges of an eddy (yellow), and south of the Southern Boundary (blue). This colour coding is discussed in section 4.3.

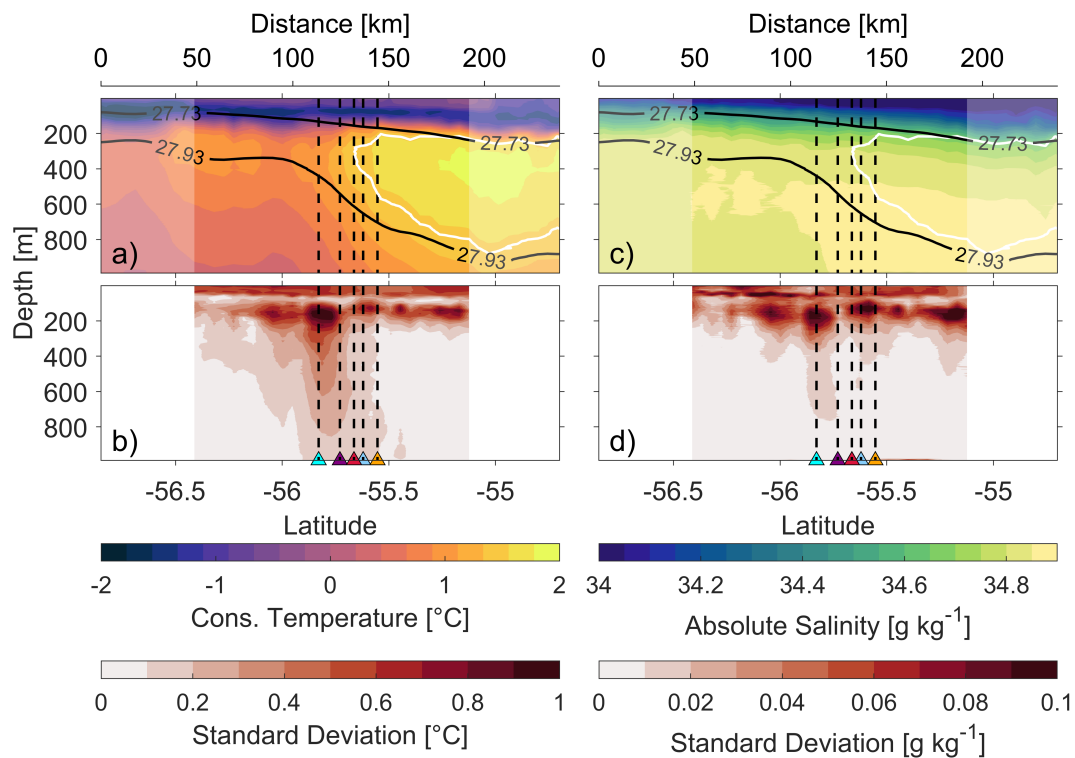


Figure 4.3: Mean (a,c) and standard deviation (b,d) of all glider transects A-E for (a,b) conservative temperature and (c,d) absolute salinity. The coloured triangles at the bottom of panels (b,d), and black dashed lines extending upwards from them are as in Fig. 4.2. Data from each transect are binned to the same 5 km horizontal grid and then averaged (mean) for all transects. Partially shaded areas on (a,c) indicate areas that do not have data from all transects. Mean isopycnals 27.73 kg m⁻³ and 27.93 kg m⁻³ are shown in black. The white contour indicates the mean 1.5 °C contour.

North of the Southern Boundary, Θ/S profiles (Figs. 4.6 and 4.7) converge towards similar temperatures and salinities ($\Theta > 1.5^\circ\text{C}$ and $S > 34.7 \text{ g kg}^{-1}$) at the base of the thermocline (230 m), which represents UCDW. LCDW is identified below the UCDW layer with slightly lower temperatures ($\Theta \approx 0.6^\circ\text{C}$) and similar salinities ($S > 34.7 \text{ g kg}^{-1}$). In the temperature transition zone, lower temperatures between $0.2\text{--}1.2^\circ\text{C}$ indicate the presence of moderately to heavily modified CDW (mCDW), which is representative of the temperature transition zone in both transects. The clockwise eddy identified in transect A (Fig. 4.6 a,d,e) presents properties similar to the cold regime but with slightly higher temperatures (about 0.4 to 0.6°C higher) below the thermocline and slightly reduced salinities above the thermocline. The similar water mass properties of the eddy and the cold regime suggest that the eddy originated south of the Southern Boundary.

Geostrophic velocities referenced to the DAC (Fig. 4.8) reveal the frontal jet associated with strong density gradients. Transect A has the most intense jet with an eastward core velocity of up to 80 cm s^{-1} and a meridional extent of about 50 km. In contrast, the frontal jet associated with smaller density gradients is weaker and broader in transect C with an eastward core velocity of up to 60 cm s^{-1} and a meridional extent of about 80 km. The southern edge of the frontal jet is located between $55.5\text{--}56^\circ\text{S}$ in both transects and is consistent with the Southern Boundary's location indicated by the southernmost limit of UCDW (Fig. 4.2) and the gradient of ADT (Fig. 4.8a,c). Westward velocities south of the Southern Boundary at a depth of 80–400 m between $56\text{--}56.5^\circ\text{S}$ in transect A are consistent with the location and cyclonic rotation of the eddy (Fig. 4.4a) and indicate the eddy's southern edge. Both transects (Fig. 4.8a,b) show another eastward flow further south ($56.25\text{--}56.75^\circ\text{S}$) with velocities of up to 30 cm s^{-1} , which marks the boundary between the transition zone and the cold regime south of the Southern Boundary.

The temperature of the temperature maximum for each transect is used to divide each transect into segments (Fig. 4.5). We introduce a color-coding scheme to show whether a vertical profile is located to the north or south of the Southern Boundary, within the temperature transition zone or within the cold-core eddy. The color-coded segments are used in Figs. 4.2, 4.5, 4.6, 4.7, 4.8, 4.9 and 4.10. Each transect is segmented by the following criteria:

In summary, we have shown that a clockwise, cold-core eddy located south of the Southern Boundary influences the frontal structure and strengthens the density gradients across the front and intensifies its frontal jet. Additionally, we have demonstrated that density gradients and the frontal jet are weaker across

Table 4.1: Segmentation values based on the temperature of the temperature maximum for each vertical profile across each transect. The color-coding scheme introduced in Fig. 4.5 is based on these values.

Segments	Θ_{\max} [$^{\circ}\text{C}$]
North of the Southern Boundary	> 1.5
Temperature Transition Zone	0.95-1.5
Outer Eddy	0.8-0.95
Eddy Core	0.65-0.8
South of the Southern Boundary	< 0.65

the Southern Boundary after the eddy has been advected eastward. Furthermore, the characterisation of different regimes across the Southern Boundary region using the temperature maximum for each vertical profile reveals specific water mass properties for each regime. We further established, based on the similar water mass properties of the cold-core eddy and the cold regime, that the eddy originated south of the Southern Boundary. In the following section, we address how the changes in the frontal structure of the Southern Boundary impact its barrier/blender properties.

4.4 Effects of Mesoscale Eddies on Mixing Length Scales

Ferrari and Nikurashin (2010) demonstrated that strong mean flows, such as those found within the ACC fronts, can suppress lateral mixing. Naveira-Garabato et al. (2011) further quantified this effect by estimating mixing length scales (MLS) across the three major fronts of the ACC using hydrographic sections with a mesoscale resolution (approx. 50 km station separation). Naveira-Garabato et al. (2011) found that the eddy diffusivities are typically suppressed across the ACC's frontal jets, primarily as a result of reduced mixing lengths. Here we calculate MLS from the highly-resolved transects A and C to assess whether the passage of an eddy across the Greenwich Meridian affects the ability of water to mix across the Southern Boundary.

First, temperature is linearly interpolated onto a potential density grid with an interval of 0.02 kg m^{-3} in the vertical, as used by Naveira-Garabato et al. (2011), and 5 km in the horizontal. Subsequently, the temperature field is spatially smoothed with a 30 km (twice the Rossby Radius) x 0.08 kg m^{-3} moving median filter to filter out small scale effects and approximate a large-scale temperature field, Θ_m , and a large-scale gradient along potential density

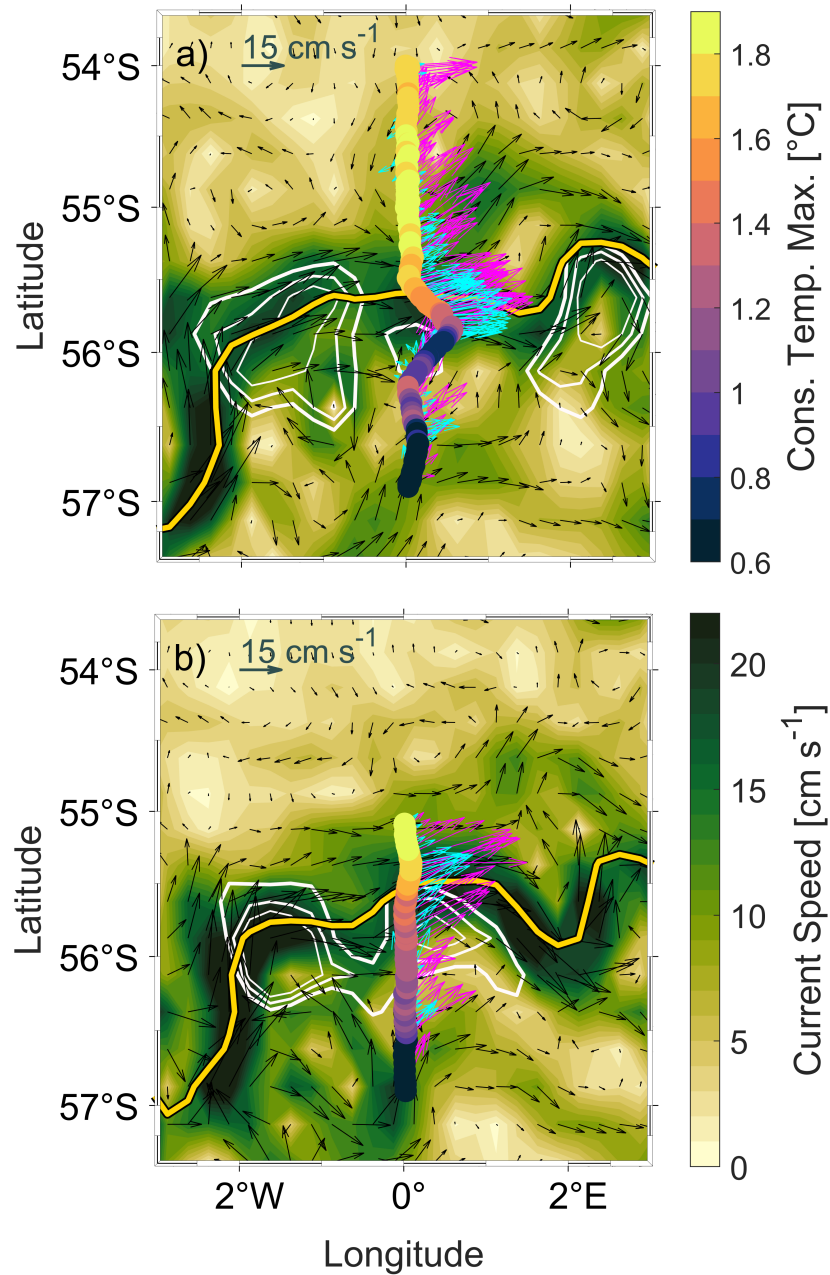


Figure 4.4: Maps of altimetric sea surface geostrophic velocities (velocity vectors in black and speed in green shading) during the glider crossings of the Southern Boundary for (a) 18th November 2019 (transect A) and (b) 3rd December 2019 (transect C). Bold yellow contours indicate the -1.16 m ADT contour on the same days. Coloured dots show the temperature maximum for each vertical profile along the respective transect. Glider dive average currents (magenta vectors) and glider surface drift speeds (cyan vectors) are superimposed. White contours show sea level anomalies of 0.06, 0.07 and 0.08 m (thin to bold) and indicate the location of cyclonic eddies in close proximity to the Southern Boundary.

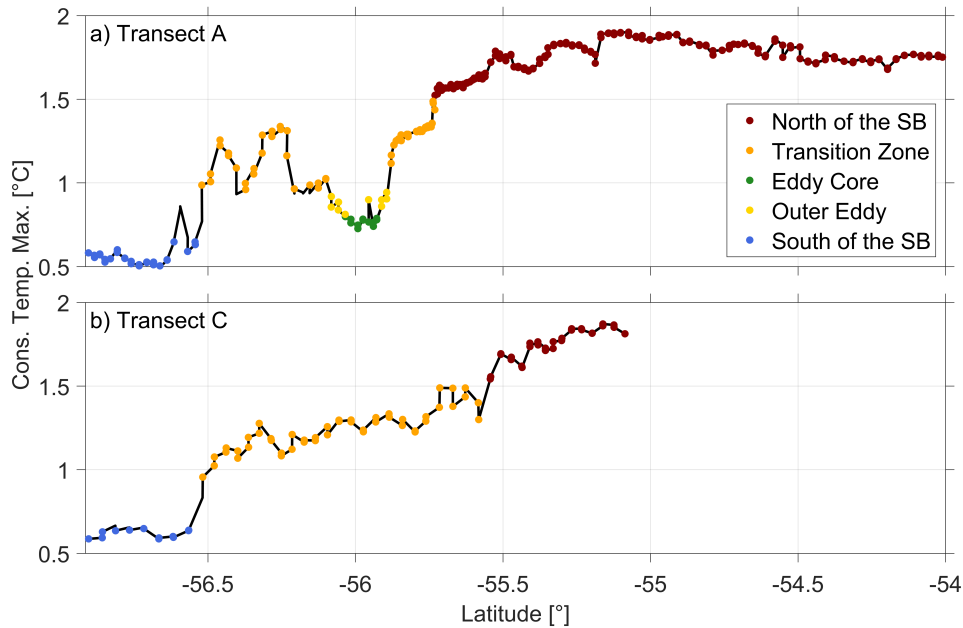


Figure 4.5: The colour-coded temperature maximum for each vertical profile along (a) transect A and (b) transect C. The segmentation values for each regime, on which the color-coding is based, are defined in Table 4.1 in section 4.3.

surfaces, $\nabla_{\rho}\Theta_m$. Θ_{rms} is a measure of the temperature fluctuations calculated by producing the root mean square of the difference between the spatial-mean temperature field and the temperature fluctuations, Θ' . The mixing length scales, L_{mix} , across the Southern Boundary are then calculated from:

$$L_{mix} = \frac{\Theta_{rms}}{\nabla_{\rho}\Theta_m}. \quad (4.1)$$

We further calculate potential vorticity, which is a largely and materially conserved property in the ocean interior that can be used to identify the susceptibility of the flow to instabilities (Haine and Marshall, 1998). The Ertel potential vorticity (PV) can be written as:

$$PV = (f\hat{\mathbf{k}} + \nabla \times \mathbf{u}) \cdot \nabla b, \quad (4.2)$$

where f is the Coriolis parameter, $\hat{\mathbf{k}}$ is the local vertical vector of unit length, g the gravitational acceleration, $\nabla \times \mathbf{u}$ is the relative vorticity, where \mathbf{u} is the velocity vector. $b = -g((\rho - \rho_0)/\rho_0)$ is the buoyancy, where ρ is the ocean density and ρ_0 is the reference ocean density. In this study, the glider transects only provide the cross-section (along-stream) velocity component. Therefore the PV has to be simplified to achieve the observational PV (Azaneu et al.,

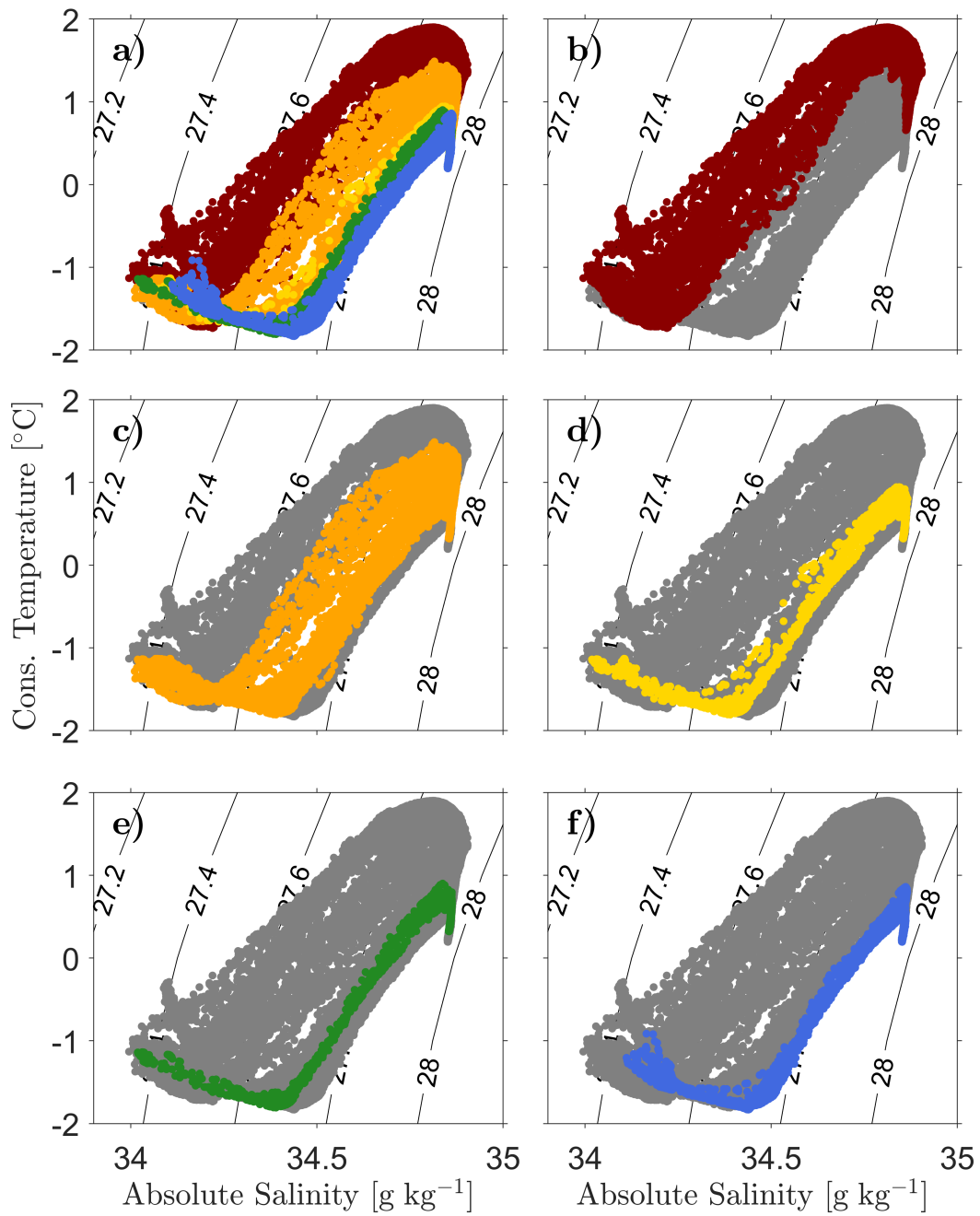


Figure 4.6: Θ/S diagrams for Transect A with colour-coding defined in Table 4.1 and colours shown in Fig. 4.5. (a) All profiles of transect A shown with colour-coding. (b-f) Grey dots show all profiles in the transect, with coloured dots showing the profiles: (b) north of the Southern Boundary, (c) in the temperature transition zone, (d) in the outer eddy, (e) in the eddy core and (f) south of the Southern Boundary.

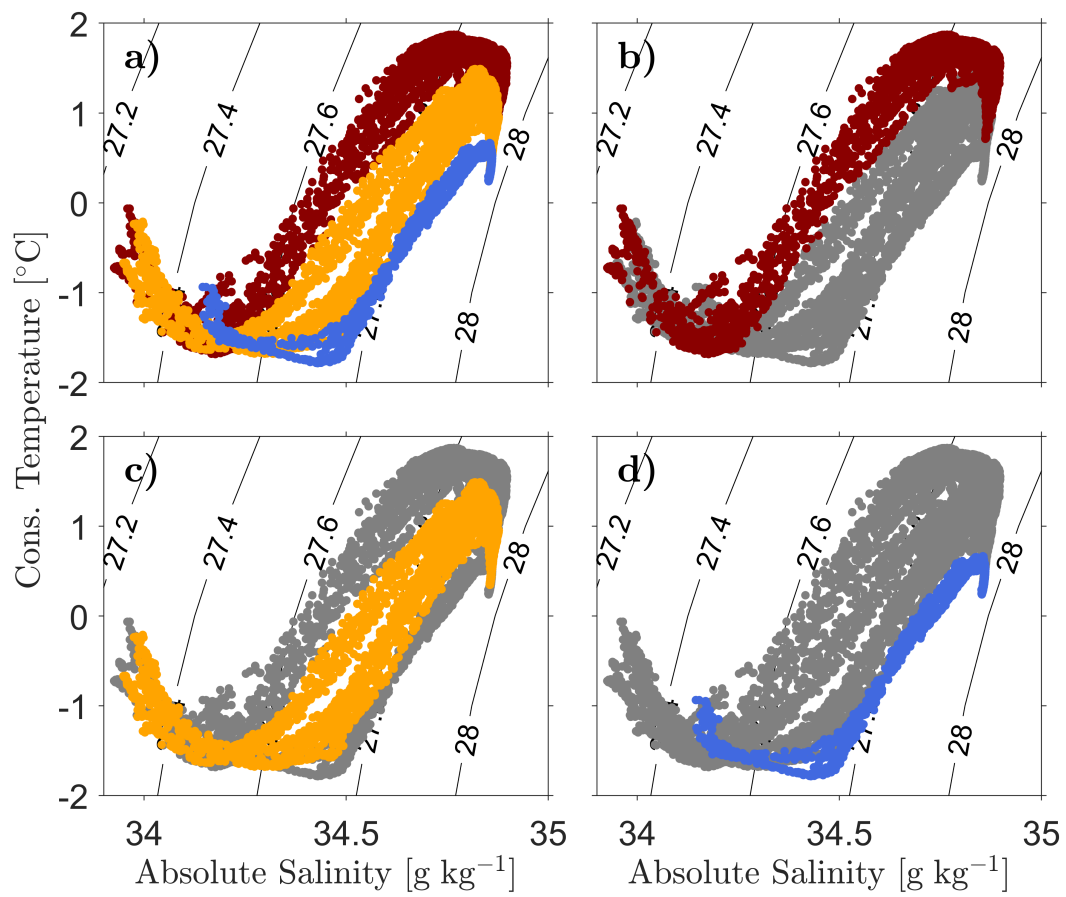


Figure 4.7: As for Fig. 4.6 but for transect C.

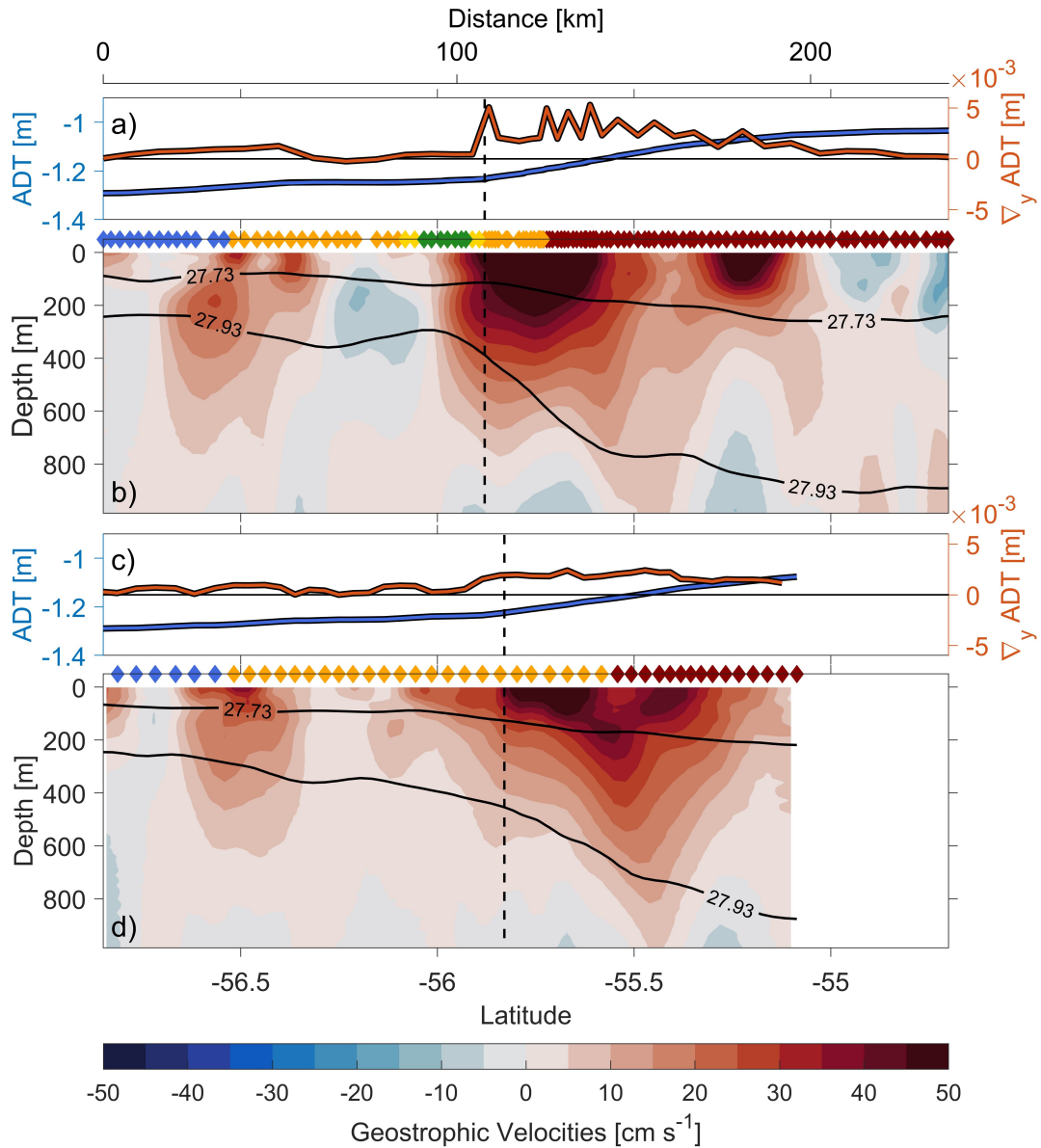


Figure 4.8: Real-time altimetric ADT and gradients of ADT ($\nabla_y \text{ADT}$) for (a) transect A and (c) transect C. (b,d) Geostrophic velocities perpendicular to the respective glider transects A and C and referenced to the DAC with a horizontal smoothing (moving mean filter) of approx. 15 km (Rossby radius within the region of interest). Positive geostrophic velocities are defined as eastwards (red). Black contours are as in Fig. 4.2. Colour-coding at the top of each panel is defined in Table 4.1 with colors shown in Fig. 4.5. The dashed black lines indicate the location of the Southern Boundary based on the southernmost strong ADT gradient.

2017).

$$PV = -\frac{\partial v}{\partial z} \frac{\partial b}{\partial x} + \frac{\partial v}{\partial x} \frac{\partial b}{\partial z} + f \frac{\partial b}{\partial z}, \quad (4.3)$$

where the first and second term correspond to the horizontal and vertical components of the relative vorticity. The third term corresponds to the stretching term which is proportional to the vertical stratification. The observational PV simplification assumes that the along-stream buoyancy gradients are much weaker than the cross-stream buoyancy gradients. The PV is further considered along potential density surfaces with the same vertical and horizontal gridding as for the calculation of L_{mix} .

The MLS diagnostics show differences between transect A (Fig. 4.9) and transect C (Fig. 4.10). The magnitude of $\nabla_\rho \Theta_m$ across the Southern Boundary is substantially larger in transect A (Fig. 4.9c) than transect C (Fig. 4.9c), where maximum $\nabla_\rho \Theta_m$ aligns with the southern edge of the frontal jet (Fig. 4.8) in both transects. The transects further demonstrate enhanced $\nabla_\rho \Theta_m$ near 56.5°S representing the second, weaker velocity core that marks the boundary between the transition zone and the cold regime further south. The magnitude of Θ_{rms} in both transects (Fig. 4.9b and Fig. 4.10b) is largest along the upper boundary of UCDW and mCDW and reflects fluctuations in the transition to denser water masses below and to the south. The resulting L_{mix} for transect A (Fig. 4.9d) and transect C (Fig. 4.10d) differ by an order of magnitude across the Southern Boundary. Transect A exhibits near zero L_{mix} distinctly confined between 55.5-56°S within the 27.6 kg m⁻³ and 28 kg m⁻³ isopycnals. The region of low L_{mix} coincides with the region of strongest eastward velocities of the frontal jet and southernmost gradients of ADT (Fig. 4.8a,b) as well as strongest magnitudes of $\nabla_\rho \Theta_m$ (Fig. 4.9c). The low magnitude of L_{mix} in transect A is classified as eddy suppressing as eddy diffusivities are proportional to L_{mix} ($\kappa = U_e L_{mix} c_e$, where U_e is the eddy velocity scale, and c_e is the eddy mixing efficiency). These results imply that the ability of water to move across the Southern Boundary is suppressed for transect A, which is consistent with all other transects that have strong density gradients across the Southern Boundary (transects B, D and E; not shown). The stronger density gradients (transects A, B, D and E) are associated with eddies passing the Greenwich Meridian south of the Southern Boundary and influencing its frontal structure and frontal jet. In contrast, transect C exhibits increased L_{mix} of up to 20 km across the Southern Boundary, and the region of lower L_{mix} is not as clearly confined to the region between 55.5-56°S as in transect A, which suggests that the ability of water to flow across the Southern Boundary is increased in transect C.

In general, PV is largest near the surface and decreases with depth towards zero (Figs. 4.9e and 4.10e). Between the 27.5 kg m^{-3} and the 27.7 kg m^{-3} isopycnals in transect A, the PV increases sharply from $PV \ll -8 \cdot 10^{-9} \text{ s}^{-3}$ (south of the Southern Boundary) to $PV \approx -3 \cdot 10^{-9} \text{ s}^{-3}$ (north of the Southern Boundary). The mesoscale eddy influencing the Southern Boundary leads to larger PV (centred around 56°S) coinciding with the eddy's location determined from the temperature maximum (color-coding). In contrast, the PV in transect C does not increase sharply between the 27.5 kg m^{-3} and the 27.7 kg m^{-3} isopycnals. In transect A, at the 27.8 kg m^{-3} isopycnal, which marks the upper boundary of UCDW (centred within the isopycnals of low L_{mix}), the PV also increases sharply across the front from $PV \approx -2.59 \cdot 10^{-9} \text{ s}^{-3}$ (south of the Southern Boundary) to $PV \approx -0.8 \cdot 10^{-9} \text{ s}^{-3}$ (north of the Southern Boundary) in a more pronounced way than in transect C. Similar to the analysis of Bower et al. (1985) for the Gulf Stream, the gradients in PV across the Southern Boundary indicate enhanced barrier-like properties in transect A compared with transect C. Although the PV gradients and low L_{mix} indicate an impedance to cross-frontal mixing, increasing L_{mix} values near the surface suggest that there is still some exchange taking place between regions north and south of the front.

These results indicate that changes in L_{mix} and differing PV gradients in transects A and C are linked to the mesoscale cold-core eddy influencing the density gradients across the Southern Boundary in transect A. As revealed in section 4.3, the cold-core eddy passing the Greenwich Meridian interrupts the temperature transition zone, strengthens the density gradients across the Southern Boundary and amplifies the frontal jet in transect A. The suppressed L_{mix} and more pronounced PV gradients imply that the ability of properties such as heat and freshwater to cross the Southern Boundary is dampened. In contrast, after the cold-core eddy has been advected away to the east, we find no interruption of the temperature transition zone, weakened density gradients and a broader and weakened frontal jet with increased and less confined L_{mix} and less pronounced PV gradients across the front which further suggests the increased ability to exchange water mass properties across the Southern Boundary.

4.4.1 Interannual Variability of Barrier Properties

We have shown that the Southern Boundary's barrier properties (as represented by MLS) are related to the magnitude of the frontal jet. Therefore the strength of the frontal jet, routinely monitored by satellite altimetry, can be used as a proxy to determine the variability of the barrier strength of the Southern

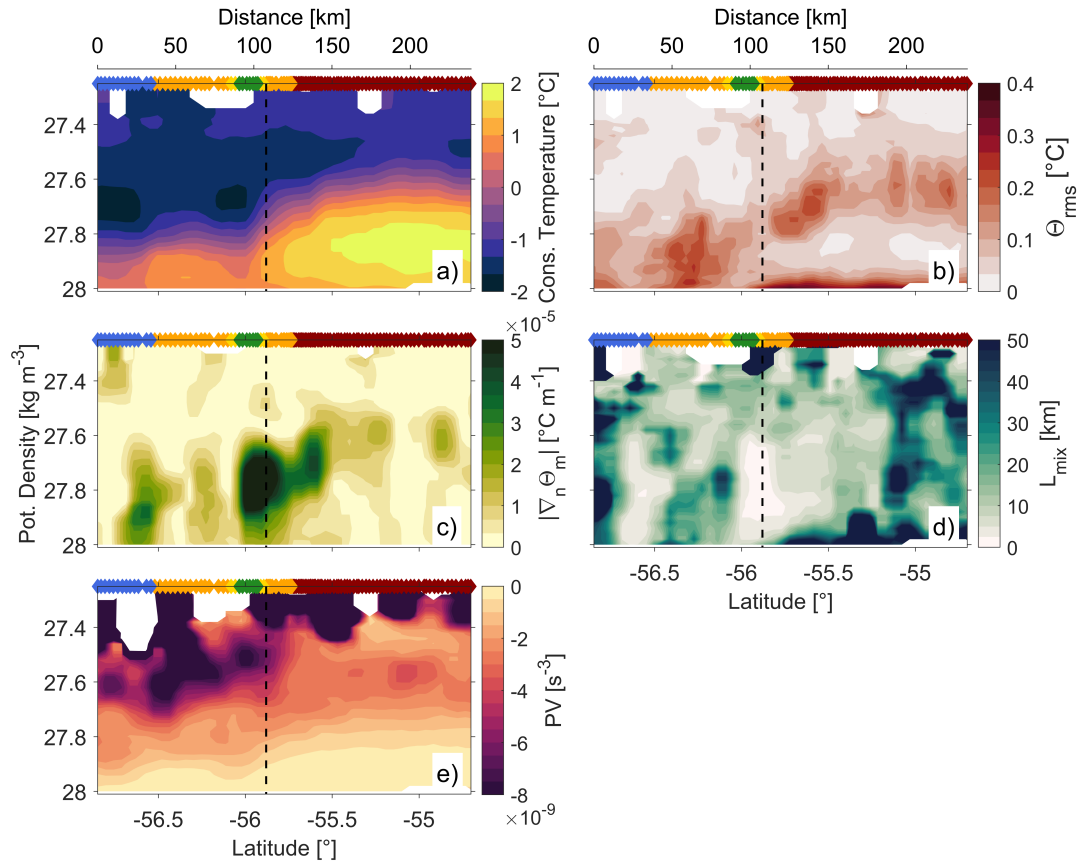


Figure 4.9: (a) The mean temperature field Θ_m , (b) the measure of the temperature fluctuations Θ_{rms} , (c) the gradient of the mean temperature $\nabla_\rho \Theta_m$ along potential density surfaces, (d) the mixing length scales L_{mix} and (e) the potential vorticity (PV) for transect A. All panels are spatially smoothed by a $30 \text{ km} \times 0.08 \text{ kg m}^{-3}$ moving median filter. The dashed black line indicates the location of the Southern Boundary as defined with gradients of ADT as shown in Fig. 4.8. All subfigures a-e are shown in density space with a vertical gridding of 0.02 kg m^{-3} . The color-coded diamonds at the top of each panel describe the segments along transect A as defined in Table 4.1.

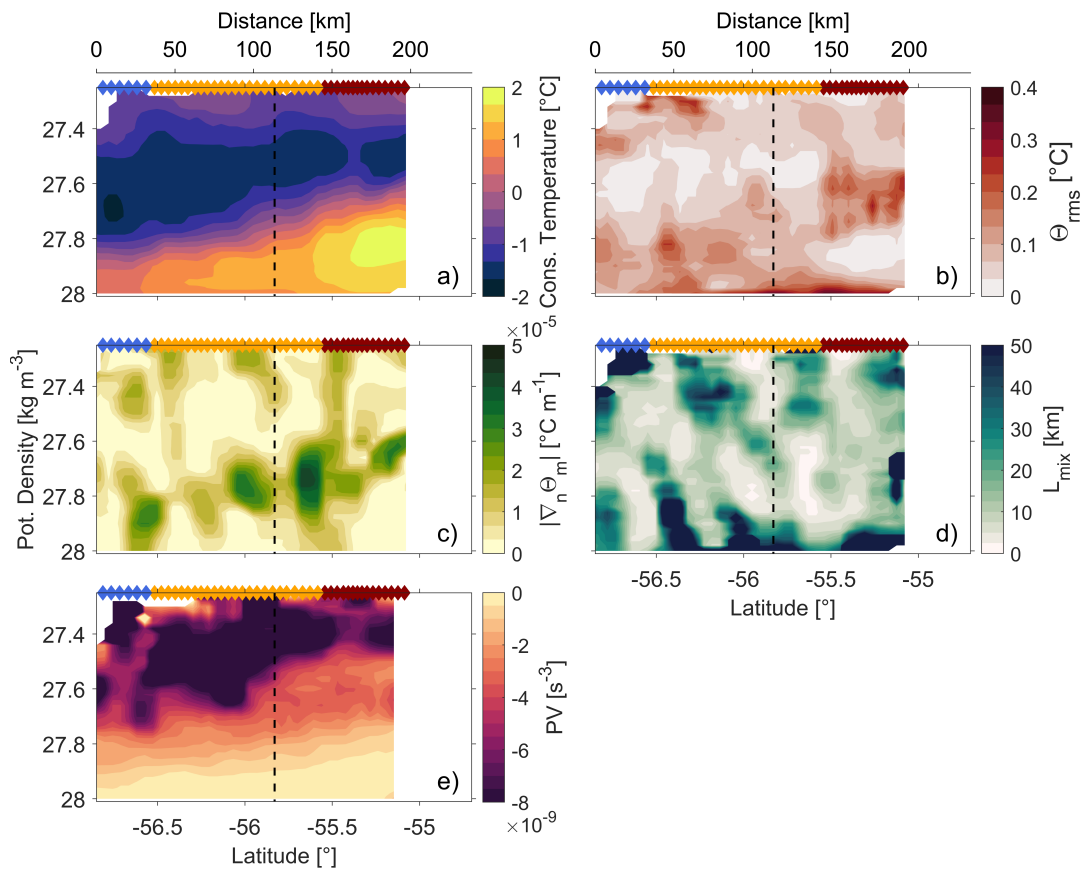


Figure 4.10: As for Fig. 4.9 but for transect C.

Boundary over long time scales (28 years of altimetry data are available). Previous studies have concluded that the use of a fixed ADT contour to define the location of the ACC's fronts is inappropriate over long time scales (such as multiple years), since even if seasonal cycles were removed the long-term warming of ACC waters and associated changes in ADT would not be eliminated (thermal expansion, (Gille, 2014)). Therefore, we estimate the Southern Boundary's location and barrier properties from 1993 to 2020 using surface frontal jet speeds calculated from sea surface slopes (Fig. 4.11) rather than using specific contours of ADT. The chosen speed contour to highlight enhanced frontal jet speed is 14.5 cm s^{-1} , which is determined from the mean frontal jet speed averaged across the latitude band from $54.87\text{-}56.62^\circ\text{S}$ plus twice the standard deviation.

The Southern Boundary's location (determined from the frontal jet) has not migrated south and remains within the $54.87\text{-}56.62^\circ\text{S}$ latitude band throughout the 1993-2020 period (Fig. 4.11). This contrasts with the southward migrating and intensifying westerly winds over the same time period (e.g., Chapman et al., 2020; Gille, 2014; Graham et al., 2012). The average frontal jet speeds across the latitude band (Fig. 4.11d) indicate that the frontal jet speed has accelerated over the past decade ($>14.5 \text{ cm s}^{-1}$, 2012-2020). This increase in frontal jet speeds is associated with stronger gradients in ADT across the Southern Boundary (Fig. 4.11), with an increase in ADT north of the Southern Boundary and no identifiable change in ADT south of the Southern Boundary. These results are consistent with Stewart (2021) and Shi et al. (2021) who demonstrated that the core eastward flow of the ACC has accelerated over the past decade. Stewart (2021) and Shi et al. (2021) further showed that the acceleration in eastward flow is related to the amplification of meridional density gradients in response to upper ocean warming within the ACC, rather than intensifying westerly winds. These results suggest that barrier properties of the Southern Boundary have strengthened over the past decade, associated with strong gradients in PV and density leading to suppressed MLS as shown in section 4.4. We did not find a significant relationship between the changing barrier properties of the Southern Boundary and the northernmost extent of sea ice concentration (Fig. 4.11, white contours). In summary, the potential the exchange of properties such as heat and carbon across the Southern Boundary was dampened over the past decade due to the acceleration of the frontal jet. The continuation of upper ocean warming may further increase meridional ADT gradients resulting in an accelerated frontal jet and strengthened barrier properties of the Southern Boundary in the future.

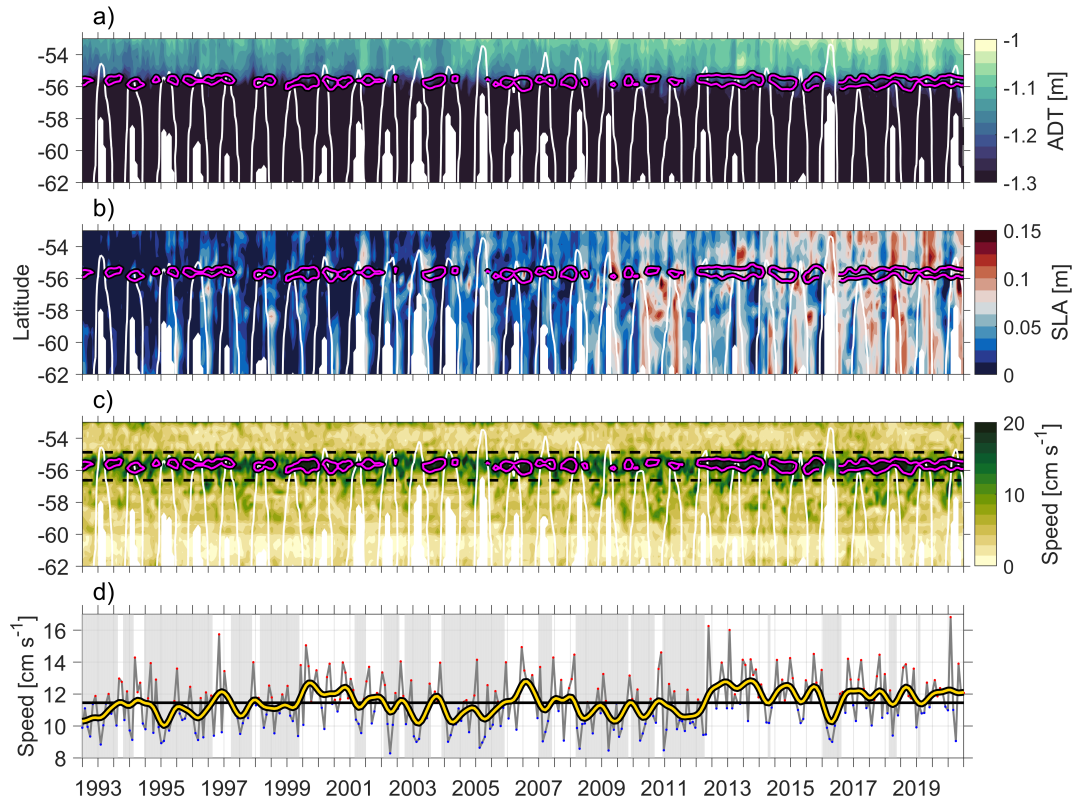


Figure 4.11: Hovmöller diagrams of a meridional transect at the Greenwich Meridian from altimetry showing (a) ADT, (b) SLA and (c) current speed. In panels (a-c), the white contours indicate the OSTIA sea ice concentration (15%) provided by CMEMS (DOI: <https://doi.org/10.48670/moi-00168>). Panel (d) displays the averaged frontal jet speed within the 54.87–56.62°S latitude band (dashed black lines in (c)), with the monthly-average frontal jet speeds (grey) and smoothed (12-month moving median filter) frontal jet speeds (yellow). The shaded areas highlight areas of the smoothed frontal jet speeds that are below the average speed, whereas red and blue dots indicate the above and below average monthly frontal jet speeds. The magenta contours in (a), (b) and (c) highlight periods of enhanced frontal jet speeds ($>14.5 \text{ cm s}^{-1}$).

Satellite altimetry observations and eddy resolving models suggest an intensifying eddy field in response to stronger winds (e.g., Meredith and Hogg, 2006; Hogg et al., 2015; Patara et al., 2016). At the Greenwich Meridian we see an increasing number of warm core eddies (Fig. 4.11b) (and increased EKE, not shown) with increased current speeds south of the Southern Boundary (Fig. 4.11c) from 2009 onwards. Warm core eddies moving south across the front may thus provide a more dominant contribution to the transport of properties across the Southern Boundary in the future as barrier properties strengthen through acceleration.

4.5 Conclusions

In this study we use three months of repeat, high-resolution glider transects over the Antarctic Circumpolar Current's Southern Boundary to assess its variability in location and intensity in terms of lateral gradients and velocities. During the observational time period, the Southern Boundary was located between 55.5-56°S, where the gradients in ADT and the southernmost limit of UCDW coincided. The estimated location is consistent with previously estimated locations of the Southern Boundary (e.g., Billany et al., 2010). Most glider transects (except transect C) are characterised by strong density gradients across the front associated with a strong frontal jet ($\approx 80\text{cm s}^{-1}$), whereas transect C demonstrated weaker density gradients associated with a weaker, broader frontal jet ($\approx 60\text{cm s}^{-1}$).

The glider transects and SLA revealed that mesoscale cold-core eddies influence the Southern Boundary's frontal structure by disrupting the temperature transition zone, enforcing stronger density gradients across the front and amplifying the frontal jet. These findings are consistent with Williams et al. (e.g., 2007) who demonstrated that eddies impact lateral density gradients across the ACC that can accelerate or decelerate the mean flow. We find cold-core eddies are present in all transects that have a disrupted transition zone and strong density gradients (example transect A). In contrast, we show that the cold-core eddy in transect A is advected away eastward before transect C is occupied, which then does not cross the cold-core eddy and presents weaker density gradients and a weaker, broader frontal jet. The highly energetic eddy field within the ACC varies rapidly and locally around the Antarctic continent and thus more observations are needed to address the impacts of mesoscale eddies on the Southern Boundary's frontal structure in a circumpolar fashion. Future investigations with a focus on regions where the influences of mesoscale eddies on the Southern Boundary's frontal structure are more or less significant may improve estimations of its barrier properties.

Low L_{mix} and more pronounced PV gradients at the Southern Boundary are found at the upper boundary of UCDW (example transect A, Fig. 4.9 d) associated with strong density gradients and an amplified frontal jet. These characteristics suggest that the exchange of properties across the Southern Boundary is dampened. Thus, it is implied that strengthened barrier properties are a result of cold-core eddies enforcing stronger density gradients across the Southern Boundary. In contrast, increased values of L_{mix} of up to 20 km

and less pronounced PV gradients across the Southern Boundary (example transect C, Fig. 4.10 d) are found when no cold-core eddy is observed to influence the Southern Boundary's frontal structure (weaker density gradients, weaker frontal jet). These findings emphasize that locally changing mesoscale structures can significantly impact the Southern Boundary's barrier properties and thus modulate cross-frontal exchange of properties such as heat and carbon. The cross-frontal exchange of properties is specifically relevant to regions where the Southern Boundary is located near the continental shelf break, such as in the West Antarctic Sector, as the amount of heat accessing the continental shelf is modulated by the front's barrier properties.

Additionally, we have shown that the linkage between MLS and the intensity of the frontal jet of the Southern Boundary is important to establish the Southern Boundary's barrier properties over long time periods (multiple years). Increased ADT gradients across the Southern Boundary, as a result of increased ADT north of the front (Fig. 4.11a), confirm amplified frontal jet speeds from 2009 onwards. This is consistent with the amplification of the ACC's eastward flow demonstrated by Shi et al. (2021) and Stewart (2021). Based on our results, strengthened density gradients across the Southern Boundary and thus an intensified frontal jet are indicators for dampened cross-frontal exchange and strengthened barrier properties. Thus, we suggest that the poleward heat transfer through mixing across the Southern Boundary at the Greenwich Meridian has likely decreased over the last decade, whereas the intensified eddy field and generation of warm-core eddies that cross the Southern Boundary in response to intensifying westerly winds likely provided an increased contribution to poleward heat transfer. As these processes vary locally and temporarily, our results demonstrate that more investigations of the Southern Boundary's frontal jet intensity and barrier properties are needed to understand and estimate the cross-frontal exchange around the Antarctic continent in more detail.

Chapter 5

Conclusions and Future Work

5.1 Summary

The Southern Boundary describes the southernmost barrier of the ACC that separates warm ACC waters from colder waters further south. In comparison to the major ACC fronts, the Southern Boundary is poorly investigated due to the lack of long-term and high-resolution observations. However, the spatial and temporal variability of the Southern Boundary, the intensity of its frontal jet and the cross-frontal mixing of properties (e.g., heat) can have large scale impacts on sea ice extent, penetration of warm waters onto the continental shelf and resulting ice shelf melt. The barrier properties of the Southern Boundary are particularly important for areas where the Southern Boundary is located closest to the continental shelf break (e.g., the West Antarctic Sector). Thus, additional investigations of processes, mechanisms and conditions that influence the Southern Boundary's variability are essential to understand future climate scenarios. This thesis investigated and analysed dynamical processes and mechanisms that drive and influence the Southern Boundary around Antarctica. Key sites considered in this thesis are located in the Bellingshausen and Weddell seas. The results provided are an important contribution to improve our understanding of the Southern Boundary and its influence on the southward extent of warm waters onto the Bellingshausen Sea continental shelf (Chapter 2). Furthermore, the processes that dominate the temperature variability on the Bellingshausen Sea continental shelf are investigated in great detail and provide further insight into processes and conditions that favour long-term warming and cooling of water masses in the southern Bellingshausen Sea (Chapter 3). Finally, the processes that impact the frontal structure of the Southern Boundary and the mixing of properties across the Southern Boundary at the Greenwich Meridian, Weddell Sea, are investigated (Chapter 4).

5.1.1 The Bellingshausen Sea

This thesis presented results from two studies in the Bellingshausen Sea, where the Southern Boundary is located close to the continental shelf break and slope. The absence of the ASC in the central and eastern Bellingshausen Sea provides a direct connection between the Southern Boundary and colder waters on the continental shelf. The first study in the Bellingshausen Sea (Chapter 2) has demonstrated the frontal structure and the location of the Southern Boundary above the shelf break and slope and partly on the continental shelf in the eastern Bellingshausen Sea with observed hydrographic transects. However, due to the lack of observations in repeated locations it became apparent that investigations focusing on the variability of the Southern Boundary require long-term model data. Thus, additional data were extracted from GLORYS for the time period from 2000 to 2018. One of the key questions, which had been given very little attention in the past, was whether the extent of warm waters on the continental shelf is impacted by the spatial and temporal variability of the Southern Boundary and more specifically whether the Southern Boundary's distance to the shelf break impacts the warm water extent on the continental shelf. The results of this study demonstrated that the penetration of warm waters in direct connection to the shelf break is closely related to the distance of the Southern Boundary to the shelf break specifically in the eastern Bellingshausen Sea. Furthermore, the Southern Boundary presented a weak seasonal, but strong interannual variability with respect to its distance to the shelf break. Our results also demonstrated that the southward extent of warm waters on the continental shelf does not necessarily imply that the southern Bellingshausen Sea is affected by the penetration of warm waters onto the continental shelf near the shelf break. These results further raised the question which processes and mechanisms influence the temperature variability on the southern Bellingshausen Sea continental shelf.

Over the past decade, many studies have investigated mechanisms that are responsible for the penetration of warm water onto the continental shelf and specifically its pathway through troughs towards ice shelf cavities in the West Antarctic sector. However, some modelling studies emphasised the importance of sea ice concentration, air-sea heat flux and cold water formation within coastal polynyas as an important driver for the modification of ocean conditions (St-Laurent et al., 2015) and ice shelf stability (Khazendar et al., 2013). In Chapter 3, GLORYS was used to identify factors enhancing access of warm Circumpolar Deep Water into the Eltanin and Latady bays on the southern Bellingshausen Sea continental shelf from 1993 to 2018. Annual means of

potential temperature from 300 m to the seabed revealed the interannual variability and allowed a separation into warm and cold regimes. The Amundsen Sea Low was more intense and extended further east during the warm regime than the cold regime. In the warm regime, a wind-induced reduction of sea ice concentration near the coast increased surface heat loss, convection, and formation of cold dense water in winter, associated with a decrease in heat content of the southern Bellingshausen Sea over time and a net northward heat transport. In contrast, in the cold regime, increased sea ice concentration reduced the surface heat loss and thus formation of cold, dense water. Combined with an increase in heat content over time and a net southward heat transport, this resulted in a warming of the southern Bellingshausen Sea. This suggested that the deep-water temperature in the southern Bellingshausen Sea is maintained by a combination of shelf break heat transport and surface heat fluxes. Our results showed that the variability of surface heat fluxes is related to the variability of the Amundsen Sea Low and its influence on sea ice extent and local formation of cold, dense water in winter.

The majority of observational and modelling studies have focused on the Amundsen Sea and WAP, where detailed investigations (observations and simulations) improved our understanding of local dynamical processes and mechanisms that enable the transport of warm water onto the continental shelf and towards ice shelf cavities (e.g. Schmidtko et al., 2014). Our results contribute to this research by revealing important aspects of the local dynamical processes that influence the temperature variability on the Bellingshausen Sea continental shelf. The separation of warm and cold regimes in the Bellingshausen Sea was accomplished for the first time and provided crucial characteristics that favour the long-term warming and cooling of temperatures on the continental shelf. Additionally, our results show that warm and cold years in the Bellingshausen Sea only partly agree with observations (Jenkins et al., 2018; Webber et al., 2017) and simulations (Dutrieux et al., 2014; Dotto et al., 2019) of warm and cold years in the adjacent Amundsen Sea, suggesting a different variability pattern. We further identified a negative feedback loop on the Bellingshausen Sea continental shelf (warming in the cold regime, cooling in the warm regime) which is opposite to the feedback loop demonstrated on the WAP (Venables and Meredith, 2014).

The research in the Bellingshausen Sea revealed many future questions. One of these is related to the wind field above the Bellingshausen Sea and its influences on the shelf circulation, sea ice concentration and cold water formation. Climate model simulations predict that the ASL is likely to migrate poleward

and eastward within the remainder of this century (Hosking et al., 2016). This would cause a southward migration of eastward winds along the shelf break and slope (Holland et al., 2019). Furthermore, studies have shown that eastward winds above the ACC have intensified and shifted southward as a result of climate change (positive Southern Annular Mode; e.g. Thompson et al., 2011). This change in atmospheric circulation can further intensify eastward wind speeds along the shelf break and slope, which would increase the offshore Ekman transport and result in even lower SSH on the Bellingshausen Sea continental shelf. Stronger eastward winds and stronger SSH gradients above the shelf break and slope would further result in an amplification of the frontal jet associated with the Southern Boundary. An amplification of the frontal jet would also impact the barrier properties of the Southern Boundary. Our results in Chapter 4 have demonstrated a strengthening of barrier properties and thus a decrease in mixing across the Southern Boundary in association with an amplified frontal jet and stronger density gradients across the Southern Boundary region. Conversely, studies have shown that the southward migrating and intensifying eastward winds cause an enhancement in the eddy kinetic energy field (Meredith and Hogg, 2006; Hogg et al., 2015; Patara et al., 2016) and therefore the transport of heat towards the Bellingshausen Sea continental shelf could be increased through eddies crossing the Southern Boundary. Additionally, the predicted southward migration of the ASL can also cause a weakening of northward winds in the southern Bellingshausen Sea as the wind field associated with the ASL would move further south. This southward shift in the ASL wind field can result in an increase in sea ice concentrations near the coast and thus a reduction in heat loss to the atmosphere which can decrease convection and cold water formation. These characteristics would suggest a warming of the southern Bellingshausen Sea and enhanced ice shelf melt in the future.

5.1.2 The Weddell Sea

The third study presented in this thesis demonstrated results with respect to the Southern Boundary's frontal structure and its short-term (≈ 14 days) variability at the Greenwich Meridian in the Weddell Sea. For this study, a total of five repeated and highly resolved hydrographic glider transects and AVISO satellite altimetry have been used to identify processes and mechanisms that impact the Southern Boundary's frontal structure and influence the mixing of water mass properties across the Southern Boundary. Our investigations showed that a cyclonic eddy, located in close proximity to the south of the Southern Boundary, interacted with the Southern Boundary and impacted its

frontal structure. Our results demonstrated that the interaction of the cyclonic eddy with the Southern Boundary strengthened the Southern Boundary's density gradients. Geostrophic velocities demonstrated a narrow and strong frontal jet (≈ 50 km wide with velocities of 80 cm s^{-1}) associated with the Southern Boundary. Shortly after the eddy crossed the Greenwich Meridian, a weakening of the density gradients across the Southern Boundary was identified. This resulted in a broadening and weakening of the frontal jet (≈ 75 km wide with velocities of 60 cm s^{-1}). Our results further demonstrated near zero mixing length scales across the frontal jet while the eddy interacted with the Southern Boundary that increased to nearly 25 km after the eddy crossed the Greenwich Meridian. These results highlighted important characteristics with respect to the Southern Boundary's barrier properties that dampen or amplify the mixing of properties across it. Stronger barrier properties are associated with stronger density gradients across the Southern Boundary and a stronger frontal jet and imply reduced mixing of properties across the Southern Boundary.

This study raised a particular question concerning the definition of the Southern Boundary. Many studies have focused on defining the different fronts of the ACC to study their seasonal and interannual variability, frontal structure, extent and location. These definitions were based on water mass properties (Orsi et al., 1995; Kim and Orsi, 2014), gradients of SSH (Sokolov and Rintoul, 2007; Sokolov and Rintoul, 2009a; Sokolov and Rintoul, 2009b; Billany et al., 2010) and mean transport positions (Gille, 2014; Gille et al., 2016). In most cases, the Southern Boundary's location was limited to a single contour varying in space and time. One major point of discussion over the past decade was whether the fronts of the ACC have shifted south in response to southward migrating and intensifying eastward winds. The large-scale southward shift of at least the three major ACC fronts has been identified using fixed SSH contours for each of the fronts (Sokolov and Rintoul, 2009a; Sokolov and Rintoul, 2009b) and also Billany et al. (2010) observed the southward shift of ACC fronts including the Southern Boundary using the SSH approach. Gille (2014) questioned this southward shift by calculating displacements of transport-weighted indices of mean ACC positions and demonstrated strong temporal and spatial variability of the ACC fronts, but no southward trend. Yamazaki et al. (2021) further demonstrated a substantial southward shift of the Southern Boundary of more than 50 km using water mass properties from CTD stations, historical Argo floats and model simulations, which was argued to likely be controlled by continental slope topography. Our results using a fixed contour to define the Southern Boundary's location demonstrated an unrealistic southward shift

of 195 km southward from 1993 to 2020. However, the location of the frontal jet associated with the Southern Boundary remained unchanged. This further highlighted that this unrealistic southward shift is mainly a reflection of long-term warming of ACC waters. Thus, even if seasonal changes were removed, the long-term trend would still influence the Southern Boundary's location deduced from a SSH contour due to thermal expansion. As a result, it is now broadly accepted that mean ACC positions have not shifted south in response to recent climate change (Chapman et al., 2020). This statement further implies that the definitions of the Southern Boundary using either water mass properties or a fixed SSH contour are inappropriate to investigate its long-term spatial and temporal variability. Furthermore, the question remains whether it even is appropriate to define the Southern Boundary as a single contour or whether it would be more accurate to define the Southern Boundary's location based on the position and extent of the frontal jet from the SSH gradients. The frontal jets of the ACC were identified to be somewhat 'resistant' in location in response to southward migrating eastward winds (Chapman et al., 2020). Based on this suggested approach, the Southern Boundary would rather describe the transition zone between warm ACC waters and colder waters further south that could be observed on a global scale.

The results of this study further revealed that the frontal jet has amplified over the past decade. Stewart (2021) and Shi et al. (2021) demonstrated that the core eastward flow of the ACC at 52°S has accelerated over the past decade as a result of intensifying latitudinal density gradients in response to upper ocean warming. The intensified frontal jet that has been identified over the same time period confirms these findings for the Southern Boundary. In addition, satellite observations and simulations from previous studies suggested that the long-term intensification of eastward winds energised the eddy field within the ACC (Meredith and Hogg, 2006; Hogg et al., 2015; Patara et al., 2016). Our results have indicated an increasing number of warm core eddies at the Greenwich Meridian from 2009 onwards. An essential question that remains is therefore how the Southern Boundary's barrier properties are affected by the energetic eddy field, as an increased frontal jet would imply the strengthening of barrier properties and a decrease in mixing across the Southern Boundary, whereas more warm core eddies shed by the ACC could increase the southward heat transport. This is not only an important future question for the Weddell Sea but in particular for areas where the Southern Boundary is located much closer to the continental shelf break. An example is the West Antarctic sector, where increased southward heat transport could have substantial consequences for the

melting of ice shelves and resulting sea level rise.

5.2 Future Work

There are a number of suggestions how research and future studies can be developed further from the results demonstrated in this thesis and key questions that arose from our research. In general, the lack of long-term observations in the Southern Ocean, and particularly in the areas on the continental shelf that are difficult to access, limits our ability to investigate processes and conditions that favour warming and cooling of temperatures on the continental shelf of Antarctica.

In the Bellingshausen Sea, GLORYS has greatly helped to identify parameters that indicate warming and cooling of temperatures on the continental shelf that can be observed in more detail in the future. For example, bottom temperatures in Eltanin Bay near the coast in the southern Bellingshausen Sea (coastal polynya region) provided a strong indication of cold water formation and warming/cooling tendencies. Note that bottom temperatures may not only be an indicator for warming and cooling tendencies on the Bellingshausen Sea continental shelf, but also in other coastal polynya regions such as in the Amundsen and Ross seas and along the coastline of East Antarctica. Therefore, bottom moorings, which measure temperature and salinity, placed in coastal polynya regions and close to ice shelf cavities (Fig. 5.1, red dots) would greatly extend this research and would provide the advantage of the moorings being less vulnerable to sea ice and icebergs than a full-depth mooring. Observations of this type would not only be essential to confirm key characteristics for warm and cold regimes identified in GLORYS for the Bellingshausen Sea, but would also help to improve reanalysis products and reduce biases.

Another parameter that showed strong correlations to the temperature variability on the Bellingshausen Sea continental shelf in GLORYS is SSH. SSH variability can be observed via satellite altimetry, where lower SSH in the central Bellingshausen Sea shelf indicates cold years and warming tendencies due to the negative feedback loop found in GLORYS. Furthermore, the SSH signal is fairly large (> 200 km) in GLORYS, which would suggest that SSH from satellite altimetry would be able to capture the SSH signal even if the resolution of SSH from satellite altimetry is not currently as high as the SSH in GLORYS. Conversely, GLORYS also had limitations with respect to continental shelf bathymetry, ice shelf cavities and ice shelf melt that can substantially

impact the southward heat transport towards ice shelf cavities, water mass stratification and cold water formation. Reducing these limitations by implementing more recent bathymetry, ice shelf cavities and ice shelf melt in GLORYS would greatly help to improve estimations of the impact of southward heat transport on ice shelf melt rates over several decades.

Investigations with respect to the Southern Boundary could be developed further and with a more circumpolar approach, predominantly in locations where the Southern Boundary is close to the shelf break (Fig. 5.1, Southern Boundary contour marked in red). We also suggest to devote more attention to the frontal jet associated with the Southern Boundary in the future, where a particular focus could also be given to a potential southward shift of the Southern Boundary in response to southward migrating and intensifying eastward winds. Yamazaki et al. (2021) observed a southward shift of the Southern Boundary in East Antarctica using water mass properties, but no evidence was provided that the frontal jet has shifted south. Our investigations on the long-term variability of the Southern Boundary in the Bellingshausen Sea (Chapter 2) further indicated that in some years the water masses of the Southern Boundary moved onto the continental shelf, whereas the location of its frontal jet remained unchanged. Furthermore, our results did not indicate a southward shift of the frontal jet at the Greenwich Meridian over the past decades (Chapter 4), which also implies that the Southern Boundary has not shifted south in response to southward migrating winds. For future research, we suggest redefining the Southern Boundary based on a range of meridional SSH gradients to achieve a definition for the Southern Boundary's location that is least impacted by long-term warming. Daily locations of the frontal jet can be observed via satellite altimetry products (e.g., AVISO). This approach would allow investigation of the long-term variability of the southernmost barrier to mixing (the frontal jet). Collecting information on the spatial and temporal variability of the Southern Boundary on a circumpolar scale will help to identify if and where the Southern Boundary and its frontal jet have shifted south.

Future research with respect to the intensity of the frontal jet is crucial for estimations of the mixing of properties across the Southern Boundary. Studies have suggested an intensification of the ACC in response to upper ocean warming and increased latitudinal density gradients (Stewart, 2021; Shi et al., 2021) and our results indicated an amplification of the frontal jet at the Greenwich Meridian as well. However, the question remains whether the amplification of the frontal jet occurs on a circumpolar scale or whether specific areas demonstrate an unchanged or weakened frontal jet, which would indicate increased

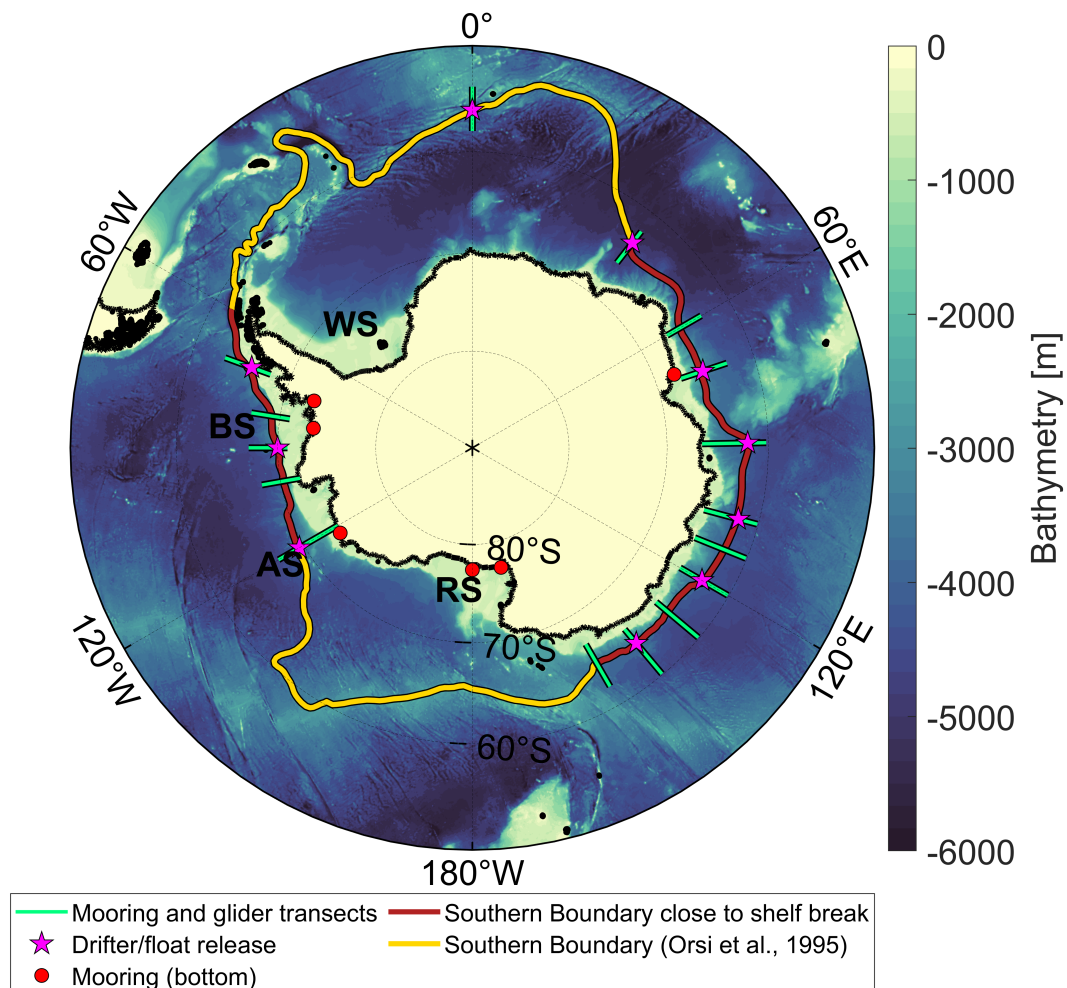


Figure 5.1: Map of the Southern Ocean with suggested observational platforms and placement locations for future research. The contour of the Southern Boundary (yellow line) is based on the definition from Orsi et al. (1995) with areas where the Southern Boundary is located closest to the continental shelf break marked in red. The bathymetry is based on Schaffer et al., 2019. The acronyms are: Weddell Sea (WS), Ross Sea (RS), Amundsen Sea (AS), Bellingshausen Sea (BS) and West Antarctic Peninsula (WAP).

mixing across the Southern Boundary. Observations of the Southern Boundary and its frontal jet via satellite altimetry (e.g. AVISO), closely-spaced mooring transects and glider campaigns in various locations around Antarctica would greatly expand the investigations of the long- and short-term variability of the frontal jet intensity and of the vertical structure of the Southern Boundary. A focus here could be on areas where the Southern Boundary is closest to the shelf break (such as in the West Antarctic Sector and along the coast of East Antarctica (Fig. 5.1)), which would provide observations comparable to observations from previous studies (Thompson et al., 2020; Yamazaki et al., 2021).

Studies have demonstrated an intensified eddy field within the ACC in response to southward migrating and intensifying eastward winds (Meredith and Hogg, 2006; Hogg et al., 2015; Patara et al., 2016). Our results at the Greenwich Meridian in particular have demonstrated the substantial impacts that eddies can have on the Southern Boundary's frontal structure and mixing across the front. These results also indicated an increasing number of warm core eddies crossing the Southern Boundary in recent years. However, the Southern Boundary at the Greenwich Meridian is located in a region that is fairly isolated from downstream perturbations at Drake Passage to the west and far enough to the east not to be strongly influenced by the Agulhas Current and its retroflexion. Thus, studies of regions that are dominated by downstream perturbations such as within Drake Passage or around islands and plateaus (e.g. Kerguelen Plateau) are essential to understand the Southern Boundary's barrier properties around Antarctica. The deployment of surface drifters and floats (Fig. 5.1, magenta stars) around these regions in simulations and in the real ocean would provide trajectories from which estimates of eddy diffusivities (Lagrangian single and pair particle statistics) can be calculated (e.g. Griesel et al., 2010). Eddy diffusivities are an important indicator of a more energised eddy field in both observations and simulations and can further be used to improve parameterisations in future simulations of the Southern Ocean.

5.3 Final Considerations

In the West Antarctic Sector (predominantly the Amundsen Sea and WAP) much attention has been given to shelf break processes that favour the penetration of warm CDW onto the continental shelf and its pathway towards ice shelf cavities. In comparison with the Amundsen Sea and the WAP, the Bellingshausen Sea was fairly understudied due to the lack of long-term observations in such an inaccessible region. Our results from GLORYS filled in some of the

scientific gaps with respect to long-term temperature variability, warm and cold regimes and cold water formation on the Bellingshausen Sea continental shelf in response to changes of the ASL. The methods applied in this study are applicable to other marginal seas around Antarctica, such as the Weddell, Ross and Amundsen Seas, the continental shelf of East Antarctica and the WAP. Results from those future studies in other marginal seas could help understanding the temperature variability on the continental shelf and different processes involved. Furthermore, processes and indicators for the temperature variability in these future studies could help to motivate the need for additional observations in specifically targeted areas, such as within coastal polynyas.

Many previous studies have analysed and reported the long- and short term variability, frontal structures and mixing across the major ACC fronts. However, very little focus has been given to the Southern Boundary, due to its relatively weak surface signal in comparison to the major ACC fronts. Our research has clearly highlighted the scientific gaps and discrepancies with respect to the Southern Boundary and specifically its definition. We raised awareness that the frontal jet associated with the Southern Boundary has been neglected in the past, and demonstrated its importance in providing the southernmost barrier to meridional mixing of properties such as heat. Specifically in regions where the Southern Boundary is located close to the shelf break, detailed future investigations are crucial for understanding processes in a changing climate that impact the penetration of warm waters onto the continental shelf around Antarctica. Many future research questions arose from our research on the Southern Boundary, which greatly contributed to identifying gaps in knowledge and ideas for future studies.

Appendix A

The supporting information includes four figures to accompany Chapter 3 'Wind-induced variability on the Bellingshausen Sea continental shelf'. The following description of figures and captions is implemented as in the supporting information of Chapter 3 submitted to *Journal of Geophysical Research: Oceans*. The additional figures are used to highlight that wind conditions in the warm regime are responsible for reduced sea ice concentration in the southern Bellingshausen Sea as discussed in Chapter 3. In the warm regime, sea ice is blown away more rapidly from the coast to the north-west. The reduction in sea ice concentration results in increased heat loss to the atmosphere and thus an increase in convection and the formation of cold, dense water in winter.

Fig. A1 demonstrates the summer and winter long-term mean of wind speeds extracted from ERA5 from 1993 to 2018 and highlights the summer and winter conditions of the wind field above the Bellingshausen Sea. Fig. A3 shows the anomalies of winter wind speed, zonal and meridional wind components for warm and cold regimes as defined in Chapter 3. The anomaly calculations are based on the winter long-term mean as shown in in Fig. A1b and are used to highlight the strong seasonality of the wind fields above the Bellingshausen Sea and to highlight the differences between warm and cold regimes as discussed in 3. Fig. A2 shows the anomalies of summer wind speed, zonal and meridional wind components for warm and cold regimes as defined in Chapter 3. The anomaly calculations are based on the summer long-term mean as shown in in Fig. A1a and are used to highlight the strong seasonality of the wind fields above the Bellingshausen Sea and to highlight the differences between warm and cold regimes as discussed in 3.

Fig. A4 presents the summer and winter anomalies of sea ice concentration for the warm and cold regimes as defined in Chapter 3. The anomalies are calculated using the long-term mean summer and winter sea ice concentration (Fig. 3.2). The sea ice concentration anomalies are used to demonstrate the strong seasonality in sea ice concentration and the differences in seasonality during the warm and cold regimes as discussed in Chapter 3.

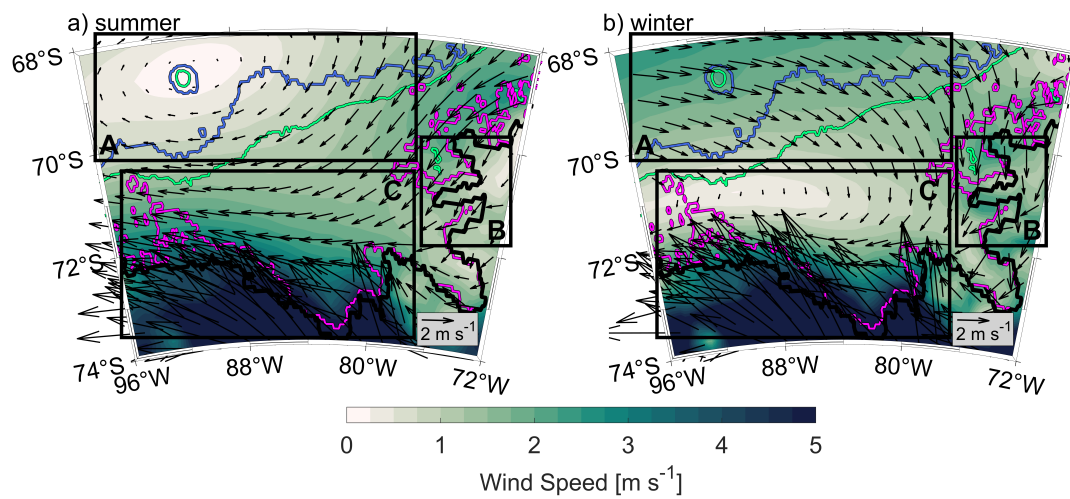


Figure A1: (a) Summer and (b) winter long-term mean of wind speeds from 1993 to 2018, extracted from ERA5 in the Bellingshausen Sea region. Velocity arrows of the summer and winter long-term means are superimposed. Isobaths are coloured as in Fig. 3.2 in Chapter 3.

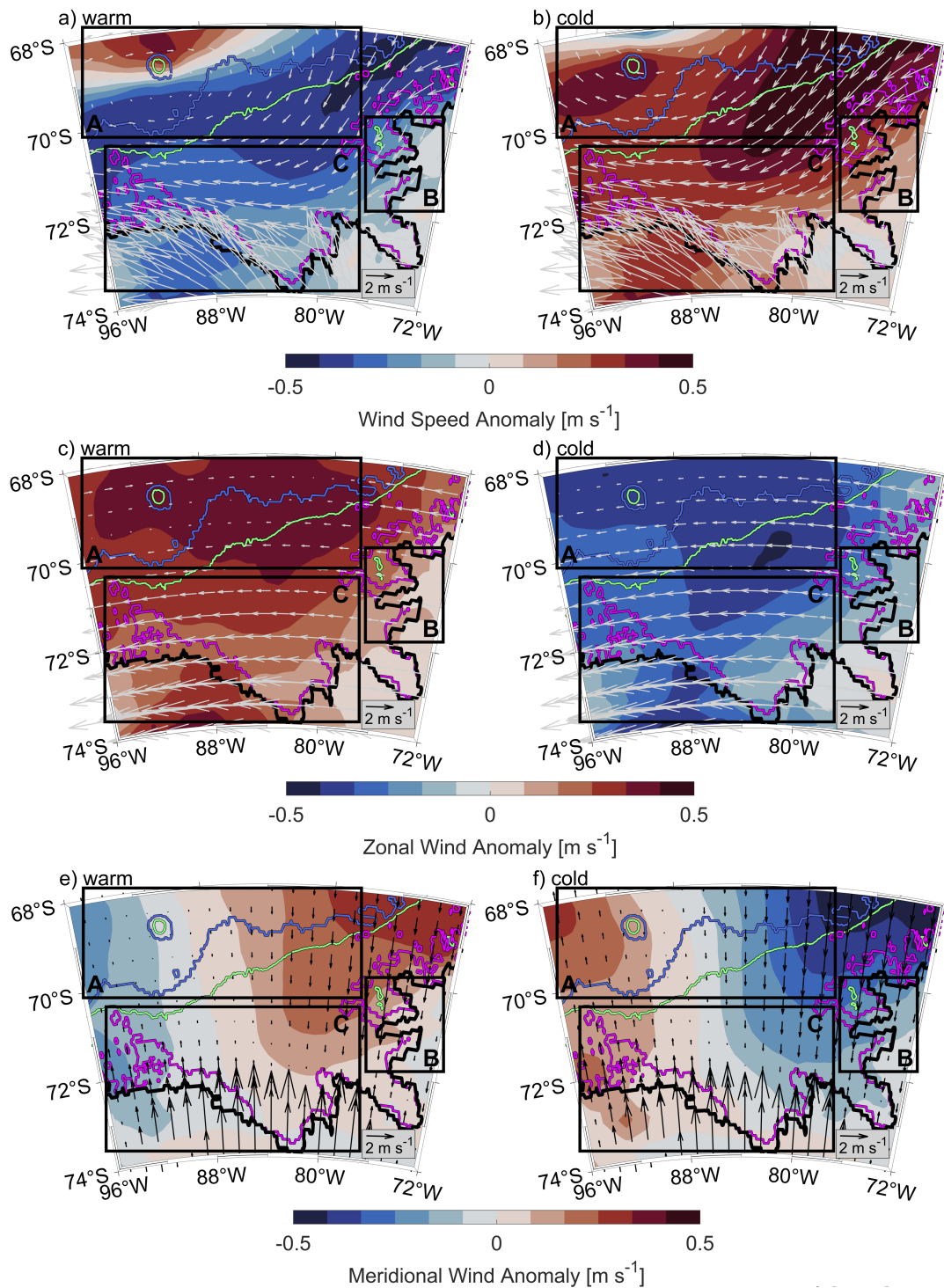


Figure A2: Anomalies from the summer long-term mean of (a,b) wind speed, (c,d) zonal wind component and (e,f) meridional wind component for the warm (a,c,e) and cold (b,d,f) regimes. The anomalies are calculated from summer long-term means as shown in Fig. A1. Composite wind velocity vectors for the warm and cold regimes are superimposed. Boxes A, B and C highlight areas discussed in Chapter 3. Isobaths are coloured as in Fig. 3.2 in Chapter 3.

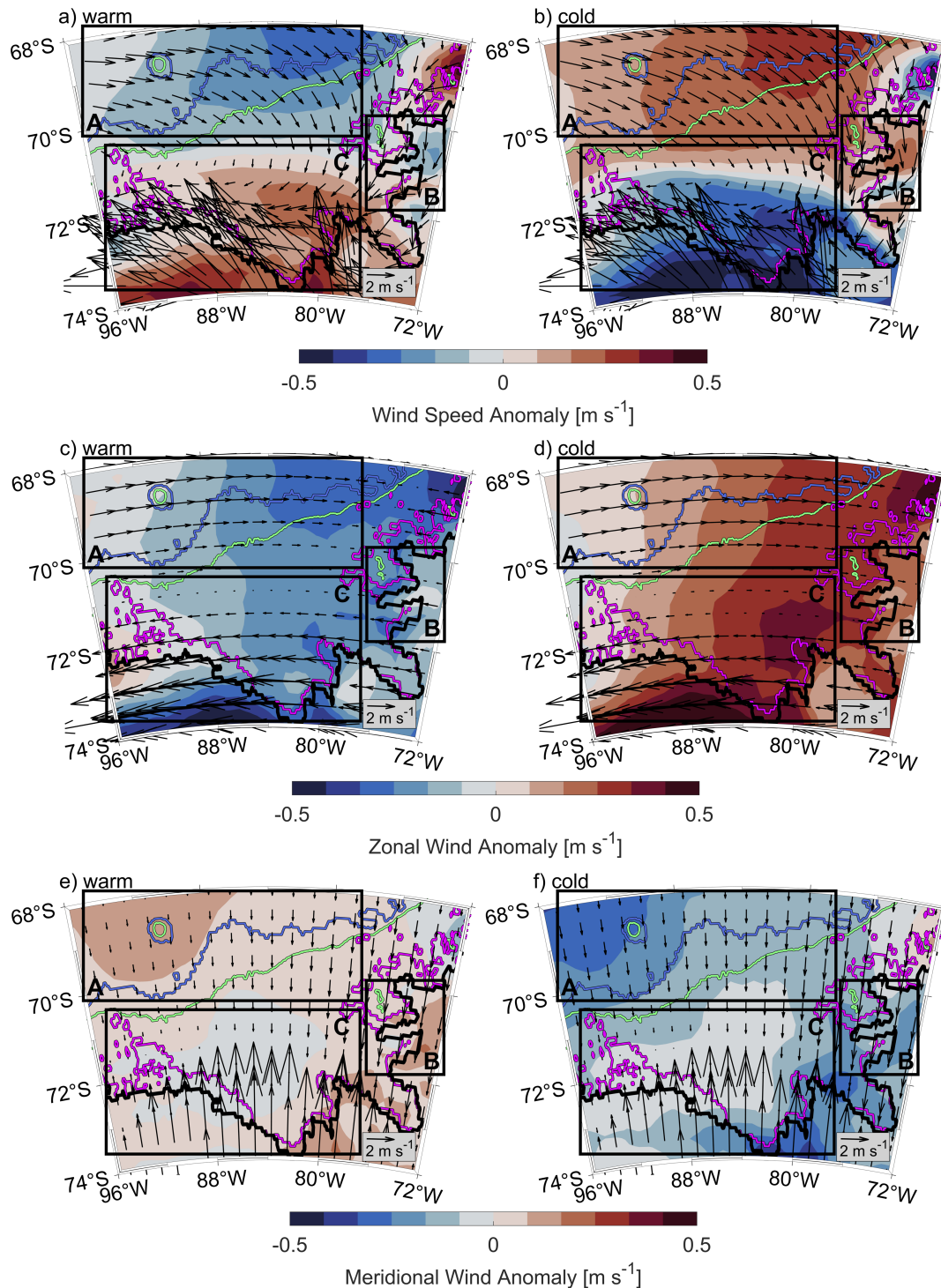


Figure A3: Anomalies from the winter long-term mean of (a,b) wind speed, (c,d) zonal wind component and (e,f) meridional wind component for the warm (a,c,e) and cold (b,d,f) regimes. The anomalies are calculated from winter long-term means as shown in Fig. A1. Composite wind velocity vectors for the warm and cold regimes are superimposed. Boxes A, B and C highlight areas discussed in the text (Chapter 3). Isobaths are coloured as in Fig. 3.2 in Chapter 3.

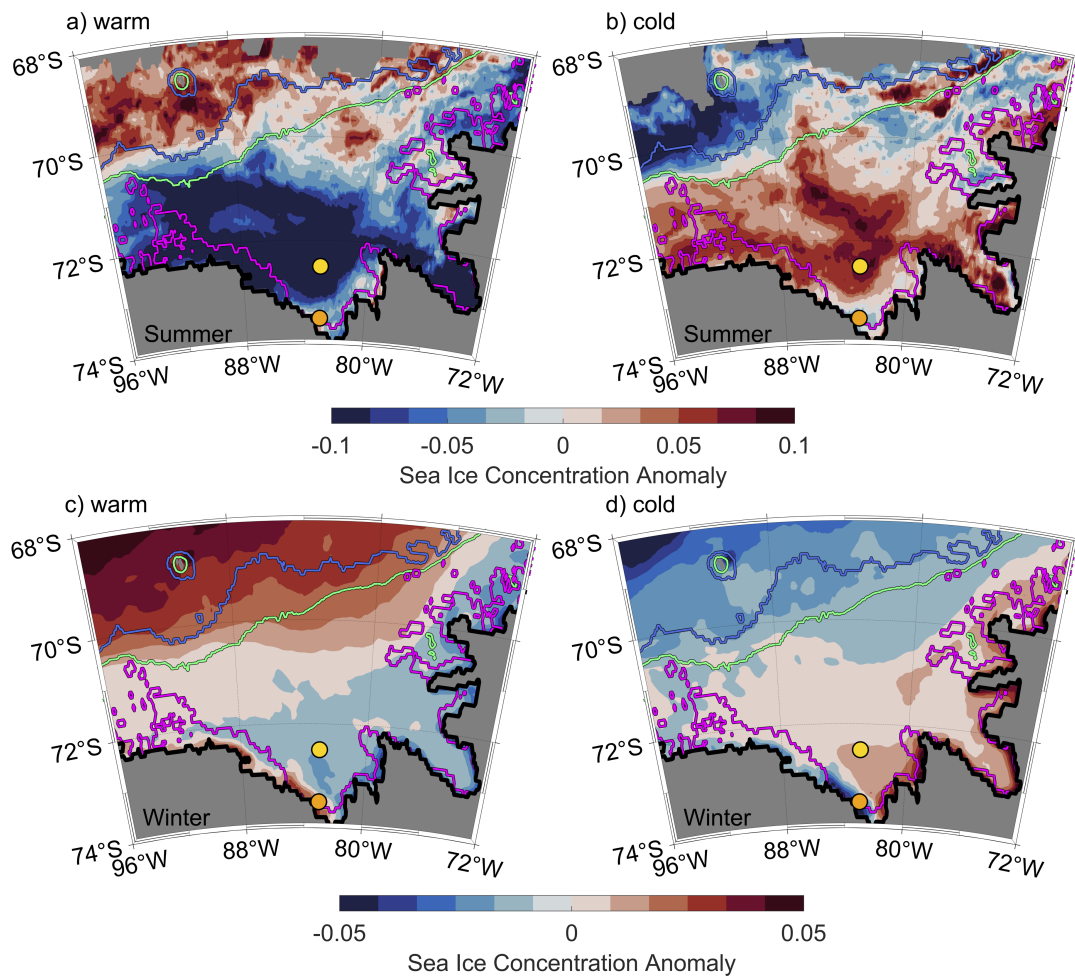


Figure A4: Sea ice anomalies for the summer and winter long-term means for (a,c) the warm regime and (b,d) the cold regime. The anomalies are calculated with summer and winter long-term means of sea ice concentration as shown in Fig. 3.2e,f in Chapter 3. Isobaths are coloured as in Fig. 3.2 in Chapter 3.

References

- Armitage, T. W. K., R. Kwok, A. F. Thompson, and G. Cunningham (2018). “Dynamic Topography and Sea Level Anomalies of the Southern Ocean: Variability and Teleconnections”. In: *Journal of Geophysical Research: Oceans* 123.1, pp. 613–630. DOI: [10.1002/2017jc013534](https://doi.org/10.1002/2017jc013534).
- Arndt, J. E., H. W. Schenke, M. Jakobsson, F. O. Nitsche, G. Buys, B. Goleby, M. Rebesco, F. Bohoyo, J. Hong, J. Black, R. Greku, G. Udintsev, F. Barrios, W. Reynoso-Peralta, M. Taisei, and R. Wigley (2013). “The International Bathymetric Chart of the Southern Ocean (IBCSO) Version 1.0-A new bathymetric compilation covering circum-Antarctic waters”. In: *Geophysical Research Letters* 40.12, pp. 3111–3117. DOI: [10.1002/grl.50413](https://doi.org/10.1002/grl.50413).
- Assmann, K. M., E. Darelius, A. K. Wåhlin, T. W. Kim, and S. H. Lee (2019). “Warm Circumpolar Deep Water at the Western Getz Ice Shelf Front, Antarctica”. In: *Geophysical Research Letters* 46.2, pp. 870–878. DOI: [10.1029/2018gl1081354](https://doi.org/10.1029/2018gl1081354).
- Assmann, K. M., H. H. Hellmer, and S. S. Jacobs (2005). “Amundsen Sea ice production and transport”. In: *Journal of Geophysical Research* 110. DOI: [10.1029/2004jc002797](https://doi.org/10.1029/2004jc002797).
- Assmann, K. M., A. Jenkins, D. R. Shoosmith, D. P. Walker, S. S. Jacobs, and K. W. Nicholls (2013). “Variability of Circumpolar Deep Water transport onto the Amundsen Sea continental shelf through a shelf break trough”. In: *Journal of Geophysical Research: Oceans* 118, 6603–6620. DOI: [doi: 10.1002/2013JC008871](https://doi.org/10.1002/2013JC008871).
- Auger, M., R. Morrow, E. Kestenare, J.-B. Sallée, and R. Cowley (2021). “Southern Ocean in-situ temperature trends over 25 years emerge from interannual variability”. In: *Nature Communications* 12.1. DOI: [10.1038/s41467-020-20781-1](https://doi.org/10.1038/s41467-020-20781-1).
- Auger, M., P. Prandi, and J.-B. Sallée (2022). “Southern ocean sea level anomaly in the sea ice-covered sector from multimission satellite observations”. In: *Scientific Data* 9.1. DOI: [10.1038/s41597-022-01166-z](https://doi.org/10.1038/s41597-022-01166-z).

- Azaneu, M., K. J. Heywood, B. Y. Queste, and A. F. Thompson (2017). “Variability of the Antarctic Slope Current System in the Northwestern Weddell Sea”. In: *Journal of Physical Oceanography* 47.12, pp. 2977–2997. DOI: [10.1175/jpo-d-17-0030.1](https://doi.org/10.1175/jpo-d-17-0030.1).
- Baines, P. G. and S. Condie (1998). “Observations and modelling of Antarctic downslope flows: A review”. In: *Antarctic Research Series* 75, pp. 29–49.
- Billany, W., S. Swart, J. Hermes, and C. J. C. Reason (2010). “Variability of the Southern Ocean fronts at the Greenwich Meridian”. In: *Journal of Marine Systems* 82.4, pp. 304–310. DOI: [10.1016/j.jmarsys.2010.06.005](https://doi.org/10.1016/j.jmarsys.2010.06.005).
- Bower, A. S., H. T. Rossby, and J. L. Lillibridge (1985). “The Gulf Stream - Barrier or Blender?” In: *Journal of Physical Oceanography* 15.1, pp. 24–32. DOI: [10.1175/1520-0485\(1985\)015<0024:tgsob>2.0.co;2](https://doi.org/10.1175/1520-0485(1985)015<0024:tgsob>2.0.co;2).
- Carter, L., I. N. McCave, and M. J. M. Williams (2008). “Chapter 4 Circulation and Water Masses of the Southern Ocean: A Review”. In: pp. 85–114. DOI: [10.1016/S1571-9197\(08\)00004-9](https://doi.org/10.1016/S1571-9197(08)00004-9).
- Chapman, C. and J.-B. Sallée (2017). “Isopycnal Mixing Suppression by the Antarctic Circumpolar Current and the Southern Ocean Meridional Overturning Circulation”. In: *Journal of Physical Oceanography* 47.8, pp. 2023–2045. DOI: [10.1175/jpo-d-16-0263.1](https://doi.org/10.1175/jpo-d-16-0263.1).
- Chapman, C. C., M.-A. Lea, A. Meyer, J.-B. Sallée, and M. Hindell (2020). “Defining Southern Ocean fronts and their influence on biological and physical processes in a changing climate”. In: *Nature Climate Change* 10.3, pp. 209–219. DOI: [10.1038/s41558-020-0705-4](https://doi.org/10.1038/s41558-020-0705-4).
- Chavanne, C. P., K. J. Heywood, K. W. Nicholls, and I. Fer (2010). “Observations of the Antarctic Slope Undercurrent in the southeastern Weddell Sea”. In: *Geophysical Research Letters* 37, p. 5. DOI: [doi:10.1029/2010GL043603](https://doi.org/10.1029/2010GL043603).
- Chidichimo, M., K. A. Donohue, D. R. Watts, and K. L. Tracey (2014). “Baroclinic Transport Time Series of the Antarctic Circumpolar Current Measured in Drake Passage”. In: *Journal of Physical Oceanography* 44.7, pp. 1829–1853. DOI: [10.1175/jpo-d-13-071.1](https://doi.org/10.1175/jpo-d-13-071.1).
- Church, J. A., P. U. Clark, A. Cazenave, J. M. Gregory, S. Jevrejeva, A. Levermann, M. A. Merrifield, G. A. Milne, R. S. Nerem, P. D. Nunn, A. J. Payne, W. T. Pfeffer, D. Stammer, and A. S. Unnikrishnan (2013). “Sea Level Change”. In: *Contribution of Working Group I to the Fifth Assessment Report of the Intergovernmental Panel on Climate Change*. Ed. by T. F. Stocker, D. Qin, G.-K. Plattner, M. Tignor, S. K. Allen, J. Boschung, A. Nauels, Y. Xia, V. Bex, and P. M. Midgley, pp. 1137–1216. DOI: [10.1017/cbo9781107415324.026](https://doi.org/10.1017/cbo9781107415324.026).

-
- Cook, A. J., P. R. Holland, M. P. Meredith, T. Murray, A. Luckman, and D. G. Vaughan (2016). “Ocean forcing of glacier retreat in the western Antarctic Peninsula”. In: *Science* 353.6296, pp. 283–286. DOI: [10.1126/science.aae0017](https://doi.org/10.1126/science.aae0017).
- Cook, A. J. and D. G. Vaughan (2010). “Overview of areal changes of the ice shelves on the Antarctic Peninsula over the past 50 years”. In: *The Cryosphere* 4, pp. 77–98. DOI: [10.5194/tc-4-77-2010](https://doi.org/10.5194/tc-4-77-2010).
- Couto, N., D. G. Martinson, J. Kohut, and O. Schofield (2017). “Distribution of Upper Circumpolar Deep Water on the warming continental shelf of the West Antarctic Peninsula”. In: *Journal of Geophysical Research: Oceans* 122.7, pp. 5306–5315. DOI: [10.1002/2017jc012840](https://doi.org/10.1002/2017jc012840).
- Dai, A., T. Qian, K. E. Trenberth, and J. D. Milliman (2009). “Changes in Continental Freshwater Discharge from 1948 to 2004”. In: *Journal of Climate* 22.10, pp. 2773–2792. DOI: [10.1175/2008jcli2592.1](https://doi.org/10.1175/2008jcli2592.1).
- Dangendorf, S., C. Hay, F. M. Calafat, M. Marcos, C. G. Piecuch, K. Berk, and J. Jensen (2019). “Persistent acceleration in global sea-level rise since the 1960s”. In: *Nature Climate Change* 9.9, pp. 705–710. DOI: [10.1038/s41558-019-0531-8](https://doi.org/10.1038/s41558-019-0531-8).
- Dinniman, M. S. and J. M. Klinck (2004). “A model study of circulation and cross-shelf exchange on the west Antarctic Peninsula continental shelf”. In: *Deep Sea Research Part II: Topical Studies in Oceanography* 51.17-19, pp. 2003–2022. DOI: [10.1016/j.dsr2.2004.07.030](https://doi.org/10.1016/j.dsr2.2004.07.030).
- Dinniman, M. S., J. M. Klinck, and E. E. Hoffmann (2012). “Sensitivity of Circumpolar Deep Water Transport and Ice Shelf Basal Melt along the West Antarctic Peninsula to Changes in the Winds”. In: *Journal of Climate* 25, 4799–4816. DOI: [10.1175/JCLI-D-11-00307.1](https://doi.org/10.1175/JCLI-D-11-00307.1).
- Dotto, T. S., A. C. N. Garabato, S. Bacon, P. R. Holland, S. Kimura, Y. L. Firing, M. Tsamados, A. K. Wåhlin, and A. Jenkins (2019). “Wind-Driven Processes Controlling Oceanic Heat Delivery to the Amundsen Sea, Antarctica”. In: *Journal of Physical Oceanography* 49.11, pp. 2829–2849. DOI: [10.1175/jpo-d-19-0064.1](https://doi.org/10.1175/jpo-d-19-0064.1).
- Dotto, T. S., A. C. Naveira Garabato, A. K. Wåhlin, S. Bacon, P. R. Holland, S. Kimura, M. Tsamados, L. Herraiz-Borreguero, O. Kalén, and A. Jenkins (2020). “Control of the Oceanic Heat Content of the Getz-Dotson Trough, Antarctica, by the Amundsen Sea Low”. In: *Journal of Geophysical Research: Oceans* 125.8. DOI: [10.1029/2020jc016113](https://doi.org/10.1029/2020jc016113).
- Drévuillon, M., C. Regnier, J. M. Lellouche, G. Garric, C. Bricaud, and O. Hernandez (2021). “Quality Information Document for Global Ocean Reanalysis

- Products GLOBAL_REANALYSIS_PHY_001_030". In: *CMEMS-GLO-QUID-001-030*, pp. 1–52.
- Dutrieux, P., J. De Rydt, A. Jenkins, P. R. Holland, H. K. Ha, S. H. Lee, E. J. Steig, Q. Ding, E. P. Abrahamsen, and M. Schröder (2014). “Strong Sensitivity of Pine Island Ice-Shelf Melting to Climatic Variability”. In: *Science* 343, pp. 174–178. DOI: [10.1126/science.1244341](https://doi.org/10.1126/science.1244341).
- Fernandez, E. and J. M. Lellouche (2021). “Product User Manual for Global Ocean Reanalysis Products GLOBAL_REANALYSIS_PHY_001_030”. In: *CMEMS-GLO-QUID-001-030*, pp. 1–21.
- Ferrari, R. and M. Nikurashin (2010). “Suppression of Eddy Diffusivity across Jets in the Southern Ocean”. In: *Journal of Physical Oceanography* 40.7, pp. 1501–1519. DOI: [10.1175/2010jpo4278.1](https://doi.org/10.1175/2010jpo4278.1).
- Flexas, M. M., A. F. Thompson, M. P. Schodlok, H. Zhang, and K. Speer (2022). “Antarctic Peninsula warming triggers enhanced basal melt rates throughout West Antarctica”. In: *Science Advances* 8.32. DOI: [10.1126/sciadv.abj9134](https://doi.org/10.1126/sciadv.abj9134).
- Frederikse, T., F. Landerer, L. Caron, S. Adhikari, D. Parkes, V. W. Humphrey, S. Dangendorf, P. Hogarth, L. Zanna, L. Cheng, and Y.-H. Wu (2020). “The causes of sea-level rise since 1900”. In: *Nature* 584.7821, pp. 393–397. DOI: [10.1038/s41586-020-2591-3](https://doi.org/10.1038/s41586-020-2591-3).
- Fretwell, P. et al. (2013). “Bedmap2: improved ice bed, surface and thickness datasets for Antarctica”. In: *The Cryosphere* 7.1, pp. 375–393. DOI: [10.5194/tc-7-375-2013](https://doi.org/10.5194/tc-7-375-2013).
- Gille, S. T. (2002). “Warming of the Southern Ocean Since the 1950s”. In: *Science* 295, pp. 1275–1277. DOI: [10.1126/science.1065863](https://doi.org/10.1126/science.1065863).
- (2008). “Decadal-Scale Temperature Trends in the Southern Hemisphere Ocean”. In: *Journal of Climate* 21.18, pp. 4749–4765. DOI: [10.1175/2008jcli2131.1](https://doi.org/10.1175/2008jcli2131.1).
- (2014). “Meridional displacement of the Antarctic Circumpolar Current”. In: *Philosophical Transactions of the Royal Society A* 372.20130273, pp. 1–12. DOI: [10.1098/rsta.2013.0273](https://doi.org/10.1098/rsta.2013.0273).
- Gille, S. T., D. C. McKee, and D. G. Martinson (2016). “Temporal Changes in the Antarctic Circumpolar Current: Implications for the Antarctic Continental Shelves”. In: *The Oceanography Society* 29.4, pp. 95–106. DOI: [10.2307/24862285](https://doi.org/10.2307/24862285).
- Graham, J. A., M. S. Dinniman, and J. M. Klinck (2016). “Impact of model resolution for on-shelf heat transport along the West Antarctic Peninsula”.

-
- In: *Journal of Geophysical Research: Oceans* 121.10, pp. 7880–7897. DOI: [10.1002/2016jc011875](https://doi.org/10.1002/2016jc011875).
- Graham, R. M., A. M. de Boer, K. J. Heywood, M. R. Chapman, and D. P. Stevens (2012). “Southern Ocean fronts: Controlled by wind or topography?” In: *Journal of Geophysical Research: Oceans* 117.C8, n/a–n/a. DOI: [10.1029/2012jc007887](https://doi.org/10.1029/2012jc007887).
- Griesel, A., S. T. Gille, J. Sprintall, J. L. McClean, J. H. LaCasce, and M. E. Maltrud (2010). “Isopycnal diffusivities in the Antarctic Circumpolar Current inferred from Lagrangian floats in an eddying model”. In: *Journal of Geophysical Research* 115.C6. DOI: [10.1029/2009jc005821](https://doi.org/10.1029/2009jc005821).
- Haine, T. W. N. and J. Marshall (1998). “Gravitational, Symmetric, and Baroclinic Instability of the Ocean Mixed Layer”. In: *Journal of Physical Oceanography* 28.4, pp. 634–658. DOI: [10.1175/1520-0485\(1998\)028<0634:gsabio>2.0.co;2](https://doi.org/10.1175/1520-0485(1998)028<0634:gsabio>2.0.co;2).
- Hay, C. C., E. Morrow, R. E. Kopp, and J. X. Mitrovica (2017). “Erratum: Probabilistic reanalysis of twentieth-century sea-level rise”. In: *Nature* 552.7684, pp. 278–278. DOI: [10.1038/nature24466](https://doi.org/10.1038/nature24466).
- Hazel, J. E. and A. L. Stewart (2019). “Are the Near-Antarctic Easterly Winds Weakening in Response to Enhancement of the Southern Annular Mode?” In: *Journal of Climate* 32.6, pp. 1895–1918. DOI: [10.1175/jcli-d-18-0402.1](https://doi.org/10.1175/jcli-d-18-0402.1).
- Hersbach, H., B. Bell, P. Berrisford, G. Horányi, J. Muñoz Sabater, J. Nicolas, C. Peubey, R. Radu, I. Rozum, D. Schepers, A. Simmons, C. Soci, D. Dee, and J.-N. Thépaut (2019). “ERA5 monthly averaged data on single levels from 1979 to present”. In: *Copernicus Climate Change Journal*. DOI: [10.24381/CDS.F17050D7](https://doi.org/10.24381/CDS.F17050D7).
- Heywood, K. J., A. C. Naveira-Garabato, D. P. Stevens, and R. D. Muench (2004). “On the fate of the Antarctic Slope Front and the origin of the Weddell Front”. In: *Journal of Geophysical Research* 109.C6. DOI: [10.1029/2003JC002053](https://doi.org/10.1029/2003JC002053).
- Hofmann, E. E. (1985). “The large-scale horizontal structure of the Antarctic Circumpolar Current from FGGE drifters”. In: *Journal of Geophysical Research* 90.C4, p. 7087. DOI: [10.1029/jc090ic04p07087](https://doi.org/10.1029/jc090ic04p07087).
- Hogg, A. E., A. Shepherd, S. L. Cornford, K. H. Briggs, N. Gourmelen, J. A. Graham, I. Joughin, J. Mouginot, T. Nagler, A. J. Payne, E. Rignot, and J. Wuite (2017). “Increased ice flow in Western Palmer Land linked to ocean melting”. In: *Geophysical Research Letters* 44.9, pp. 4159–4167. DOI: [10.1002/2016gl072110](https://doi.org/10.1002/2016gl072110).

- Hogg, A. McC., M. P. Meredith, D. P. Chambers, E. P. Abrahamson, C. W. Hughes, and A. K. Morrison (2015). “Recent trends in the Southern Ocean eddy field”. In: *Journal of Geophysical Research: Oceans* 120.1, pp. 257–267. DOI: [10.1002/2014jc010470](https://doi.org/10.1002/2014jc010470).
- Holland, P. R., T. J. Bracegirdle, P. Dutrieux, A. Jenkins, and E. J. Steig (2019). “West Antarctic ice loss influenced by internal climate variability and anthropogenic forcing”. In: *Nature Geoscience* 12.9, pp. 718–724. DOI: [10.1038/s41561-019-0420-9](https://doi.org/10.1038/s41561-019-0420-9).
- Holland, P. R., A. Jenkins, and D. M. Holland (2010). “Ice and ocean processes in the Bellingshausen Sea, Antarctica”. In: *Journal of Geophysical Research* 115, p. 16. DOI: [10.1029/2008JC005219](https://doi.org/10.1029/2008JC005219).
- Hosking, J. S., A. Orr, T. J. Bracegirdle, and J. Turner (2016). “Future circulation changes off West Antarctica: Sensitivity of the Amundsen Sea Low to projected anthropogenic forcing”. In: *Geophysical Research Letters* 43, pp. 367–376. DOI: [10.1002/2015GL067143](https://doi.org/10.1002/2015GL067143).
- Hosking, J. S., Andrew Orr, Gareth J. Marshall, John Turner, and Tony Phillips (2013). “The Influence of the Amundsen–Bellingshausen Seas Low on the Climate of West Antarctica and Its Representation in Coupled Climate Model Simulations”. In: *Journal of Climate* 26, 6633–6648. DOI: [10.1175/JCLI-D-12-00813.1](https://doi.org/10.1175/JCLI-D-12-00813.1).
- Hughes, C. W. and E. R. Ash (2001). “Eddy forcing of the mean flow in the Southern Ocean”. In: *Journal of Geophysical Research: Oceans* 106.C2, pp. 2713–2722. DOI: [10.1029/2000jc900332](https://doi.org/10.1029/2000jc900332).
- IOC, SCOR, and IAPSO (2010). “The international thermodynamic equation of seawater – 2010: Calculation and use of thermodynamic properties.” In: *Intergovernmental Oceanographic Commission, Manuals and Guides No. 56, UNESCO (English)*, pp. 1–196. URL: <https://www.teos-10.org/>.
- Jacobs, S. S. (1991). “On the nature and significance of the Antarctic and Slope Front”. In: *Marine Chemistry* 35, pp. 9–24. DOI: [10.1016/S0304-4203\(09\)90005-6](https://doi.org/10.1016/S0304-4203(09)90005-6).
- Jacobs, S. S., A. Jenkins, C. F. Giulivi, and P. Dutrieux (2011). “Stronger ocean circulation and increased melting under Pine Island Glacier ice shelf”. In: *Nature Geoscience* 4.8, pp. 519–523. DOI: [10.1038/ngeo1188](https://doi.org/10.1038/ngeo1188).
- Jacobs, S. S., A. Jenkins, H. Hellmer, C. Giulivi, F. Nitsche, B. Huber, and R. Gurrero (2012). “The Amundsen Sea and the Antarctic Ice Sheet”. In: *Oceanography* 23, pp. 154–163. DOI: [10.5670/oceanog.2012.90](https://doi.org/10.5670/oceanog.2012.90).
- Jenkins, A., P. Dutrieux, S. S. Jacobs, S. D. McPhail, J. R. Perrett, A. T. Webb, and D. White (2010). “Observations beneath Pine Island Glacier in

- West Antarctica and implications for its retreat”. In: *Nature Geoscience* 3.7, pp. 468–472. DOI: [10.1038/ngeo890](https://doi.org/10.1038/ngeo890).
- Jenkins, A. and S. S. Jacobs (2008). “Circulation and melting beneath George VI Ice Shelf, Antarctica”. In: *Journal of Geophysical Research* 113. DOI: [10.1029/2007JC004449](https://doi.org/10.1029/2007JC004449).
- Jenkins, A., D. Shoosmith, P. Dutrieux, S. S. Jacobs, T. W. Kim, S. H. Lee, H. K. Ha, and S. Stammerjohn (2018). “West Antarctic Ice Sheet retreat in the Amundsen Sea driven by decadal oceanic variability”. In: *Nature Geoscience* 11.10, pp. 733–738. DOI: [10.1038/s41561-018-0207-4](https://doi.org/10.1038/s41561-018-0207-4).
- Joughin, I., S. Tulaczyk, R. Bindschadler, and S. F. Price (2002). “Changes in west Antarctic ice stream velocities: Observation and analysis”. In: *Journal of Geophysical Research: Solid Earth* 107.B11. DOI: [10.1029/2001jb001029](https://doi.org/10.1029/2001jb001029).
- Khazendar, A., M. P. Schodlok, I. Fenty, S. R. M. Ligtenberg, E. Rignot, and M. R. van den Broeke (2013). “Observed thinning of Totten Glacier is linked to coastal polynya variability”. In: *Nature Communications* 4.1. DOI: [10.1038/ncomms3857](https://doi.org/10.1038/ncomms3857).
- Kim, T.-W., H. K. Ha, A. K. Wählin, S. H. Lee, C. S. Kim, J. H. Lee, and Y. K. Cho (2017). “Is Ekman pumping responsible for the seasonal variation of warm circumpolar deep water in the Amundsen Sea?” In: *Continental Shelf Research* 132, pp. 38–48. DOI: [10.1016/j.csr.2016.09.005](https://doi.org/10.1016/j.csr.2016.09.005).
- Kim, T.-W., H. W. Yang, P. Dutrieux, A. K. Wählin, A. Jenkins, Y. G. Kim, H. K. Ha, C.-S. Kim, K.-H. Cho, T. Park, J. Park, S. H. Lee, and Y.-K. Cho (2021). “Interannual Variation of Modified Circumpolar Deep Water in the Dotson-Getz Trough, West Antarctica”. In: *Journal of Geophysical Research: Oceans* 126.12, pp. 1–25. DOI: [10.1029/2021jc017491](https://doi.org/10.1029/2021jc017491).
- Kim, Y. S. and A. H. Orsi (2014). “On the Variability of Antarctic Circumpolar Current Fronts Inferred from 1992-2011 Altimetry*”. In: *Journal of Physical Oceanography* 44.12, pp. 3054–3071. DOI: [10.1175/jpo-d-13-0217.1](https://doi.org/10.1175/jpo-d-13-0217.1).
- Kimura, S., A. Jenkins, H. Regan, P. R. Holland, K. M. Assmann, D. B. Whitt, M. Van Wessem, W. J. van de Berg, C. H. Reijmer, and P. Dutrieux (2017). “Oceanographic Controls on the Variability of Ice-Shelf Basal Melting and Circulation of Glacial Meltwater in the Amundsen Sea Embayment, Antarctica”. In: *Journal of Geophysical Research: Oceans* 122.12, pp. 10131–10155. DOI: [10.1002/2017jc012926](https://doi.org/10.1002/2017jc012926).

- Klinck, J. M., E. E. Hofmanna, R. C. Beardsley, B. Salihoglua, and S. Howard (2004). “Water-mass properties and circulation on the west Antarctic Peninsula Continental Shelf in Austral Fall and Winter 2001”. In: *Deep Sea Research Part II: Topical Studies in Oceanography* 51, pp. 1925–1946. DOI: [10.1016/j.dsr2.2004.08.001](https://doi.org/10.1016/j.dsr2.2004.08.001).
- Koenig, Z., C. Provost, R. Ferrari, N. Sennéchaël, and M.-H. Rio (2014). “Volume transport of the Antarctic Circumpolar Current: Production and validation of a 20 year long time series obtained from in situ and satellite observations”. In: *Journal of Geophysical Research: Oceans* 119.8, pp. 5407–5433. DOI: [10.1002/2014jc009966](https://doi.org/10.1002/2014jc009966).
- Konrad, H., A. Shepherd, L. Gilbert, A. E. Hogg, M. McMillan, A. Muir, and T. Slater (2018). “Net retreat of Antarctic glacier grounding lines”. In: *Nature Geoscience* 11.4, pp. 258–262. DOI: [10.1038/s41561-018-0082-z](https://doi.org/10.1038/s41561-018-0082-z).
- Martinson, D. G. and D. C. McKee (2012). “Transport of warm Upper Circumpolar Deep Water onto the western Antarctic Peninsula continental shelf”. In: *Ocean Science* 8.4, pp. 433–442. DOI: [10.5194/os-8-433-2012](https://doi.org/10.5194/os-8-433-2012).
- Martinson, D. G., S. E. Stammerjohn, R. A. Iannuzzi, R. C. Smith, and M. Vernet (2008). “Western Antarctic Peninsula physical oceanography and spatio-temporal variability”. In: *Deep-Sea Research II* 55, pp. 1964–1987. DOI: [10.1016/j.dsr2.2008.04.038](https://doi.org/10.1016/j.dsr2.2008.04.038).
- Meredith, M. P. and A. M. Hogg (2006). “Circumpolar response of Southern Ocean eddy activity to a change in the Southern Annular Mode”. In: *Geophysical Research Letters* 33.16. DOI: [10.1029/2006g1026499](https://doi.org/10.1029/2006g1026499).
- Morrison, A. K., T. L. Frölicher, and J. L. Sarmiento (2015). “Upwelling in the southern ocean”. In: *Physics Today* 68.1, p. 27.
- Nakayama, Y., D. Menemenlis, M. Schodlok, and E. Rignot (2017). “Amundsen and Bellingshausen Seas simulation with optimized ocean, sea ice, and thermodynamic ice shelf model parameters”. In: *Journal of Geophysical Research: Oceans* 122.8, pp. 6180–6195. DOI: [10.1002/2016jc012538](https://doi.org/10.1002/2016jc012538).
- Nakayama, Y., D. Menemenlis, H. Zhang, M. Schodlok, and E. Rignot (2018). “Origin of Circumpolar Deep Water intruding onto the Amundsen and Bellingshausen Sea continental shelves”. In: *Nature Communications* 9.1. DOI: [10.1038/s41467-018-05813-1](https://doi.org/10.1038/s41467-018-05813-1).
- Narayanan, A., S. T. Gille, M. R. Mazloff, and K. Murali (2019). “Water Mass Characteristics of the Antarctic Margins and the Production and Seasonality of Dense Shelf Water”. In: *Journal of Geophysical Research: Oceans* 124.12, pp. 9277–9294. DOI: [10.1029/2018jc014907](https://doi.org/10.1029/2018jc014907).

-
- Naveira-Garabato, A. C., R. Ferrari, and K. L. Polzin (2011). “Eddy stirring in the Southern Ocean”. In: *Journal of Geophysical Research* 116.C9. DOI: [10.1029/2010jc006818](https://doi.org/10.1029/2010jc006818).
- Oppenheimer, M., B. C. Glavovic, J. Hinkel, R. van de Wal, A. K. Magnan, A. Abd-Elgawad, R. Cai, M. Cifuentes-Jara, R. M. DeConto, T. Ghosh, J. Hay, F. Isla, B. Marzeion, B. Meyssignac, and Z. Sebesvari (2019). “Sea Level Rise and Implications for Low-Lying Islands, Coasts and Communities”. In: ed. by H.-O. Pörtner, D. C. Roberts, V. Masson-Delmotte, P. Zhai, M. Tignor, E. Poloczanska, K. Mintenbeck, A. Alegría, M. Nicola, A. Okem, J. Petzold, B. Rama, and N. M. Weyer, pp. 321–446. DOI: [10.1017/9781009157964.006](https://doi.org/10.1017/9781009157964.006).
- Orsi, A. H., T. Whitworth, and W. D. Nowlin (1995). “On the meridional extent and fronts of the Antarctic Circumpolar Current”. In: *Deep Sea Research Part I: Oceanographic Research Papers* 42, pp. 641–673. DOI: [10.1016/0967-0637\(95\)00021-W](https://doi.org/10.1016/0967-0637(95)00021-W).
- Paolo, F. S., H. A. Fricker, and L. Padman (2015). “Volume loss from Antarctic ice shelves is accelerating”. In: *Science* 348, pp. 327–331. DOI: [10.1126/science.aaa0940](https://doi.org/10.1126/science.aaa0940).
- Parkinson, C. L. and D. J. Cavalieri (2012). “Antarctic sea ice variability and trends, 1979–2010”. In: *The Cryosphere* 6.4, pp. 871–880. DOI: [10.5194/tc-6-871-2012](https://doi.org/10.5194/tc-6-871-2012).
- Patara, L., C. W. Böning, and A. Biastoch (2016). “Variability and trends in Southern Ocean eddy activity in 1/12° ocean model simulations”. In: *Geophysical Research Letters* 43.9, pp. 4517–4523. DOI: [10.1002/2016gl069026](https://doi.org/10.1002/2016gl069026).
- Peterson, R. G. and W. B. White (1998). “Slow oceanic teleconnections linking the Antarctic Circumpolar Wave with the tropical El Niño–Southern Oscillation”. In: *Journal of Geophysical Research: Oceans* 103.C11, pp. 24573–24583. DOI: [10.1029/98jc01947](https://doi.org/10.1029/98jc01947).
- Pritchard, H. D., S. R. M. Ligtenberg, H. A. Fricker, D. G. Vaughan, M. R. van den Broeke, and L. Padman (2012). “Antarctic ice-sheet loss driven by basal melting of ice shelves”. In: *Nature* 484.7395, pp. 502–505. DOI: [10.1038/nature10968](https://doi.org/10.1038/nature10968).
- Pujol, M.-I. (2022). “PRODUCT USER MANUAL. For Sea Level Altimeter Products.” In: *CMEMS-SL-PUM-008-032-062*, pp. 1–42.
- Rignot, E., G. Casassa, P. Gogineni, W. Krabill, A. Rivera, and R. Thomas (2004). “Accelerated ice discharge from the Antarctic Peninsula following the collapse of Larsen B ice shelf”. In: *Geophysical Research Letters* 31.18. DOI: [10.1029/2004gl020697](https://doi.org/10.1029/2004gl020697).

- Rignot, E., J. Mouginot, M. Morlighem, H. Seroussi, and B. Scheuchl (2014). “Widespread, rapid grounding line retreat of Pine Island, Thwaites, Smith, and Kohler glaciers, West Antarctica, from 1992 to 2011”. In: *Geophysical Research Letters* 41.10, pp. 3502–3509. DOI: [10.1002/2014gl060140](https://doi.org/10.1002/2014gl060140).
- Rignot, E., J. Mouginot, B. Scheuchl, M. van den Broeke, M. J. van Wessem, and M. Morlighem (2019). “Four decades of Antarctic Ice Sheet mass balance from 1979–2017”. In: *PNAS* 116, pp. 1095–1103. DOI: [10.1073/pnas.1812883116](https://doi.org/10.1073/pnas.1812883116).
- Rintoul, S. R., C. W. Hughes, and D. Olbers (2001). “Chapter 4.6 The Antarctic Circumpolar Current System”. In: *International Geophysics* 77, pp. 271–302. DOI: [10.1016/S0074-6142\(01\)80124-8](https://doi.org/10.1016/S0074-6142(01)80124-8).
- Roach, Christopher J. and Kevin Speer (2019). “Exchange of Water Between the Ross Gyre and ACC Assessed by Lagrangian Particle Tracking”. In: *Journal of Geophysical Research: Oceans* 124.7, pp. 4631–4643. DOI: [10.1029/2018jc014845](https://doi.org/10.1029/2018jc014845).
- Ruan, X., K. G. Speer, A. F. Thompson, L. M. Schulze-Chretien, and D. R. Shoosmith (2021). “Ice-Shelf Meltwater Overturning in the Bellingshausen Sea”. In: *Journal of Geophysical Research: Oceans* 126.5. DOI: [10.1029/2020jc016957](https://doi.org/10.1029/2020jc016957).
- Scambos, T. A., J. A. Bohlander, C. A. Shuman, and P. Skvarca (2004). “Glacier acceleration and thinning after ice shelf collapse in the Larsen B embayment, Antarctica”. In: *Geophysical Research Letters* 31.18. DOI: [10.1029/2004g1020670](https://doi.org/10.1029/2004g1020670).
- Schaffer, J., R. Timmermann, J. E. Arndt, S. S. Kristensen, C. Mayer, M. Morlighem, and D. Steinhage (2016). “A global, high-resolution data set of ice sheet topography, cavity geometry, and ocean bathymetry”. In: *Earth System Science Data* 8, pp. 543–557. DOI: [10.5194/essd-8-543-2016](https://doi.org/10.5194/essd-8-543-2016).
- Schaffer, J., R. Timmermann, J. E. Arndt, S. H. R. Rosier, P. G. D. Anker, S. L. Callard, P. E. D. Davis, B. Dorschel, H. Grob, T. Hattermann, C. M. Hofstede, T. Kanzow, M. Kappelsberger, J. M. Lloyd, C. Ó Cofaigh, and D. H. Roberts (2019). *An update to Greenland and Antarctic ice sheet topography, cavity geometry, and global bathymetry (RTopo-2.0.4)*. data set. Supplement to: Schaffer, Janin; Kanzow, Torsten; von Appen, Wilken-Jon; von Albedyll, Luisa; Arndt, Jan Erik; Roberts, David H (2020): Bathymetry constrains ocean heat supply to Greenland's largest glacier tongue. *Nature Geoscience*, 13(3), 227–231, <https://doi.org/10.1038/s41561-019-0529-x>. DOI: [10.1594/PANGAEA.905295](https://doi.org/10.1594/PANGAEA.905295). URL: <https://doi.org/10.1594/PANGAEA.905295>.

-
- Schmidtko, S., K. J. Heywood, A. F. Thompson, and S. Aoki (2014). “Multi-decadal warming of Antarctic waters”. In: *Science* 346, pp. 1227–1231. DOI: [10.1126/science.1256117](https://doi.org/10.1126/science.1256117).
- Schubert, R., A. F. Thompson, K. Speer, L. Schulze-Chretien, and Y. Bebieva (2021). “The Antarctic Coastal Current in the Bellingshausen Sea”. In: *The Cryosphere* 15.9, pp. 4179–4199. DOI: [10.5194/tc-15-4179-2021](https://doi.org/10.5194/tc-15-4179-2021).
- Schulze-Chretien, L. M., A. F. Thompson, M. M. Flexas, K. Speer, N. Swaim, R. Oelerich, X. Ruan, R. Schubert, and C. LoBuglio (2021). “The Shelf Circulation of the Bellingshausen Sea”. In: *Journal of Geophysical Research: Oceans* 126.5. DOI: [10.1029/2020jc016871](https://doi.org/10.1029/2020jc016871).
- Shao, A. E., S. T. Gille, S. Mecking, and L. Thompson (2015). “Properties of the Subantarctic Front and Polar Front from the skewness of sea level anomaly”. In: *Journal of Geophysical Research: Oceans* 120.7, pp. 5179–5193. DOI: [10.1002/2015jc010723](https://doi.org/10.1002/2015jc010723).
- Shepherd, A., H. A. Fricker, and S. L. Farrell (2018). “Trends and connections across the Antarctic cryosphere”. In: *Nature* 558.7709, pp. 223–232. DOI: [10.1038/s41586-018-0171-6](https://doi.org/10.1038/s41586-018-0171-6).
- Shepherd, A., D. Wingham, D. Wallis, K. Giles, S. Laxon, and A. V. Sundal (2012a). “Correction to “Recent loss of floating ice and the consequent sea level contribution””. In: *Geophysical Research Letters* 39.17. DOI: [10.1029/2012g1053573](https://doi.org/10.1029/2012g1053573).
- Shepherd, A., D. J. Wingham, and J. A. D. Mansley (2002). “Inland thinning of the Amundsen Sea sector, West Antarctica”. In: *Geophysical Research Letters* 29.10. DOI: [10.1029/2001g1014183](https://doi.org/10.1029/2001g1014183).
- Shepherd, A. et al. (2012b). “A Reconciled Estimate of Ice-Sheet Mass Balance”. In: *Science* 338.6111, pp. 1183–1189. DOI: [10.1126/science.1228102](https://doi.org/10.1126/science.1228102).
- Shi, J.-R., L. D. Talley, S.-P. Xie, Q. Peng, and W. Liu (2021). “Ocean warming and accelerating Southern Ocean zonal flow”. In: *Nature Climate Change* 11.12, pp. 1090–1097. DOI: [10.1038/s41558-021-01212-5](https://doi.org/10.1038/s41558-021-01212-5).
- Smith, D. A., E. E. Hofmann, J. M. Klinck, and C. M. Lascara (1999). “Hydrography and circulation of the West Antarctic Peninsula Continental Shelf”. In: *Deep Sea Research Part I: Oceanographic Research Papers* 46, pp. 925–949. DOI: [10.1016/S0967-0637\(98\)00103-4](https://doi.org/10.1016/S0967-0637(98)00103-4).
- Sokolov, S. and S. R. Rintoul (2007). “Multiple Jets of the Antarctic Circumpolar Current South of Australia*”. In: *Journal of Physical Oceanography* 37.5, pp. 1394–1412. DOI: [10.1175/jpo3111.1](https://doi.org/10.1175/jpo3111.1).

- Sokolov, S. and S. R. Rintoul (2009a). “Circumpolar structure and distribution of the Antarctic Circumpolar Current fronts: 1. Mean circumpolar paths”. In: *Journal of Geophysical Research: Ocean* 114. DOI: [10.1029/2008JC005108](https://doi.org/10.1029/2008JC005108).
- (2009b). “Circumpolar structure and distribution of the Antarctic Circumpolar Current fronts: 2. Variability and relationship to sea surface height”. In: *Journal of Geophysical Research* 114.C11019, pp. 1–15. DOI: [10.1029/2008JC005248](https://doi.org/10.1029/2008JC005248).
- Speer, K., S. R. Rintoul, and B. Sloyan (2000). “The Diabatic Deacon Cell”. In: *Journal of Physical Oceanography* 30.12, pp. 1312–1322. DOI: [10.1175/1520-0485\(2000\)030<3212:TDDC>2.0.CO;2](https://doi.org/10.1175/1520-0485(2000)030<3212:TDDC>2.0.CO;2).
- St-Laurent, P., J. M. Klinck, and M. S. Dinniman (2015). “Impact of local winter cooling on the melt of Pine Island Glacier, Antarctica”. In: *Journal of Geophysical Research: Oceans* 120.10, pp. 6718–6732. DOI: [10.1002/2015jc010709](https://doi.org/10.1002/2015jc010709).
- Steig, E. J., Q. Ding, D. S. Battisti, and A. Jenkins (2012). “Tropical forcing of Circumpolar Deep Water Inflow and outlet glacier thinning in the Amundsen Sea Embayment, West Antarctica”. In: *Annals of Glaciology* 53.60, pp. 19–28. DOI: [10.3189/2012aog60a110](https://doi.org/10.3189/2012aog60a110).
- Stewart, A. L. (2021). “Warming spins up the Southern Ocean”. In: *Nature Climate Change* 11.12, pp. 1022–1024. DOI: [10.1038/s41558-021-01227-y](https://doi.org/10.1038/s41558-021-01227-y).
- Stukel, M. R., L. I. Aluwihare, K. A. Barbeau, A. M. Chekalyuk, R. Goericke, A. J. Miller, M. D. Ohman, A. Ruacho, H. Song, B. M. Stephens, and M. R. Landry (2017). “Mesoscale ocean fronts enhance carbon export due to gravitational sinking and subduction”. In: *Proceedings of the National Academy of Sciences* 114.6, pp. 1252–1257. DOI: [10.1073/pnas.1609435114](https://doi.org/10.1073/pnas.1609435114). eprint: <https://www.pnas.org/doi/pdf/10.1073/pnas.1609435114>. URL: <https://www.pnas.org/doi/abs/10.1073/pnas.1609435114>.
- Swart, N. C., S. T. Gille, J. C. Fyfe, and N. P. Gillett (2018). “Recent Southern Ocean warming and freshening driven by greenhouse gas emissions and ozone depletion”. In: *Nature Geoscience* 11.11, pp. 836–841. DOI: [10.1038/s41561-018-0226-1](https://doi.org/10.1038/s41561-018-0226-1).
- Talley, L. D., G. L. Pickard, W. J. Emery, and J. H. Smith (2011). *Descriptive Physical Oceanography: an Introduction*. 6th ed. Elsevier Ltd., p. 555.
- Thoma, M., A. Jenkins, D. Holland, and S. Jacobs (2008). “Modelling Circumpolar Deep Water intrusions on the Amundsen Sea continental shelf, Antarctica”. In: *Geophysical Research Letters* 35. DOI: [10.1029/2008GL034939](https://doi.org/10.1029/2008GL034939).

-
- Thompson, A. F. and K. J. Heywood (2008). “Frontal structure and transport in the northwestern Weddell Sea”. In: *Deep Sea Research Part I: Oceanographic Research Papers* 55.10, pp. 1229–1251. DOI: [10.1016/j.dsr.2008.06.001](https://doi.org/10.1016/j.dsr.2008.06.001).
- Thompson, A. F. and J.-B. Sallée (2012). “Jets and Topography: Jet Transitions and the Impact on Transport in the Antarctic Circumpolar Current”. In: *Journal of Physical Oceanography* 42.6, pp. 956–972. DOI: [10.1175/jpo-d-11-0135.1](https://doi.org/10.1175/jpo-d-11-0135.1).
- Thompson, A. F., K. G. Speer, and L. M. Schulze Chretien (2020). “Genesis of the Antarctic Slope Current in West Antarctica”. In: *Geophysical Research Letters* 47.16. DOI: [10.1029/2020gl087802](https://doi.org/10.1029/2020gl087802).
- Thompson, A. F., A. L. Stewart, P. Spence, and K. J. Heywood (2018). “The Antarctic Slope Current in a Changing Climate”. In: *Reviews of Geophysics* 56.4, pp. 741–770. DOI: [10.1029/2018rg000624](https://doi.org/10.1029/2018rg000624).
- Thompson, D. W. J., S. Solomon, P. J. Kushner, M. H. England, K. M. Grise, and D. J. Karoly (2011). “Signatures of the Antarctic ozone hole in Southern Hemisphere surface climate change”. In: *Nature Geoscience* 4.11, pp. 741–749. DOI: [10.1038/ngeo1296](https://doi.org/10.1038/ngeo1296).
- Turner, J., T. Phillips, J. S. Hosking, G. J. Marshall, and A. Orr (2013). “The Amundsen Sea Low”. In: *International Journal of Climatology* 33, pp. 1818–1829. DOI: [10.1002/joc.3558](https://doi.org/10.1002/joc.3558).
- Venables, H. J. and M. P. Meredith (2014). “Feedbacks between ice cover, ocean stratification, and heat content in Ryder Bay, western Antarctic Peninsula”. In: *Journal of Geophysical Research: Oceans* 119.8, pp. 5323–5336. DOI: [10.1002/2013jc009669](https://doi.org/10.1002/2013jc009669).
- Wählin, A. K., O. Kalén, L. Arneborgand, G. Björk, G. K. Carvajal, H. K. Ha, T. W. Kim, S. H. Lee, J. H. Lee, and C. Stranne (2013). “Variability of Warm Deep Water Inflow in a Submarine Trough on the Amundsen Sea Shelf”. In: *Journal of Physical Oceanography* 43, pp. 2054–2070. DOI: [10.1175/JPO-D-12-0157.1](https://doi.org/10.1175/JPO-D-12-0157.1).
- Wählin, A. K., N. Steiger, E. Darelius, K. M. Assmann, M. S. Glessmer, H. K. Ha, L. Herraiz-Borreguero, C. Heuzé, A. Jenkins, T. W. Kim, A. K. Mazur, J. Sommeria, and S. Viboud (2020). “Ice front blocking of ocean heat transport to an Antarctic ice shelf”. In: *Nature* 578.7796, pp. 568–571. DOI: [10.1038/s41586-020-2014-5](https://doi.org/10.1038/s41586-020-2014-5).
- Walker, D. P., A. Jenkins, K. M. Assmann, D. R. Shoosmith, and M. A. Brandon (2013). “Oceanographic observations at the shelf break of the Amundsen Sea, Antarctica”. In: *Journal of Geophysical Research* 118, pp. 2906–2918. DOI: [10.1002/jgrc.20212](https://doi.org/10.1002/jgrc.20212).

- Wang, X., D. Giannakis, and J. Slawinska (2018). “The Antarctic circumpolar wave and its seasonality: Intrinsic travelling modes and El Niño-Southern Oscillation teleconnections”. In: *International Journal of Climatology* 39.2, pp. 1026–1040. DOI: [10.1002/joc.5860](https://doi.org/10.1002/joc.5860).
- Webber, B. G. M., K. J. Heywood, D. P. Stevens, P. Dutrieux, E. P. Abrahamson, A. Jenkins, S. S. Jacobs, H. K. Ha, S. H. Lee, and T. W. Kim (2017). “Mechanisms driving variability in the ocean forcing of Pine Island Glacier”. In: *Nature Communications* 8.1. DOI: [10.1038/ncomms14507](https://doi.org/10.1038/ncomms14507).
- White, W. B. and R. G. Peterson (1996). “An Antarctic circumpolar wave in surface pressure, wind, temperature and sea-ice extent”. In: *Nature* 380.6576, pp. 699–702. DOI: [10.1038/380699a0](https://doi.org/10.1038/380699a0).
- Whitworth, T., A. H. Orsi, S.-J. Kim, W. D. Nowlin, and R. A. Locarnini (1985). “Water Masses and Mixing Near the Antarctic Slope Front”. In: *Ocean, Ice, and Atmosphere: Interactions at the Antarctic Continental Margin*. Ed. by S. S. Jacobs and R. F. Weiss. American Geophysical Union (AGU), pp. 1–27. ISBN: 9781118668238. DOI: [10.1029/AR075p0001](https://doi.org/10.1029/AR075p0001). eprint: <https://agupubs.onlinelibrary.wiley.com/doi/pdf/10.1029/AR075p0001>. URL: <https://agupubs.onlinelibrary.wiley.com/doi/abs/10.1029/AR075p0001>.
- Williams, G. D., L. Herraiz-Borreguero, F. Roquet, T. Tamura, K. I. Ohshima, Y. Fukamachi, A. D. Fraser, L. Gao, H. Chen, C. R. McMahon, R. Harcourt, and M. Hindell (2016). “The suppression of Antarctic bottom water formation by melting ice shelves in Prydz Bay”. In: *Nature Communications* 7.1. DOI: [10.1038/ncomms12577](https://doi.org/10.1038/ncomms12577).
- Williams, R. G., C. Wilson, and C. W. Hughes (2007). “Ocean and Atmosphere Storm Tracks: The Role of Eddy Vorticity Forcing”. In: *Journal of Physical Oceanography* 37.9, pp. 2267–2289. DOI: [10.1175/jpo3120.1](https://doi.org/10.1175/jpo3120.1).
- Wåhlin, A. K., X. Yuan, G. Björk, and C. Nohr (2010). “Inflow of Warm Circumpolar Deep Water in the Central Amundsen Shelf”. In: *Journal of Physical Oceanography* 40, pp. 1427–1434. DOI: [10.1175/2010JP04431.1](https://doi.org/10.1175/2010JP04431.1).
- Yamazaki, K., S. Aoki, K. Katsumata, D. Hirano, and Y. Nakayama (2021). “Multidecadal poleward shift of the southern boundary of the Antarctic Circumpolar Current off East Antarctica”. In: *Science Advances* 7.24. DOI: [10.1126/sciadv.abf8755](https://doi.org/10.1126/sciadv.abf8755).
- Zhang, X., A. F. Thompson, M. M. Flexas, F. Roquet, and H. Bornemann (2016). “Circulation and meltwater distribution in the Bellingshausen Sea: From shelf break to coast”. In: *Geophysical Research Letters* 43.12, pp. 6402–6409. DOI: [10.1002/2016gl1068998](https://doi.org/10.1002/2016gl1068998).